

Automatic Ball Balancing Systems

David John Rodrigues

Department of Engineering Mathematics

University of Bristol



A dissertation submitted to the University of Bristol in
accordance with the requirements of the degree of
Doctor of Philosophy in the Faculty of Engineering.

March 2010

Abstract

This thesis investigates the dynamics of automatic balancers for rotating machinery. The key principle of operation is to deploy a series of balancing masses that are free to rotate at a fixed distance from the shaft. Automatic balancers are ‘passive’ and so the masses are carried to their compensating positions solely through the influence of the rotor vibrations. However, such mechanisms do not work for all rotational speeds and their performance is also heavily dependent on the other characteristics of the rotor set-up. Most of the previous research has focused on simple planar systems in which the imbalance is entirely caused by mass eccentricity. Here we extend the understanding of automatic balancers by considering set-ups in which imbalance also arises due to misalignment of the principal axis of inertia.

In the first part of the thesis an analysis of a two-plane automatic ball balancer (ABB) is presented. This device consists of a pair of circular races that are set perpendicular to the shaft in two distinct planes. Within each race are a series of balancing balls that move to compensate any mass imbalance arising from eccentricity or misalignment. The out-of-plane tilting motions are described in terms of Euler angles and an autonomous system of governing equations is derived through the use of rotating coordinates. The steady states are explicitly determined and numerical continuation techniques are employed in order to map out the stability boundaries of the balanced state in various parameter planes. The results of the stability analysis are supplemented with simulations that demonstrate the coexistence of a stable balanced state with other less desirable dynamics.

The ABB model is extended by including effects such as support anisotropy and rotor acceleration. The symmetry of the imbalance is considered, and techniques from equivariant bifurcation theory are used to derive a necessary condition for the stability of the balanced state. The unfolding of the solution structure is explored and we investigate mechanical set-ups in which either the supports or the ABB device are asymmetric. Here it is shown that, provided the imbalance is small, the balanced state is robust to the considered asymmetries.

Next, we perform an experimental study of a specific ABB system that possesses both cylindrical and conical rigid body modes. In the region of the resonances we find a rich variety of dynamics including the coexistence of steady state operation with destabilised ball whirling motions. Nevertheless, for sufficiently high rotational frequencies the balls consistently find their balance compensating positions and the subsequent reductions in vibration levels are repeatedly observed. These results are compared to simulations generated from the mathematical model and a good qualitative and quantitative agreement is established.

Finally, possible directions for future research are identified, and we also provide design guidelines for the implementation of ABBs in ‘real-world’ machines.

Acknowledgements

First of all I would like to thank my supervisors Prof. Alan Champneys, Prof. Mike Friswell and Dr. Eddie Wilson for their continued support and encouragement. Without their guidance and expertise this Ph.D. would not have been possible.

Thanks also goes to Mike Harrison and all the other balancing specialists at Rolls-Royce who took an interest in my research. Their questions and advice were invaluable in providing me with the necessary ‘real-world’ perspective.

I am also grateful to Dr. Kirk Green for paving the way, Dr. Dave Barton for his programming tips and especially Clive Rendall and Tony Griffith for their help with the experiments.

During my time in Bristol I have made many wonderful friends, thanks to all of you for providing the fun times. In particular, a special mention goes to those in the ‘Red House’ for making my home life so relaxed and enjoyable.

Finally a huge thank you goes to my family, especially to my parents for their unbounded love and support throughout the many years of my education. Long may the learning continue...

“Every journey starts with a single step.”
Aboriginal proverb.

Author's Declaration

I declare that the work in this dissertation was carried out in accordance with the regulations of the University of Bristol. The work is original except where indicated by special reference in the text and no part of the dissertation has been submitted for any other degree.

Any views expressed in the dissertation are those of the author and in no way represent those of the University of Bristol.

The dissertation has not been presented to any other University for examination either in the United Kingdom or overseas.

Signed:

Dated:

Contents

List of Tables	v
List of Figures	ix
List of Symbols	xi
1 Introduction	1
1.1 Balancing	1
1.1.1 Single-plane balancing	1
1.1.2 Two-plane balancing	2
1.1.3 Traditional balancing	3
1.1.4 Automatic balancing	4
1.2 Review of a Jeffcott rotor	5
1.2.1 Derivation of the equations of motion	5
1.2.2 Steady state frequency response	7
1.3 The working principle of the ABB	8
1.4 Review of previous work	9
1.4.1 Contemporary theoretical studies	11
1.4.2 Contemporary experimental investigations	12
1.5 Aims and organisation of the thesis	14
2 Automatic two-plane balancing	17
2.1 Derivation of the equations of motion	17
2.1.1 Mechanical set-up	18
2.1.2 Co-ordinate frames	18
2.1.3 Lagrangian formulation	20
2.1.4 Non-dimensionalisation and the equations of motion	26
2.2 Steady state bifurcation analysis	28
2.2.1 Explicit steady state solutions	28
2.2.2 Static imbalance	31
2.2.3 Couple imbalance	36

2.2.4	General dynamic imbalance	36
2.3	Numerical simulations	38
2.3.1	The effect of varying Ω , ε and m	39
2.3.2	The effect of race damping	41
2.3.3	The effect of varying the initial conditions	44
2.4	Discussion	44
3	Breaking the symmetry	47
3.1	Equations of motion	48
3.1.1	Rotating coordinates	48
3.1.2	Inertial frame and support anisotropy	49
3.1.3	Complex coordinates	50
3.1.4	Rotor acceleration	51
3.2	Asymmetry of the imbalance	52
3.2.1	Symmetry identification	54
3.2.2	Pitchfork bifurcation with \mathcal{D}_4 symmetry	56
3.2.3	Symmetry breaking between the races	63
3.3	Asymmetry of the supports	64
3.3.1	Isotropic supports	66
3.3.2	Anisotropic supports	68
3.4	Asymmetry of the device	71
3.5	The effect of the rotor run-up	74
3.6	Discussion	77
4	Experimental Study	79
4.1	Description of the experimental setup	80
4.2	Estimating the rotor parameters	82
4.3	The plain rotor response and support parameter estimation	85
4.4	The response of the ABB	90
4.4.1	An applied imbalance of 3 washers	90
4.4.2	An applied imbalance of 2 washers	93
4.4.3	Effect of rolling friction	95
4.4.4	Further changes to the applied imbalance	98
4.5	Numerical simulation	100
4.5.1	An applied imbalance of 3 washers	101
4.5.2	An applied imbalance of 2 washers	102
4.6	Discussion	105
5	Conclusion and outlook	107

5.1	Summary	107
5.2	Future research	108
5.3	Recommendations for automatic balancer design	110
A	Physical interpretation of the Hopf bifurcation	113
A.1	Supercritical and subcritical Hopf bifurcations	113
A.2	The effect of the initial conditions	115
B	Measurement of the rotor imbalance	117
B.1	Four-run without phase method	117
B.1.1	An example	117
B.2	The imbalance in $(\varepsilon, \chi, \beta)$ notation	119
C	Measurement of the support parameters	123
C.1	Support stiffness	123
C.2	Support damping	125

List of Tables

4.1	Estimated rotor parameters.	83
4.2	Estimated imbalance parameters.	84
4.3	Estimated rotor support parameters.	88
4.4	Comparison of system parameters.	97
B.1	Parameter values for the calculation of the imbalance.	121
B.2	Estimated imbalance parameters for the different number of washers removed. .	121

List of Figures

1.1	Imbalance diagram for a planar rotor.	2
1.2	Two-plane balancing procedure.	3
1.3	Schematic diagram of an automatic ball balancer.	4
1.4	Schematic diagram of a Jeffcott rotor.	6
1.5	Frequency response of an unbalanced Jeffcott rotor.	8
1.6	Relative positions of the whirl centre O , geometric centre C and centre of mass G for different operating speeds.	9
1.7	The first automatic balancer.	10
1.8	Comparison of autobalancers.	13
2.1	Schematic diagram of a two-plane automatic balancer.	18
2.2	Definition of the co-ordinate system.	19
2.3	Definition of the imbalance.	21
2.4	Schematic diagram of the steady states for the static imbalance case.	30
2.5	Bifurcation diagrams for the static imbalance case upon variation of the rotation speed Ω , and the ball mass m	32
2.6	Two-parameter bifurcation diagrams, upon variation of the parameters: (a) ε against Ω , (b) c against Ω , and (c) c_b against Ω	34
2.7	Diagram showing stable regions of the balanced state upon variation of the parameters ε against Ω , whilst m is also varied so that $m = \varepsilon$	35
2.8	Schematic diagram of the steady states for the couple imbalance case.	36
2.9	Bifurcation diagrams for the dynamic imbalance case.	37
2.10	Two-parameter bifurcation diagrams, upon variation of the damping parameters.	39
2.11	Numerical simulations showing vibration levels for the static imbalance case.	40
2.12	Influence of ball damping c_b on the support vibrations and ball positions.	42
2.13	Numerical simulations for the dynamic imbalance case showing vibration levels \bar{A}_1 above the ball positions α_k	43
3.1	One parameter bifurcation diagrams in m that illustrate the unfolding of the pitchfork bifurcation at which the balanced state is born.	53

3.2	Physical and abstract realisations of the symmetry group that illustrates the isomorphism $\Gamma \cong \mathcal{D}_4$ for the case of a static imbalance.	55
3.3	Plots of $\kappa(\Omega)$	60
3.4	Bifurcation diagrams for the normal form of the \mathcal{D}_4 -equivariant pitchfork bifurcation for various regions in the (a_1, a_2) plane.	62
3.5	Comparison of the unfolding of the \mathcal{D}_4 -equivariant pitchfork for the full and reduced systems.	64
3.6	Comparison of the ABB stability regions for gyroscopically uncoupled and coupled rotors.	67
3.7	Stability chart for a set-up with anisotropic supports.	69
3.8	'Brute force' bifurcation diagrams for the case of anisotropic supports.	70
3.9	Bifurcation diagrams showing the stable regions of an ABB that has various device asymmetries.	72
3.10	Bifurcation diagrams in the case of a 'long' rotor with a dynamic imbalance. . .	73
3.11	Diagram showing the ball speeds $\dot{\theta}_k$ against rotor speed Ω for a constant acceleration rotor run-up.	75
3.12	Simulations which include the effect of the rotor run-up.	76
4.1	Photograph of the experimental rig.	80
4.2	Photograph of the automatic balancer.	81
4.3	Finite element model of the rotor.	83
4.4	Measured response of the plain rotor with a 3-washer imbalance.	86
4.5	Comparison of the measured response with theory for the plain rotor with a 3-washer imbalance.	87
4.6	Measured response of the rotor with 2 balls in the ABB disk and an applied imbalance of 3 washers	91
4.7	Measured frequency response and ball positions for the rotor with two balls in the ABB disk and an applied imbalance of 2 washers.	94
4.8	Free body diagram of the ball race contact.	96
4.9	Measured frequency responses for different amounts of removed washers. . . .	99
4.10	Relationship between the vibration amplitude and the amount of imbalance. . .	100
4.11	Comparison of simulations with the measured response for the ABB with a 3-washer imbalance.	101
4.12	Simulated frequency response and ball positions for the automatic balancer with two balls and an applied imbalance of 2 washers.	103
5.1	Rolls-Royce disk balancer.	110
A.1	Schematic bifurcation diagrams in the vicinity of a Hopf bifurcation.	114

A.2	Phase portrait in the bistable region.	115
B.1	Graphical construction used to determine the rotor imbalance.	118
B.2	Schematic diagram showing the directions of the inherent, applied and resultant misalignments together with the applied eccentricity.	120
C.1	Fitting of the support damping parameters.	125

List of Symbols

a_1, a_2	Normal form coefficients	56
\bar{A}_1	Average vibration amplitude at points that are one unit length from C	38
\bar{A}_{\max}	Average of the maximum vibration amplitudes at each bearing	85
B	The balanced steady state	29
c	Damping coefficient	5
c_1, c_2	Damping coefficient of bearings 1 and 2 respectively	18
c_{ij}	Element of the damping matrix	26
\tilde{c}	Ratio between the stiffness and damping matrices	65
c_b	Race damping coefficient	26
c_r	Torque damping coefficient	51
C	Centre of rotation	27
$C\xi\eta z$	Body frame	18
C	Damping matrix	27
$\mathbf{C}_m, \mathbf{C}_d$	Mean and deviatoric damping matrices respectively	51
C1	Steady state solution with coincident balls in both races	29
C3	Steady state solution with coincident balls in one race	29
Ct3	Steady state solution with coincident balls in the top race	53
Cb3	Steady state solution with coincident balls in the bottom race	53
d_{S_i}	Deflection of the i th support	24
D	Autobalancing driving force	4
\mathcal{D}_4	Symmetry group of the square	55
E	Young's modulus	96
\mathbf{f}_I	Mass imbalance vector	49
\mathbf{f}_{b_k}	Ball imbalance vector	49
F	Rayleigh's dissipation function	6
\mathcal{F}	Right hand side function	54
G	Centre of mass	1
$Gp_1p_2p_3$	Principal axes of the moment of inertia	20
H_{cyl}	Hopf bifurcation associated with the cylindrical whirl	31

H_{con}	Hopf bifurcation associated with the conical whirl	31
J	Moment of inertia tensor	18
J_t	Transverse moment of inertia	24
J_p	Polar moment of inertia	24
\tilde{J}_p	Modified polar moment of inertia	51
k	Stiffness, Ball counter when a subscript	5
k_1, k_2	Stiffness of bearings 1 and 2 respectively	18
k_{ij}	Element of the stiffness matrix	25
\mathbf{K}	Stiffness matrix	27
$\mathbf{K}_m, \mathbf{K}_d$	Mean and deviatoric stiffness matrices respectively	51
l_1, l_2	Axial distance from C to bearings 1 and 2 respectively	18
L_2	Euclidean norm	33
m	Mass of the balancing balls	18
m_c	Critical ball mass value	31
m_t, m_b	Critical ball mass values for the top and bottom races respectively	31
M	Mass of the rotor	18
M_f	Moment of rolling friction	96
\mathbf{M}	Mass matrix	27
\mathcal{M}	Generalised mass matrix	54
n_w	Number of washers removed from the pre-balanced disk	84
N	Normal reaction force	4
O	Whirl centre	5
$OxyZ$	Rotating frame	18
$OXYZ$	Inertial frame	18
PF	Pitchfork bifurcation	31
q_k	k th Lagrangian coordinate	6
\mathbf{q}	Generalised coordinate vector	21
Q	Centrifugal ‘force’	4
r	Ball radius	96
\mathbf{r}	Vector of the complex vibrational coordinates in the rotating frame	50
\mathbf{r}_C	Position vector of the centre of rotation	5
\mathbf{r}_G	Position vector of the centre of mass	6
\mathbf{r}_{b_k}	Position vector of the k th ball	21
R	Race radius	18
\mathbf{R}	Rotation matrix	19
\mathbf{s}	Vector of the complex vibrational coordinates in the space frame	50
S_1, S_2	Location of supports 1 and 2 respectively	18
t	Time	6

T	Kinetic energy	6
\mathbf{u}	State space vector	54
v_1, v_2	Normal form variables	56
V	Potential energy	6
W	Hysteretic energy loss	96
x, y	Rotating frame translational degrees of freedom	19
\mathbf{x}	Vector of the rotating frame vibrational coordinates	27
X, Y	Space frame translational degrees of freedom	50
\mathbf{X}	Vector of the space frame vibrational coordinates	50
z_k	Axial displacement of the k th balancing ball	18
α_k	Angle of the k th ball with respect to the rotating frame	18
$\bar{\alpha}$	Mean angle of the balls in a race	29
$\hat{\alpha}$	Deviatoric angle of the balls in a race	29
$\boldsymbol{\alpha}^*$	Balanced state ball positions	65
β	Phase angle between the couple and static imbalances	2
γ	Spatial symmetry	54
Γ	Symmetry group	55
δ	A small quantity	25
ε	Eccentricity	1
θ_0	Rotor angle	18
θ_k	Angle of the k th ball with respect to the inertial space frame	51
μ	Bifurcation parameter	54
μ_f	Rolling friction coefficient	96
ν	Poisson's ratio	96
σ_α	Angular spread of the balanced state ball positions	94
$\tau(\dot{\theta}_0)$	Motor torque	51
ϕ_x, ϕ_y	Rotating frame inclinational degrees of freedom	19
ϕ_X, ϕ_Y	Space frame inclinational degrees of freedom	50
φ	Phase of the amplitude response	7
φ_{c_z}	Phase of the amplitude response in the plane of the disk	102
χ	Misalignment angle	2
Ω	Rotation speed	2
Ω_c	Critical speed	7
Ω_{cyl}	Critical speed associated with the cylindrical whirl	26
Ω_{con}	Critical speed associated with the conical whirl	31
$\boldsymbol{\Omega}$	Angular velocity vector of the rotor	21
$\boldsymbol{\Omega}_r$	Angular velocity vector of the rotating frame	22

Chapter 1

Introduction

Rotating machines can be found everywhere in the modern world. They range from the highly engineered gas turbines that power our factories and aircraft, to everyday household appliances such as fans, washing machines and DVD players. Although these machines serve many different functions and have a wide variety of appearances, one feature that they all have in common is unwanted vibrations. These oscillations lead to noise, reductions in performance and shorter service lives, therefore every effort should be made in order to eliminate any possible sources of vibration.

1.1 Balancing

It has long been known that one of the main causes of vibrations in rotating machinery is mass imbalance. These errors in the mass distribution are usually corrected during a balancing process in which mass is added or removed from specific parts of the rotor. We shall now proceed with a brief overview of this subject; for further details we refer the interested reader to [63, 64].

1.1.1 Single-plane balancing

In a planar system a mass imbalance occurs when the centre of mass G is not coincident with the centre of rotation C , see Figure 1.1. The distance between the two points is called the mass eccentricity ε , and this error leads to an unbalanced centrifugal force that ‘pulls’ upon the shaft and causes deflections that are felt as vibrations at the bearings. In order to reduce these vibrations most ‘disk-like’ rotors will undergo a single-plane balancing procedure before going into operation. This process will typically consist of determining the magnitude and position of the imbalance and then applying a correction weight of an appropriate mass to the opposite side of the rotor. For example, Figure 1.1 shows a set-up with a disk of mass M and radius R . In this case the mass m of the correction weight should be chosen such that $mR = M\varepsilon$.

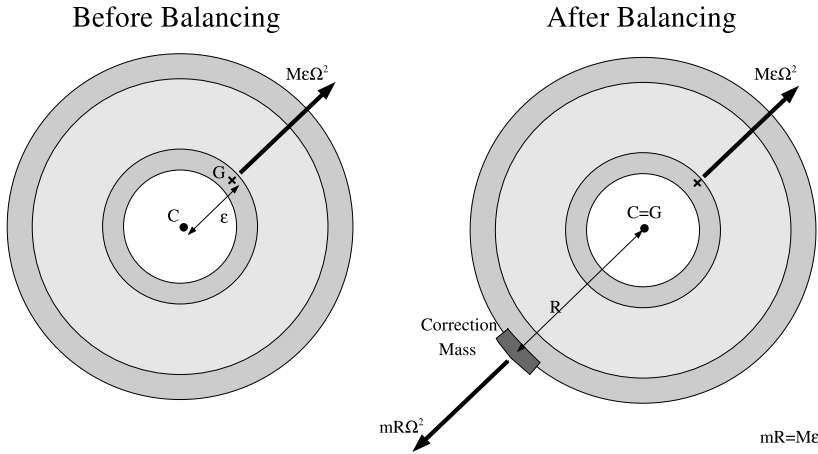


Figure 1.1. Imbalance diagram for a planar rotor of mass M , radius R and rotation speed Ω . When the rotor is unbalanced there is a distance ε between the rotor's centre of mass G and the centre of rotation C . The rotor can be balanced by applying a correction weight of mass m to the opposite side of the rotor, where m is chosen such that $mR = M\varepsilon$.

1.1.2 Two-plane balancing

When the rotor has an appreciable length, the concept of mass imbalance can be generalised to include the effect of misalignment between the principal axis of inertia and the bearing centreline. We now have two distinct types of imbalance and these are illustrated in Figure 1.2. The first is called a *static* imbalance, which occurs when the axis of inertia is displaced from, but remains parallel to, the axis of rotation. This condition gets its name because it can be detected whilst the rotor is at rest; if the shaft is supported horizontally on bearings of negligible friction the heavy spot will move under the influence of gravity and be directed downwards. A static imbalance can be corrected, either by balancing in the single-plane perpendicular to the shaft and containing the centre of mass, or by balancing in two distinct correction planes, see Figure 1.2. The other type of imbalance is of the *couple* type and occurs when the principal axis of inertia intersects the axis of rotation but is misaligned to it by an angle χ . To eliminate a couple imbalance two balancing planes must be used, as the correction masses are placed on opposite sides of the rotor in order to produce a restoring couple. (In this thesis we do not consider rotors with more than one shaft, therefore, all references to *misalignment* will relate to the misalignment χ between the principal axis of inertia and the axis of rotation).

Typically a ‘long’ rotor will suffer from both types of imbalance and this condition is called a *dynamic* imbalance. For a rigid rotor this is the most general form of imbalance, and it can be characterised by the triple $(\varepsilon, \chi, \beta)$, where ε is the eccentricity, χ is the misalignment and β is the phase angle from the plane containing the misalignment to the direction of the eccentricity.

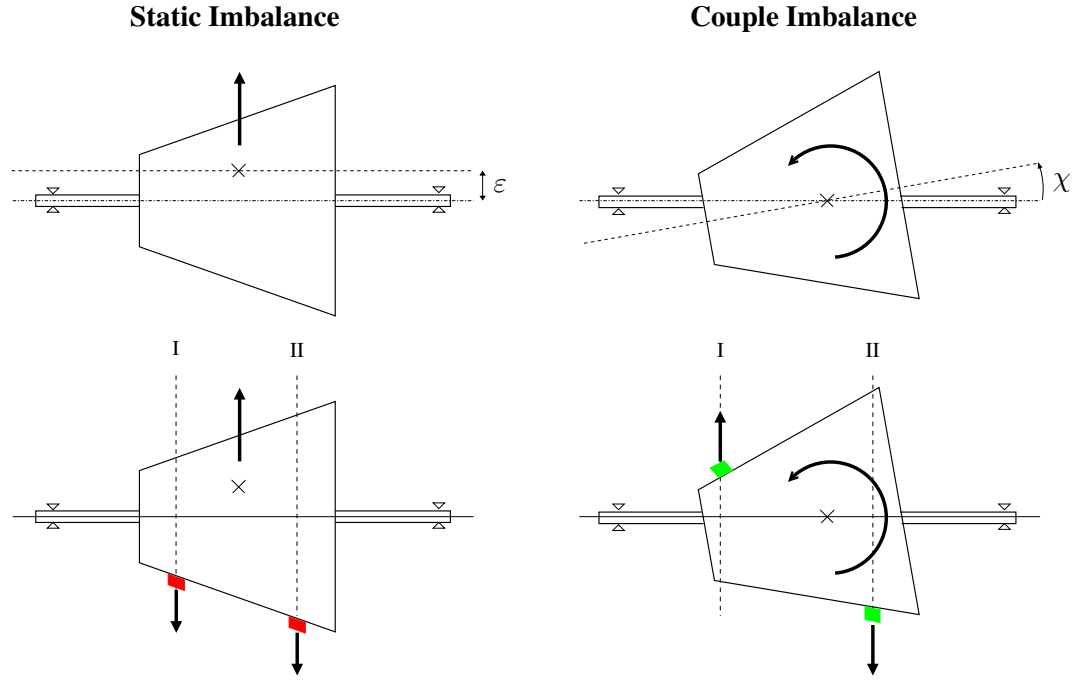


Figure 1.2. Two-plane balancing procedure. Schematic diagrams showing how both static and couple imbalances can be corrected by adding masses in two balancing planes, adapted from [64, §2.7].

A dynamic imbalance can always be eliminated by using two balancing planes and thus the ‘two-plane balancing’ procedure has become the industry standard for balancing rigid rotors that have an appreciable length. In most circumstances the static imbalance is eliminated first, before subsequently compensating for the couple imbalance. Also, the balancing planes are usually chosen to be as far apart as possible in order that a larger restoring moment can be produced with the same change in mass.

For flexible rotors, which deform under centrifugal loading, it may be necessary to use more than two correction planes. Ideally one would like to balance the rotor continuously in all transverse planes, however, this goal is neither achievable nor required. If a rotor is to operate between its n th and $n+1$ th flexible critical speeds, then it should normally be balanced with respect to its first $n+1$ mode shapes and this will generally require $n+1$ balancing planes [24, Appx.B]. In practice each disk-like component of a complex rotor will be pre-balanced before assembly and then the rotor as a whole will undergo a subsequent balancing procedure in two or more correction planes.

1.1.3 Traditional balancing

At present, most balancing operations are carried out ‘off-line’ on highly specialised balancing machines that calculate the required size and position of the correction masses. The balanc-

ing engineer will then add or remove the correction masses as instructed and will repeat the process until the rotor is within its balance tolerances. However, even with the aid of modern balancing machines, this procedure is expensive, time consuming and technically challenging. In addition, if the imbalance of the rotor changes over time then it may need to be taken out of service in order to be rebalanced. This drawback of traditional balancing techniques motivates the study of ‘on-line’ balancing devices, in which the balancing masses are redistributed whilst the rotor is operating.

1.1.4 Automatic balancing

‘On-line’ balancing mechanisms may be classified as either active or automatic. In an active system the vibrations are measured with sensors, and balancing masses are moved into position via a control law and actuator [66, 9, 61]. By contrast, an automatic balancer is a passive device whereby the masses are carried to their compensating positions solely through the influence of the rotor vibrations. Therefore, with an automatic balancer there is no need for any sensors, actuators or power supplies and as a result they are lighter, cheaper and have a simpler design than their active counterparts. (We note that some active systems are also described as ‘automatic’, however, in this thesis an automatic balancer will always refer to a passive device and this terminology is consistent with most of the references).

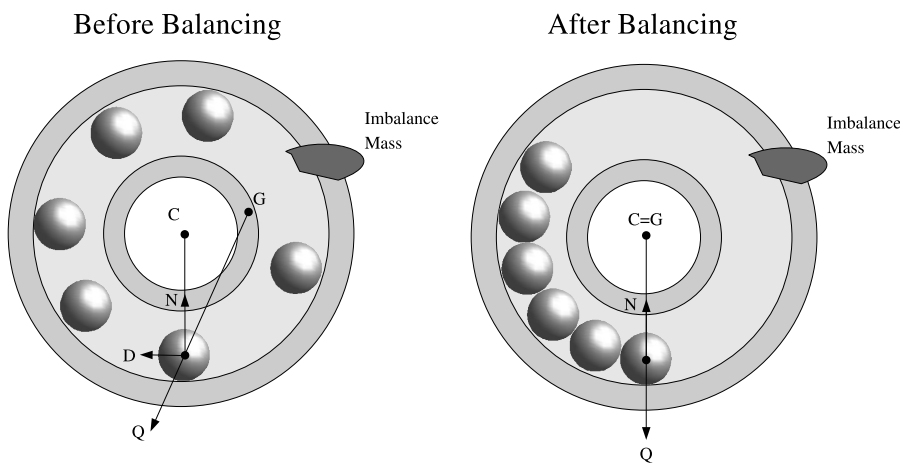


Figure 1.3. Schematic diagram of an automatic ball balancer (ABB), adapted from [18]. Here C is the centre of rotation, G is the centre of mass and Q , N and D are the centrifugal, normal reaction and automatic balancing forces respectively. Further details will be given later in Section 1.3.

The key idea of an automatic balancer is to deploy a series of masses that are free to rotate at a fixed distance from the shaft. Although the masses can take many different forms such as rings, liquids, balls and pendulums, the operating principle of all these mechanisms are largely

the same. We shall focus mainly on the automatic ball balancer (ABB) as this device is both the easiest to analyse and also the type of balancer that is most commonly found in applications.

In recent years ABBs have been applied to optical disc drives, washing machines and power tools such as lathes and angle grinders [35, 2, 47]. In all these applications the imbalance of the rotor changes throughout the operating cycle of the machine. In optical disc drives and washing machines this occurs as a result of changing the discs and washing loads respectively, whereas for power tools the variation in the imbalance arises primarily from the material erosion of the cutting surface. The mass distribution of a rotor can also change for various other reasons, for example, thermal deformation, rotor flexibility or dirt attaching itself to the system. Thus, as the understanding of automatic balancers improves we hope that this technology will be applied to an increasing number of applications, which may come to include fans, centrifuges and gas turbines.

A schematic diagram of an ABB is shown in Figure 1.3. Initially the balls are spread evenly about the race, however once the rotor is operating the balls tend to move to the opposite side of the imbalance and thus act to balance the rotor. Before we can explain why and under what conditions the ABB should work, we shall first need to introduce one of the basic models of rotordynamics.

1.2 Review of a Jeffcott rotor

The Jeffcott rotor model [36] is the simplest system that can be used to investigate the lateral vibrations of a rotor. Nevertheless, a consideration of its frequency response will still provide some insight into the underlying working principle of the ABB.

1.2.1 Derivation of the equations of motion

The Jeffcott rotor set-up consists of a two-degree-of-freedom (2DOF) unbalanced disk that is confined to rotate in the plane at a constant speed Ω , see Figure 1.4. The point G represents the disk's centre of mass and it is located at a distance ε from the geometric centre of the shaft C . In addition, we assume that the rotor is supported on an isotropic suspension with stiffness k and damping coefficient c . The equations of motion can either be derived via a direct application of Newton's second law [64, §2.3] or by using Lagrange's method [24, §2]. Here we shall use the latter approach as it will also be employed to formulate the more complicated ABB systems of the next few chapters. We choose generalised coordinates X, Y that describe the position of the geometric centre C , i.e. $\mathbf{r}_C = (X, Y)$. The position vector and velocity of the centre of

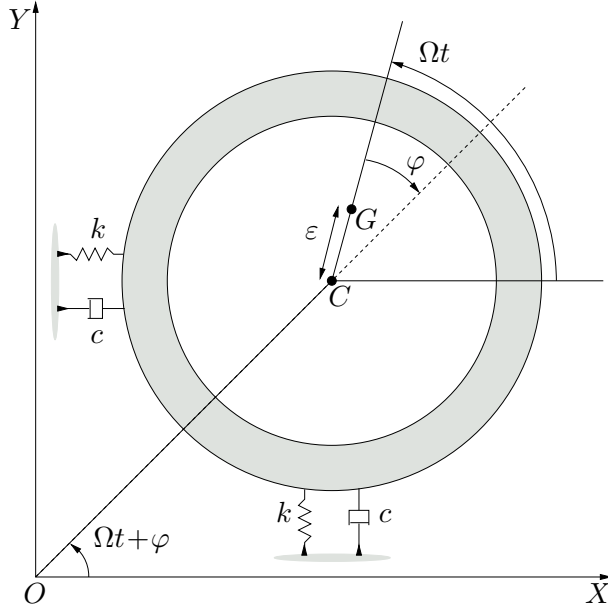


Figure 1.4. Schematic diagram of a Jeffcott rotor on an isotropic suspension, see the text for definitions of the variables.

mass G can then be written respectively as

$$\mathbf{r}_G = \begin{bmatrix} X \\ Y \end{bmatrix} + \begin{bmatrix} \varepsilon \cos(\Omega t) \\ \varepsilon \sin(\Omega t) \end{bmatrix}, \quad \text{and} \quad \dot{\mathbf{r}}_G = \begin{bmatrix} \dot{X} \\ \dot{Y} \end{bmatrix} + \begin{bmatrix} -\varepsilon \Omega \sin(\Omega t) \\ \varepsilon \Omega \cos(\Omega t) \end{bmatrix}.$$

The kinetic energy of the system is thus

$$T = \frac{1}{2} M |\dot{\mathbf{r}}_G|^2,$$

and the potential energy V and dissipation function F can also be easily expressed as

$$V = \frac{1}{2} k (X^2 + Y^2), \quad \text{and} \quad F = \frac{1}{2} c (\dot{X}^2 + \dot{Y}^2).$$

The equations of motion can now be derived through an application of Lagrange's equations

$$\frac{d}{dt} \left(\frac{\partial T}{\partial \dot{q}_k} - \frac{\partial V}{\partial q_k} \right) - \left(\frac{\partial T}{\partial q_k} - \frac{\partial V}{\partial \dot{q}_k} \right) + \frac{\partial F}{\partial \dot{q}_k} = 0,$$

where the q_k are the generalised co-ordinates, which in this case are X and Y . After performing the necessary calculations, and remembering that the spin speed Ω has been taken as a constant,

the system can be written as follows

$$\begin{aligned} M\ddot{X} + c\dot{X} + kX &= M\varepsilon\Omega^2 \cos(\Omega t), \\ M\ddot{Y} + c\dot{Y} + kY &= M\varepsilon\Omega^2 \sin(\Omega t). \end{aligned} \quad (1.1)$$

It is clear from the form of the above equations that we have derived a two-dimensional mass-spring-damper system that is excited by a synchronous rotating centrifugal force of magnitude $M\varepsilon\Omega^2$.

1.2.2 Steady state frequency response

The steady state response can be found by seeking a solution of the form

$$\begin{aligned} X &= A \cos(\Omega t + \varphi), \\ Y &= A \sin(\Omega t + \varphi), \end{aligned}$$

and substituting it into (1.1). By comparing the respective coefficients of $\cos(\Omega t + \varphi)$ and $\sin(\Omega t + \varphi)$ on both sides of the equations, the expressions for the amplitude A and phase φ can be given as

$$\begin{aligned} A &= \frac{\varepsilon\Omega^2}{\sqrt{(\Omega_c^2 - \Omega^2)^2 + (c\Omega/M)^2}}, \\ \tan \varphi &= \frac{-c\Omega/M}{\Omega_c^2 - \Omega^2}, \end{aligned}$$

where

$$\Omega_c = \sqrt{\frac{k}{M}},$$

is the critical speed of the rotor.

The frequency responses of the amplitude and phase are shown for various values of the damping coefficient in Figure 1.5. As the damping increases, the maximum amplitude in the neighbourhood of the critical speed diminishes. In addition, the resonance peak becomes ‘smoother’ and also shifts to the right. This behaviour is characteristic of a vibrating system that is subject to a harmonic excitation whose amplitude is proportional to the square of the frequency. If the forcing amplitude was independent of the frequency, then the damped resonance peak would lie to the left of the critical speed.

In the undamped case, the phase of the response is 0° for $\Omega < \Omega_c$ and -180° for $\Omega > \Omega_c$. However, when damping is present the phase angle changes continuously and always has the value -90° at $\Omega = \Omega_c$. With regards to automatic balancing, the main point to note is that for sufficiently high rotation speeds the response is out of phase with the excitation and the

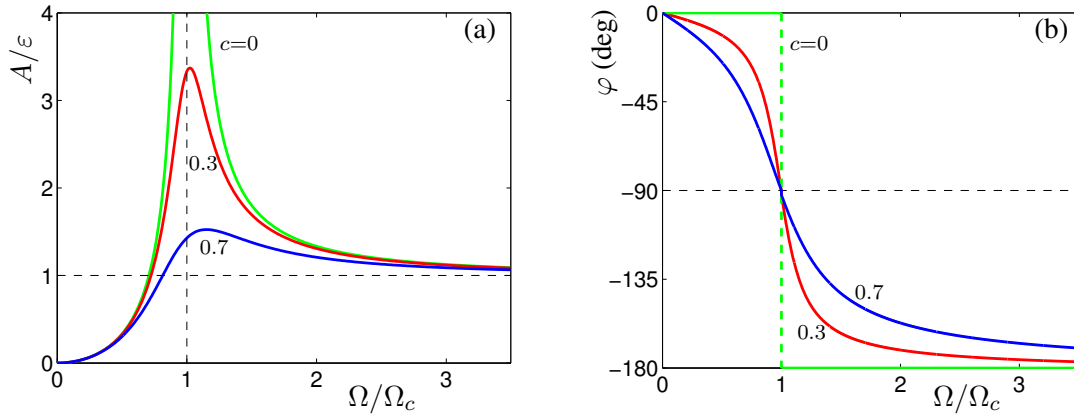


Figure 1.5. Amplitude and phase response of an unbalanced Jeffcott rotor for various values of the damping coefficient c .

amplitude of vibrations tends to ε . Physically this means that the centre of mass G approaches the whirl centre O as the rotation speed tends to infinity. This phenomenon is usually referred to as *self-centering* and indicates that for highly supercritical speeds the rotor acts to rotate about its centre of mass instead of its geometric centre.

1.3 The working principle of the ABB

In order that we may understand the importance of the self-centering effect in relation to successful ABB operation, let us now introduce two (almost massless) balancing balls that are free to rotate around a race that is centered at C . This set-up is illustrated schematically for three different rotation speeds in Figure 1.6. In all cases, there is a centrifugal ‘force’ that acts outwards from the whirl centre O , a normal reaction force that points towards the geometric centre C , and a resultant driving force D that leads to the motion of the balls with respect to the race. For subcritical speeds the phase φ is close to 0° and so the heavy side of the disk is on the outside of the whirl radius. Therefore the balls are directed towards the heavy spot and act to increase the imbalance. By contrast, for supercritical speeds $\varphi \approx -180^\circ$ and so the rotor operates with its light side out, thus the balls move away from the imbalance and act to balance the rotor.

The above explanation for the working principle behind the operation of the ABB was first put forward in 1932 by Thearle [60], and has also been described more recently in various studies on automatic balancers [30, 62, 65, 32]. However, this static analysis does not consider the motion of the balls or the dissipative effect of the race damping. Therefore one may come to the wrong conclusions with regards to the stability of the balanced state. Nevertheless, the connection between the self-centering effect and the performance of the ABB is clear.

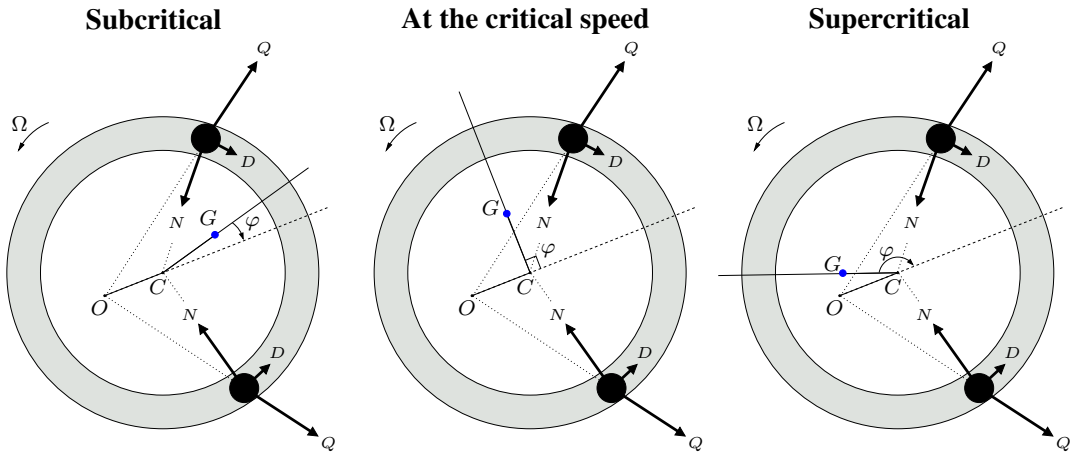


Figure 1.6. Relative positions of the whirl centre O , geometric centre C and centre of mass G for three different operating speeds. During subcritical operation the phase (lag) angle φ is small and so the points O , C and G are aligned in that order. As the frequency passes through the critical speed, point G tends to O in a process called *self-centering*. The forces on a pair of imaginary (almost massless) balancing balls are also shown. Here, Q is the centrifugal ‘force’, N is the normal force and D is the resultant driving force.

The working principle of the ABB can also be extended to rotor systems that are more complicated. For example, in a four-degree-of-freedom (4DOF) rotor model that includes tilting motions, an equivalent self-centering phenomenon will also occur. For high enough rotation speeds that are above both natural frequencies, the principal axis of inertia will coincide with the bearing centreline [64, §2.4]. Thus by using two ABBs in two distinct planes one may expect that we could compensate for both the static and also the couple imbalances. In order to assess the effectiveness of such a proposal, we shall investigate a two-plane ABB set-up in the next chapter. However, before we move on to a presentation of original research, we shall first set the scene by giving a brief overview of the autobalancing literature.

1.4 Review of previous work

The first documented account of an automatic balancer was given in 1872 by Albert Fesca in his patent entitled ‘Improvement in Centrifugal Machines for Draining Sugar’ [21], see Figure 1.7. Here he describes a device in which three rings are hung loosely on a central vertical shaft. Initially the rings are set 120° apart so that they are mutually balanced (a), however once the machine was operating the rings were found to move under the influence of the machine’s vibrations and position themselves in such a way as to compensate for the rotor’s mass imbalance. No reason as to why the rings should behave in this manner was given, nevertheless in his description of the machine Fesca notes that it was set on rubber blocks

and supported with rubber springs. Therefore, we may assume that the set-up had relatively low stiffnesses and critical speeds. Thus, it was in all likelihood capable of operating in the self-centered, supercritical frequency regime.

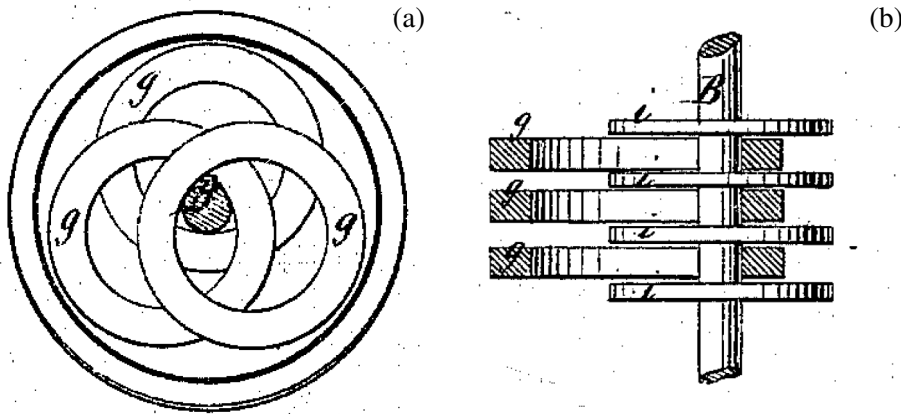


Figure 1.7. Diagram of A. Fesca's ring balancer invention reproduced from his original patent of 1872 [21], here B denotes the shaft, g the balancing rings and i the fixed disks. Panel (a) shows a plan view of the device with the three rings in their mutually balanced configuration. A side view is given in (b), here the rings are all on one side and we can see how they are separated by fixed disks.

During the early part of the 20th century similar ring balancers were also applied to steam turbines and centrifugal separators [54, 41]. Then in 1912, Maurice Leblanc proposed a new balancing device in which a heavy liquid such as mercury was used to compensate for the imbalance [39, 40]. In addition Leblanc discussed various alternative designs, which included utilising a tin alloy that would only be free to move when heated, and also, using a cement like substance that would set firm whilst it was in the balanced state. The years that followed led to many further proposals for automatic balancing devices, for example, Louden [43] envisaged a ball balancer in which a series of ‘floats’ were free to travel around a fluid filled race. Despite these practical advances, the conditions under which the automatic balancers would compensate for a mass imbalance remained largely unknown. This was mainly due to the poor understanding at the time of the underlying rotordynamics.

The first research paper on an automatic balancing system was presented in 1932 by Ernest Thearle [60]. He proposed a two-ball balancer that was equipped with a hand operated clamp and fitted to a balancing machine. The rotor was brought to an operating frequency 45% above that of the first rigid-body resonance and at this speed the balls were released via a clutch mechanism. After the balls moved to positions that reduced the vibration levels sufficiently, they were then re-clamped in order that the rotor would remain balanced. As discussed in Section 1.3, Thearle demonstrated the existence of a stable steady state at rotation speeds above the first critical frequency. However, his argument was based on a static analysis that did not

consider the momenta of the balls. With this approach one might conclude that operation above the critical speed is also a sufficient condition for the stability of the ABB, however, with a dynamic stability analysis this conclusion can be shown to be incorrect [14].

In 1977, Hedaya and Sharp [30, 29] proposed a two-plane balancing device that would compensate for both rotor eccentricity and misalignment. Here a linear dynamic analysis was presented together with some experimental results. The stability of the device was shown to have a complicated relationship with the system parameters and the importance of the race damping parameter was also highlighted.

1.4.1 Contemporary theoretical studies

More recently, the equations of motion for a planar Jeffcott-type ABB have been derived using Lagrange's method [42, 14, 28]. In particular, Chung and Ro [14] used rotating coordinates to obtain an autonomous system of governing equations. A linear stability analysis based on perturbation methods was then performed and their findings were supplemented with direct simulations of the full nonlinear system. In addition, the influence of the rotation speed and race damping were also discussed.

The first nonlinear bifurcation analysis of an ABB was provided by Green *et al.* [28]. In this study, numerical continuation techniques were used in order to find Hopf bifurcations that denote the onset of instabilities in the system's steady state behaviour. These bifurcations were followed as the parameter values were varied smoothly. In this way, the regions of stability of the ABB's balanced state were efficiently mapped out in parameter space. The same approach was applied to limit cycle solutions, and regions of bistability were found in which the balanced state coexists with solutions that have less desirable oscillatory ball motions. For further details on numerical continuation techniques and on bifurcation theory in general, see for example [38] and [59]. In addition, the physical interpretation of the ABB dynamics in the vicinity of a Hopf bifurcation is provided in Appendix A.

As mentioned above, it has long been suggested that ABBs could be used in a two-plane balancing procedure to correct for both the mass eccentricity and rotor misalignment [30]. In order to evaluate this proposal, the ABB model must be based on systems which include out-of-plane tilting vibrations.

Sperling *et al.* [56, 58] derived the governing equations for a two-plane balancer by using linearised vibrational coordinates. The stability of the balanced state was then analysed by averaging the ball motions over the fast time scale of the vibrational oscillations. This approximate method, also known as direct separation of motion [5], suggests that rotation speeds above the highest natural frequency is a sufficient condition for the asymptotic stability of the balanced state. However, this conclusion did not hold for the full system and simulations showed that

the ‘border’ speed for successful operation was above the highest natural frequency, and also depended on the support damping and ball parameter values.

Next, Chung and Jang [13] considered the out-of-plane motions of a single-plane ABB set-up with shaft flexibility. Here a time independent system of governing equations was derived through the use of the rotating frame and Euler angles. However, the ABB was fitted in the plane of the eccentricity and there was also no rotor misalignment. This meant that although tilting motions were allowed, their modes were not excited. Therefore, the second critical speed had no effect on the stability of the balanced state, and so the results were largely the same as those for the planar Jeffcott case. Another study by Chao *et al.* [8] considers the out-of-plane motions of a specific optical disk drive set-up. Although simulations were provided, the equations were written with respect to a fixed reference frame. Therefore, they had time periodic coefficients and were not readily amenable to a stability analysis. Finally, Kim *et al.* [37] modelled a similar disk drive system that was also fitted with a single-plane ABB. Here, Floquet theory was used to provide a linear stability analysis and stability charts were produced through the use of ‘brute-force’ computations.

Further studies consider the effects of imperfections in the ABB system itself. For example, it has been shown that a rotor fitted with an ABB has a vibrational amplitude that is bounded below by the race eccentricity [35, 45]. Therefore, it is important that the ABB race be manufactured and fitted to an accuracy high enough to enable the eccentricity of the runway to be less than the eccentricity of the mass imbalance. It has also been noted that for a well balanced rotor system, using two balls of different masses will always lead to an increase in vibrations [33]. This is because the balls cannot compensate for each other by residing on opposite sides of the race.

1.4.2 Contemporary experimental investigations

Recently, experimental research has focused on systems that have been tailored towards use in specific applications such as hand held power tools [47], washing machines [2, 4] and optical disk drives [11].

A sample of some modern automatic balancer set-ups have been gathered together in Figure 1.8. Panel (a) shows an automatic balancer fitted to a commercial DVD-ROM drive in which a series of many small balls occupy just under half the capacity of the runway. In such disk drive applications an oil lubricated race is highly undesirable as it may damage the optical sensor upon leakage. This constraint has motivated many studies into the effects of dry rolling friction between the race and the balancing balls [10, 62, 65]. In particular, a system with two balls in the race was investigated both theoretically and experimentally by van de Wouw *et al.* [62]. With this study they demonstrated how the friction acts to ‘spread out’ the fixed

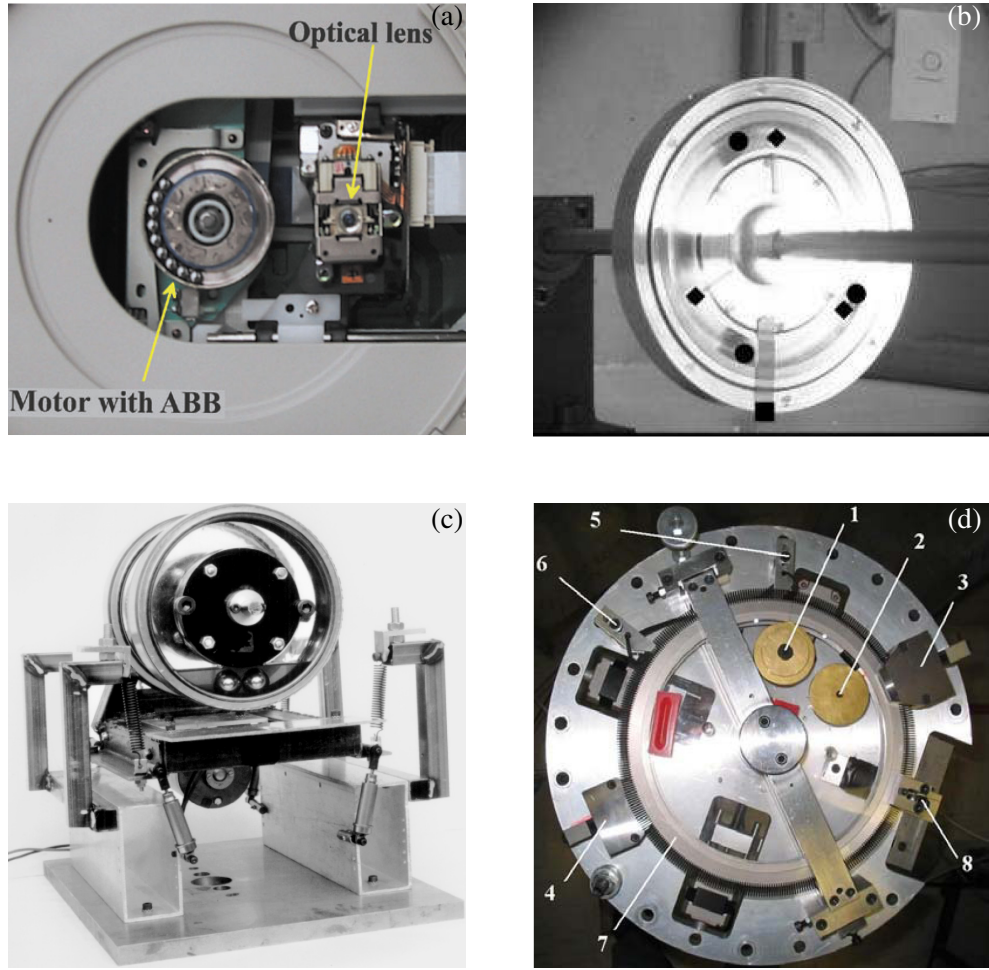


Figure 1.8. Comparison of autobalancers. Panel (a) shows a commercial GDR-8160B DVD-ROM drive of LG electronics, reproduced from [62]. An experimental ABB with partitioned race is shown in (b). Here the dots mark the position of the balls, the diamonds the position of the partitions and the square the position of the imbalance; reproduced from [27]. Panel (c) displays a two-plane ABB based on an experimental Electrolux Wascator washing machine suspension system, reproduced from [2]. A pendulum balancer is shown in (d), see text for details; reproduced from [33].

points so that they form equilibrium sets of open intervals on the race. This effect leads to ball positioning errors, and as a consequence, the performance of the ABB is reduced.

An analytical and experimental investigation on a multi-ball system with a partitioned race was carried out by Green *et al.* [27]. The set-up, shown in Figure 1.8 (b), comprises of a large rotor in which the race has been partitioned into three sectors containing one ball each. The motion of the balls was observed with the aid of a strobe light, however, large vibration amplitudes at the first critical speed prevented observations of the ABB dynamics beyond the main resonance. Nevertheless, a non-smooth mathematical model was developed in order to

describe the impacts of the balls with the partitions.

Figure 1.8(c) shows a two-plane automatic ball balancer that has been fitted to an experimental washing machine suspension system [2]. Each race contains two balls that are immersed in fluid, and this type of set-up can compensate both for the rotor eccentricity and also for the rotor misalignment. A more recent experimental study into non-planar tilting effects was carried out by Chao *et al.* [11]. Here, an optical disk drive equipped with a single plane balancer was considered, and the vibration levels of the rotor were observed as it passed through multiple resonances. Although these results are promising, the body of experimental evidence for the effective operation of an ABB device remains scarce. In particular, data for the performance of the ABB in the highly supercritical frequency range is still unavailable.

As discussed previously, one of the main limitations that precludes the widespread use of ABBs in many industrial applications is the detrimental effect of runway friction on the performance of the balancer. This drawback of the ABB motivated Horvath *et al.* [33, 32] to investigate a different type of automatic balancer that uses pendulums as the balancing masses, see Figure 1.8(d). Here, two pendulums (1-2) are attached to separate plexi-glass disks that run on independent bearings. Optical sensors (5-6) measure the positions of the pendulums and a constraint system (8) allows them to be locked in place and then released whilst the rotor is in operation. In addition, the motions of the pendulums are damped by magnets (3-4) that act on the aluminium rims (7) of the disks. This set-up was found to perform better in tests than an equivalent ABB system and this result was shown to occur as a consequence of ball positioning errors due to race friction. Although for certain applications this outcome seems to favour using pendulums instead of balls, the underlying principle for both devices is the same. In particular their equations of motion are identical when both the race friction of the ABB is neglected and the pivot points of the pendulums are taken to be at the centre of rotation.

1.5 Aims and organisation of the thesis

The motivation behind this research is to improve the understanding of automatic balancers so that in time they can be incorporated into rotating machines of a greater complexity. Specifically, we shall extend the ABB model so that it includes the effect of out-of-plane tilting motions and couple type imbalances. Furthermore, the influence of device asymmetries should be determined and an experimental proof of concept provided. With these points in mind, the outline of the thesis is as follows.

In Chapter 2, an analysis of a two-plane automatic balancer is presented. This device is capable of compensating for imbalances of both the static and couple types. Autonomous governing equations are derived through the use of rotating coordinates and the steady states of this

system are determined. Next, a particular symmetric set-up is considered, and numerical continuation techniques are employed in order to map out the stability boundaries of the balanced state in various parameter planes. Finally, the results of the stability analysis are supplemented with simulations, and we demonstrate the coexistence of a stable balanced state with other less desirable dynamics.

In Chapter 3 the ABB model is extended by including effects such as support anisotropy and rotor acceleration. The symmetry of the imbalance is considered, and techniques from equivariant bifurcation theory are used in order to derive a necessary condition for the stability of the balanced state. Next, the unfolding of the solution structure is explored and we investigate mechanical set-ups in which either the supports or the ABB device are asymmetric. Here it is shown that, provided the imbalance is small, the balanced state is robust to the considered asymmetries. Finally, we build upon the results of the stability analysis by providing simulations of the ABB dynamics that also include the influence of rotor run-up.

In Chapter 4 we present an experimental study of a specific ABB system. The design of a lightweight table top rig is described, and this set-up is shown to be capable of operating in the far supercritical frequency regime. Next, the parameters of the rotor are measured, and these values are validated by comparing experimental and simulated frequency response curves. The performance of the ABB is assessed for a variety of different imbalances and a reduction in the vibration level is consistently demonstrated for sufficiently high rotation speeds. For lower speeds the coexistence of steady state and more complex dynamics is also observed, and we show that this behaviour can be replicated by the ABB model.

Finally, in Chapter 5 we summarise and assess the results of the previous chapters. Possible directions for future research are identified, and we also provide design guidelines for the implementation of ABBs in ‘real-world’ machines.

Chapter 2

Automatic two-plane balancing

The results that are presented in this chapter have been published in [49].

In this chapter we present an analysis of a two-plane automatic ball balancer (ABB) that is capable of compensating for both static and couple type mass imbalances. This device was originally proposed in 1977 by Hedaya and Sharp [30], and has also been subsequently investigated by Sperling *et al.* [58]. However, in those works, only approximate linear stability analyses were provided. Because the ABB is a highly nonlinear device, such techniques are unable to accurately predict the requirements for the stability of the balanced state. To this effect, we shall derive the first fully geometric nonlinear model of a two-plane ABB. Furthermore, we shall use numerical continuation tools to deliver the first, nonlinear bifurcation analysis of the dynamics of such a system.

The rest of this chapter is organised as follows. In Section 2.1 we use rotating coordinates to derive an autonomous set of governing equations for the motion of an isotropically mounted rotor that is fitted with a pair of ABB devices. The steady states of the system are then considered in Section 2.2, and we focus on using numerical bifurcation theory to investigate the effect that the physical parameters have on the stability of the balanced state. Finally, in Section 2.3 we supplement the findings of the bifurcation analysis by providing numerical simulations of the dynamics, and also by investigating the effects of varying the initial conditions.

2.1 Derivation of the equations of motion

We shall derive an autonomous system of governing equations for the automatic balancer system depicted in Figure 2.1, by describing the position of the rotor centre with respect to rotating coordinates and then applying Lagrange's method [14, 28, 13].

2.1.1 Mechanical set-up

The mechanical device that we wish to model is illustrated in Figure 2.1, and is based on a rigid rotor which has been fitted with a two-plane automatic balancer [30, 58]. The rotor system in the absence of the balancing balls is assumed to have mass M , moment of inertia tensor \mathbf{J} , and to be mounted on two isotropic linear bearings that are located at S_1 and S_2 . The automatic balancer consists of a pair of races that are set normal to the shaft in two separate planes. Each race contains two balancing balls of mass m , which move through a viscous fluid and are free to travel at a fixed distance R from the shaft axis. The position of the k th ball is specified by the axial and angular displacements z_k and α_k , which are written with respect to the $C\xi\eta z$ rotor axes.

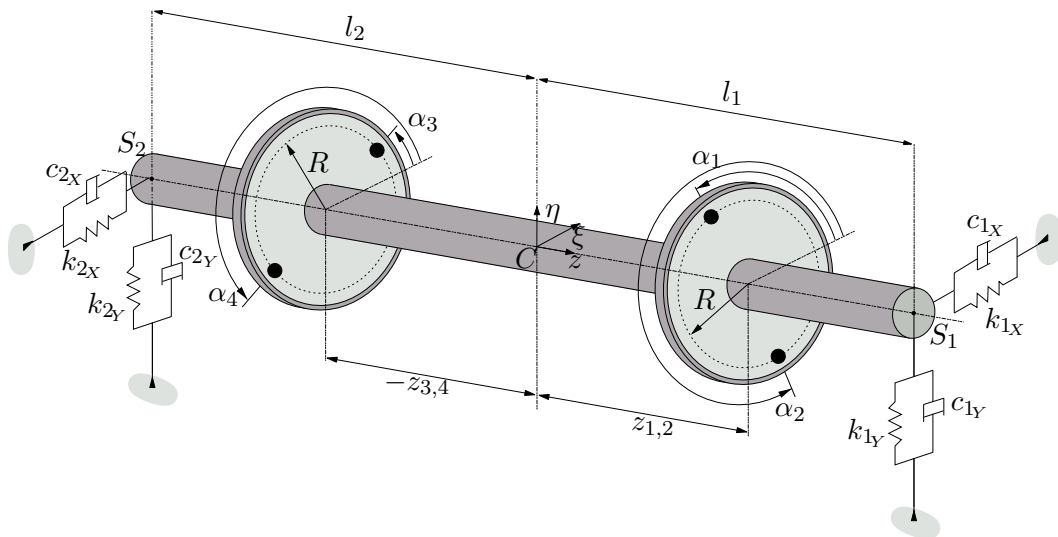


Figure 2.1. Schematic diagram of a two-plane automatic balancer. In this chapter the supports will be assumed to be isotropic, that is $\{k_{1X}, k_{2X}\} = \{k_{1Y}, k_{2Y}\} = \{k_1, k_2\}$ and similarly for the damping terms. In the later chapters these conditions will be relaxed.

2.1.2 Co-ordinate frames

In order to describe the position and orientation of the rotor, it is helpful to consider the following frames of reference, as shown in Figure 2.2. We begin with an inertial *space* frame $OXYZ$ with origin at O , and a Z -axis oriented along the undeflected bearing centreline. A rotation about the Z axis by the spin angle θ_0 results in the *rotating* frame $OxyZ$. This transformation can be written as

$$\mathbf{x} = \mathbf{R}_1 \mathbf{X},$$

where \mathbf{x} and \mathbf{X} are the column vectors of coordinates in the rotating and inertial frames respectively, and

$$\mathbf{R}_1 = \begin{bmatrix} \cos \theta_0 & \sin \theta_0 & 0 \\ -\sin \theta_0 & \cos \theta_0 & 0 \\ 0 & 0 & 1 \end{bmatrix}.$$

The torsional behaviour of the rotor lies outside the scope of this chapter, and so we shall only consider the special case of constant-speed operation, in which $\theta_0 = \Omega t$.

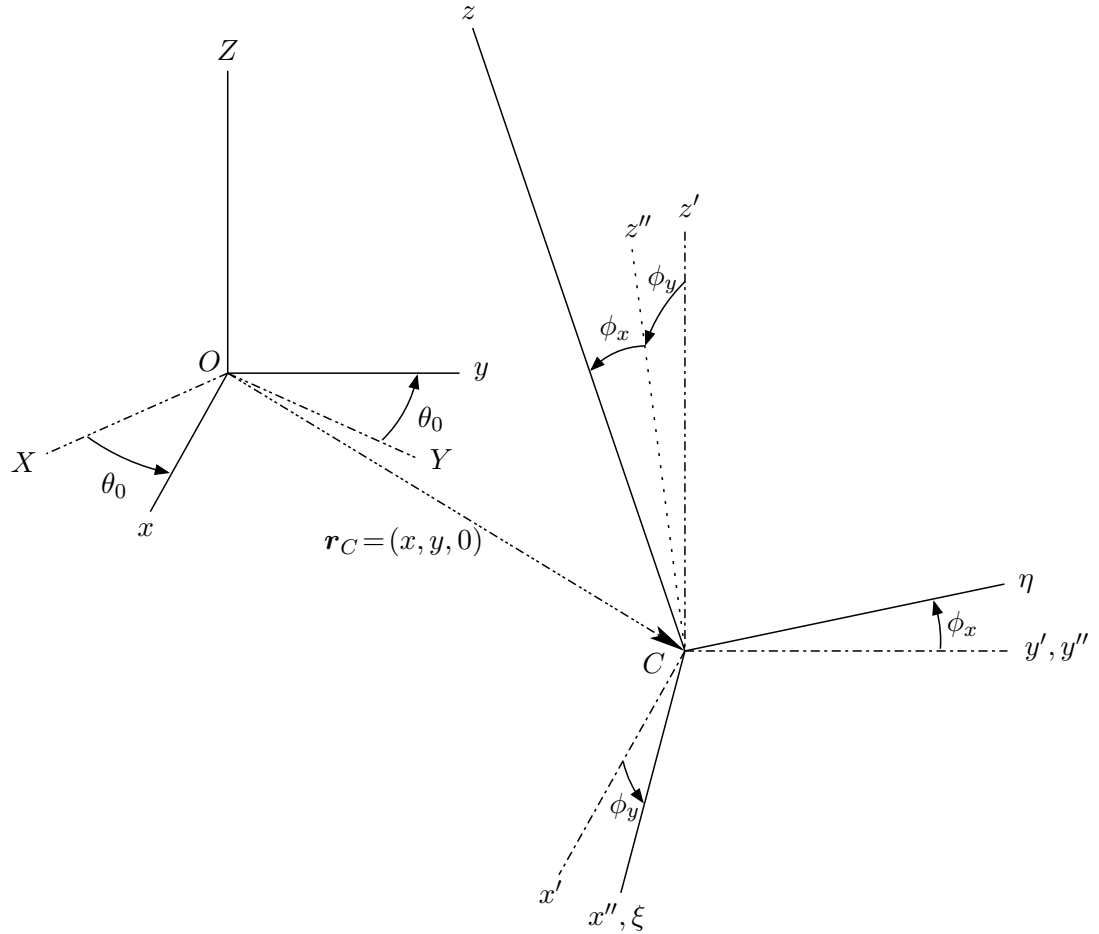


Figure 2.2. Definition of the co-ordinate system.

The rotor's lateral motion can be described by introducing a frame $Cx'y'z'$ with origin at the geometric shaft centre C , and axes parallel to those of the rotating frame $Oxyz$. We neglect any motion in the axial direction, and so the position vector of the geometric centre r_C lies in the x - y plane. The rotor may also perform an out-of-plane tilting motion that can be described as follows: firstly we define an intermediate set of axes $Cx''y''z''$ related to $Cx'y'z'$

by a rotation of an angle ϕ_y about the y' axis, then we rotate $Cx''y''z''$ about x'' by an angle ϕ_x , which results in a *body* frame $C\xi\eta z$ that is fixed with respect to the rotor. These transformations can be combined to give

$$\xi = R_3 R_2 \mathbf{x}', \quad (2.1)$$

where ξ and \mathbf{x}' are the coordinates in the body and primed axes respectively and

$$R_2 = \begin{bmatrix} \cos \phi_y & 0 & -\sin \phi_y \\ 0 & 1 & 0 \\ \sin \phi_y & 0 & \cos \phi_y \end{bmatrix}, \quad R_3 = \begin{bmatrix} 1 & 0 & 0 \\ 0 & \cos \phi_x & \sin \phi_x \\ 0 & -\sin \phi_x & \cos \phi_x \end{bmatrix}.$$

We are now able to transform between body coordinates and the space reference frame, however as shown in Figure 2.3, small errors in the rotor's mass distribution will cause the body axes $C\xi\eta z$ to differ from the principal axes of the moment of inertia. The eccentricity ε , which gives rise to the static imbalance, is defined as the distance between the shaft centre C and the rotor's centre of mass G . Also the symmetry axis p_3 corresponding to the polar moment of inertia may be misaligned to the shaft axis by an angle χ , and this results in a couple imbalance. The symmetry of the rotor enables us to take the misalignment to be about the η axis without detracting from the generality of the model. The matrix expressing this rotation is thus

$$R_4 = \begin{bmatrix} \cos \chi & 0 & -\sin \chi \\ 0 & 1 & 0 \\ \sin \chi & 0 & \cos \chi \end{bmatrix}.$$

Finally, we also include the angle β from the ξ axis to the direction of the eccentricity. This denotes the constant phase between the couple and static imbalances.

Before moving on to the derivation of the Lagrangian, it is worth noting that we have chosen the order of rotations so that the spin Ω is taken about the space Z axis as opposed to the body z axis. In the standard formulation for a linear four-degree-of-freedom rotor, both approaches lead to equivalent equations of motion [24, §3]. However, for our case where we must include the geometric nonlinearities due to the balancing balls, we find that autonomous equations can only be derived when Ω is taken about the space Z axis [48].

2.1.3 Lagrangian formulation

The nonlinear equations of motion for the system are derived from Lagrange's equations

$$\frac{d}{dt} \left(\frac{\partial T}{\partial \dot{q}_k} - \frac{\partial V}{\partial \dot{q}_k} \right) - \left(\frac{\partial T}{\partial q_k} - \frac{\partial V}{\partial q_k} \right) + \frac{\partial F}{\partial \dot{q}_k} = 0, \quad (2.2)$$

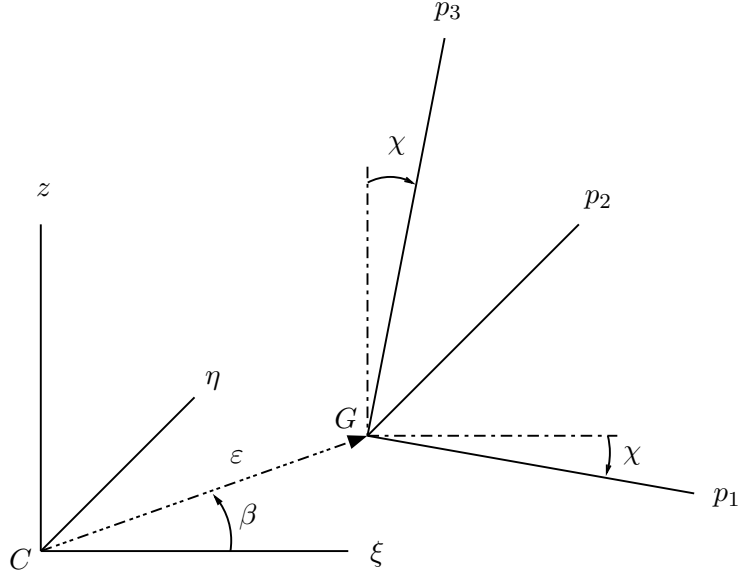


Figure 2.3. Definition of the imbalance.

where T , and V , are the kinetic and potential energies respectively, F is Rayleigh's dissipation function and the q_k are the generalised coordinates. In our case the generalised coordinates are given by

$$\mathbf{q} = (x, y, \phi_x, \phi_y, \alpha_1, \alpha_2, \alpha_3, \alpha_4),$$

and so the motion is governed by a total of eight independent equations of motion. We proceed by deriving in turn the kinetic energy, the potential energy and Rayleigh's dissipation function.

Kinetic energy

The kinetic energy of any rigid body can be decomposed as the sum of the translational energy of the centre of mass and the rotational energy of the body about its centre of mass. By treating the balls as points, the kinetic energy of the system can be written as

$$T = \frac{1}{2}M\dot{\mathbf{r}}_G^2 + \frac{1}{2}\mathbf{\Omega}^T \mathbf{J} \mathbf{\Omega} + \frac{1}{2} \sum_{k=1}^4 m\dot{\mathbf{r}}_{b_k}^2. \quad (2.3)$$

Here $\dot{\mathbf{r}}_G$ and $\dot{\mathbf{r}}_{b_k}$ are the velocities of the rotor's centre of mass and the k th ball respectively, and $\mathbf{\Omega}$ is the angular velocity of the rotor. By using the inverse of the transformation defined

in (2.1), we may write the position vector of the centre of mass, in the rotating frame as

$$\begin{aligned}\mathbf{r}_G &= \begin{bmatrix} x \\ y \\ 0 \end{bmatrix} + \mathbf{R}_2^T \mathbf{R}_3^T \begin{bmatrix} \varepsilon \cos \beta \\ \varepsilon \sin \beta \\ 0 \end{bmatrix}, \\ &= \begin{bmatrix} x + \varepsilon (\cos \beta \cos \phi_y + \sin \beta \sin \phi_x \sin \phi_y) \\ y + \varepsilon \sin \beta \cos \phi_x \\ \varepsilon (-\cos \beta \sin \phi_y + \sin \beta \sin \phi_x \cos \phi_y) \end{bmatrix}.\end{aligned}$$

The rotating coordinates x and y have been chosen to describe the lateral motion because their use enables an autonomous formulation in which the spin angle Ωt does not explicitly enter into the governing equations. The position vector of the k -th ball can be similarly given by

$$\begin{aligned}\mathbf{r}_{b_k} &= \begin{bmatrix} x \\ y \\ 0 \end{bmatrix} + \mathbf{R}_2^T \mathbf{R}_3^T \begin{bmatrix} R \cos \alpha_k \\ R \sin \alpha_k \\ z_k \end{bmatrix}, \\ &= \begin{bmatrix} x + R (\cos \phi_y \cos \alpha_k + \sin \phi_x \sin \phi_y \sin \alpha_k) + \cos \phi_x \sin \phi_y z_k \\ y + R \cos \phi_x \sin \alpha_k - \sin \phi_x z_k \\ R (-\sin \phi_y \cos \alpha_k + \sin \phi_x \cos \phi_y \sin \alpha_k) + \cos \phi_x \cos \phi_y z_k \end{bmatrix}.\end{aligned}$$

In contrast to the eccentricity ε , the race radius R cannot be assumed to be a small quantity. As a consequence, we must take extra care in terms relating to the ball positions when making any small angle assumptions on ϕ_x and ϕ_y . Thus, we prefer to compute the kinetic energy using the complete expressions for the displacements and make any approximations only after the equations of motion have been derived.

When calculating the translational kinetic energies, it is also necessary to express the velocities as they are seen by an observer in a space-fixed frame. Since we have written the position vectors with respect to rotating coordinates, we must use the following operator relation between derivatives to account for the change in frames

$$\left(\frac{d}{dt} \right)_s = \left(\frac{d}{dt} \right)_r + \boldsymbol{\Omega}_r \times .$$

Here the subscripts s and r denote the time derivatives as seen by an observer in the space and rotating frames respectively, and $\boldsymbol{\Omega}_r = [0, 0, \Omega]^T$ is the angular velocity of the rotating frame with respect to an observer fixed in space. Hence, the velocity of the centre of mass in the

space frame is given by

$$\begin{aligned}\dot{\mathbf{r}}_G &= \left(\frac{d\mathbf{r}_G}{dt} \right)_s = \left(\frac{d\mathbf{r}_G}{dt} \right)_r + \boldsymbol{\Omega}_r \times \mathbf{r}_G, \\ &= \begin{bmatrix} \dot{r}_{G,1} \\ \dot{r}_{G,2} \\ \dot{r}_{G,3} \end{bmatrix},\end{aligned}\quad (2.4)$$

where

$$\begin{aligned}\dot{r}_{G,1} &= \dot{x} + \varepsilon \left(-\cos \beta \sin \phi_y \dot{\phi}_y + \sin \beta \left(\cos \phi_x \dot{\phi}_x \sin \phi_y + \sin \phi_x \cos \phi_y \dot{\phi}_y \right) \right) \\ &\quad - \Omega (y + \varepsilon \sin \beta \cos \phi_x), \\ \dot{r}_{G,2} &= \dot{y} - \varepsilon \sin \beta \sin \phi_x \dot{\phi}_x + \Omega (x + \varepsilon (\cos \beta \cos \phi_y + \sin \beta \sin \phi_x \sin \phi_y)), \\ \dot{r}_{G,3} &= \varepsilon \left(-\cos \beta \cos \phi_y \dot{\phi}_y + \sin \beta \left(\cos \phi_x \dot{\phi}_x \cos \phi_y - \sin \phi_x \sin \phi_y \dot{\phi}_y \right) \right).\end{aligned}$$

The velocities of the balls are computed in the same manner, so that

$$\dot{\mathbf{r}}_{b_k} = \begin{bmatrix} \dot{r}_{b_k,1} \\ \dot{r}_{b_k,2} \\ \dot{r}_{b_k,3} \end{bmatrix}, \quad (2.5)$$

with

$$\begin{aligned}\dot{r}_{b_k,1} &= \dot{x} + R \left(-\sin \phi_y \dot{\phi}_y \cos \alpha_k - \cos \phi_y \sin \alpha_k \dot{\alpha}_k + \cos \phi_x \dot{\phi}_x \sin \phi_y \sin \alpha_k \right. \\ &\quad \left. + \sin \phi_x \cos \phi_y \dot{\phi}_y \sin \alpha_k + \sin \phi_x \sin \phi_y \cos \alpha_k \dot{\alpha}_k \right) \\ &\quad + \left(-\sin \phi_x \dot{\phi}_x \sin \phi_y + \cos \phi_x \cos \phi_y \dot{\phi}_y \right) z_k \\ &\quad - \Omega (y + R \cos \phi_x \sin \alpha_k - \sin \phi_x z_k), \\ \dot{r}_{b_k,2} &= \dot{y} + R \left(-\sin \phi_x \dot{\phi}_x \sin \alpha_k + \cos \phi_x \cos \alpha_k \dot{\alpha}_k \right) - \cos \phi_x \dot{\phi}_x z_k \\ &\quad + \Omega (x + R (\cos \phi_y \cos \alpha_k + \sin \phi_x \sin \phi_y \sin \alpha_k) + \cos \phi_x \sin \phi_y z_k), \\ \dot{r}_{b_k,3} &= R \left(-\cos \phi_y \dot{\phi}_y \cos \alpha_k + \sin \phi_y \sin \alpha_k \dot{\alpha}_k + \cos \phi_x \dot{\phi}_x \cos \phi_y \sin \alpha_k \right. \\ &\quad \left. - \sin \phi_x \sin \phi_y \dot{\phi}_y \sin \alpha_k + \sin \phi_x \cos \phi_y \cos \alpha_k \dot{\alpha}_k \right) \\ &\quad + \left(-\sin \phi_x \dot{\phi}_x \cos \phi_y - \cos \phi_x \sin \phi_y \dot{\phi}_y \right) z_k.\end{aligned}$$

Next we turn to the expression for the rotational energy, which is most easily derived by using the principal axes $Gp_1p_2p_3$ of Figure 2.3. It is in this frame that the inertia tensor J , takes

the diagonal form

$$\mathbf{J} = \begin{bmatrix} J_t & 0 & 0 \\ 0 & J_t & 0 \\ 0 & 0 & J_p \end{bmatrix},$$

in which J_t and J_p are the transverse and polar moments of inertia respectively. The angular velocity $\boldsymbol{\Omega}$ is composed from the following three angular velocity vectors: $\dot{\theta}_0$ directed along the Z-axis, $\dot{\phi}_y$ which is directed along the y' axis and $\dot{\phi}_x$ which lies along the x'' axis. The rotation matrices of Section 2.1.2 can now be used to transform these vectors so that they are written with respect to the principal axes, and taking the sum we obtain the angular velocity vector $\boldsymbol{\Omega}$ as

$$\begin{aligned} \boldsymbol{\Omega} &= \mathbf{R}_4 \left[\begin{bmatrix} \dot{\phi}_x \\ 0 \\ 0 \end{bmatrix} + \mathbf{R}_3 \left[\begin{bmatrix} 0 \\ \dot{\phi}_y \\ 0 \end{bmatrix} + \mathbf{R}_3 \mathbf{R}_2 \mathbf{R}_1 \begin{bmatrix} 0 \\ 0 \\ \dot{\theta}_0 \end{bmatrix} \right] \right], \\ &= \begin{bmatrix} \cos \chi (\dot{\phi}_x - \dot{\theta}_0 \sin \phi_y) - \sin \chi (-\dot{\phi}_y \sin \phi_x + \dot{\theta}_0 \cos \phi_x \cos \phi_y) \\ \dot{\phi}_y \cos \phi_x + \dot{\theta}_0 \sin \phi_x \cos \phi_y \\ \sin \chi (\dot{\phi}_x - \dot{\theta}_0 \sin \phi_y) + \cos \chi (-\dot{\phi}_y \sin \phi_x + \dot{\theta}_0 \cos \phi_x \cos \phi_y) \end{bmatrix}. \end{aligned}$$

Hence the rotational energy can now be easily computed as

$$\begin{aligned} \frac{1}{2} \boldsymbol{\Omega}^T \mathbf{J} \boldsymbol{\Omega} &= \frac{1}{2} J_t \left((\cos \chi (\dot{\phi}_x - \Omega \sin \phi_y) - \sin \chi (-\dot{\phi}_y \sin \phi_x + \Omega \cos \phi_x \cos \phi_y))^2 \right. \\ &\quad \left. + (\dot{\phi}_y \cos \phi_x + \Omega \sin \phi_x \cos \phi_y)^2 \right) \\ &\quad + \frac{1}{2} J_p \left(\sin \chi (\dot{\phi}_x - \Omega \sin \phi_y) + \cos \chi (-\dot{\phi}_y \sin \phi_x + \Omega \cos \phi_x \cos \phi_y) \right)^2. \end{aligned} \quad (2.6)$$

Finally, substituting the equations (2.4-2.6) into equation (2.3) completes the derivation of the kinetic energy for the system.

Potential energy and damping

The potential energy V , arises from the elastic deflection of the support bearings at S_1 and S_2 , as shown in Figure 2.1. The coordinates of these supports are given in the rotor-fixed frame by $[0, 0, l_1]^T$ and $[0, 0, -l_2]^T$, and we assume that each bearing is linear and isotropic with stiffness k_1 , k_2 and damping c_1 , c_2 respectively. By transforming coordinates to the space frame, the deflection \mathbf{d}_{S_i} of each support may be written as

$$\begin{aligned}\mathbf{d}_{S_i} &= \mathbf{R}_1^T \left[\begin{bmatrix} x \\ y \\ 0 \end{bmatrix} + \mathbf{R}_2^T \mathbf{R}_3^T \begin{bmatrix} 0 \\ 0 \\ \tilde{l}_i \end{bmatrix} \right] - \begin{bmatrix} 0 \\ 0 \\ \tilde{l}_i \end{bmatrix}, \\ &= \begin{bmatrix} \cos \theta_0 (x + \cos \phi_x \sin \phi_y \tilde{l}_i) - \sin \theta_0 (y - \sin \phi_x \tilde{l}_i) \\ \sin \theta_0 (x + \cos \phi_x \sin \phi_y \tilde{l}_i) + \cos \theta_0 (y - \sin \phi_x \tilde{l}_i) \\ \cos \phi_x \cos \phi_y \tilde{l}_i - \tilde{l}_i \end{bmatrix},\end{aligned}$$

where

$$\tilde{l}_1 = l_1 \quad \text{and} \quad \tilde{l}_2 = -l_2.$$

Hence the potential energy can be computed as

$$\begin{aligned}V &= \frac{1}{2} \sum_{i=1}^2 k_i \mathbf{d}_{S_i}^2, \\ &= \frac{1}{2} k_1 \left((x + \cos \phi_x \sin \phi_y l_1)^2 + (y - \sin \phi_x l_1)^2 + (\cos \phi_x \cos \phi_y l_1 - l_1)^2 \right) \\ &\quad + \frac{1}{2} k_2 \left((x - \cos \phi_x \sin \phi_y l_2)^2 + (y + \sin \phi_x l_2)^2 + (-\cos \phi_x \cos \phi_y l_2 + l_2)^2 \right).\end{aligned}\quad (2.7)$$

It is usual to assume that the vibrational coordinates (ϕ_x, ϕ_y) together with the imbalance errors ε and χ are small and $\mathcal{O}(\delta)$, with δ a small quantity. If we are to neglect terms of $\mathcal{O}(\delta^2)$ in the equations of motion, then all terms of order $\mathcal{O}(\delta^3)$ which enter into Lagrange's equation will not contribute to the system, and can be ignored. A routine calculation now gives the more familiar expression

$$V = \frac{1}{2} k_{11} (x^2 + y^2) + k_{12} (x \phi_y - y \phi_x) + \frac{1}{2} k_{22} (\phi_y^2 + \phi_x^2) + \mathcal{O}(\delta^3),$$

where

$$k_{11} = k_1 + k_2, \quad k_{12} = k_1 l_1 - k_2 l_2, \quad k_{22} = k_1 l_1^2 + k_2 l_2^2. \quad (2.8)$$

Next we turn to the dissipative effects, which arise from the damping at the supports, together with the viscous drag on the balls c_b , as they pass through the fluid in the race. These terms are most easily calculated through the use of Rayleigh's dissipation function

$$F = \frac{1}{2} \sum_{i=1}^2 c_i \dot{\mathbf{d}}_{S_i}^2 + \frac{1}{2} \sum_{k=1}^4 c_b \dot{\alpha}_k^2,$$

which after some manipulation we may write as

$$\begin{aligned}
F = & \frac{1}{2}c_{11}((\dot{x} - \Omega y)^2 + (\dot{y} + \Omega x)^2) \\
& + c_{12}((\dot{x} - \Omega y)(\dot{\phi}_y + \Omega \phi_x) + (y + \Omega x)(-\dot{\phi}_x + \Omega \phi_y)) \\
& + \frac{1}{2}c_{22}\left(\left(\dot{\phi}_y + \Omega \phi_x\right)^2 + \left(-\dot{\phi}_x + \Omega \phi_y\right)^2\right) + \frac{1}{2}\sum_{k=1}^4 c_b \dot{\alpha}_k^2 + \mathcal{O}(\delta^3),
\end{aligned} \tag{2.9}$$

where

$$c_{11} = c_1 + c_2, \quad c_{12} = c_1 l_1 - c_2 l_2, \quad c_{22} = c_1 l_1^2 + c_2 l_2^2. \tag{2.10}$$

The fully geometric nonlinear equations of motion are generated by substituting (2.3), (2.7) and (2.9) into Lagrange's equations. Before displaying them here, we shall first continue with a non-dimensionalisation.

2.1.4 Non-dimensionalisation and the equations of motion

We now consider the following dimensionless state variables

$$\begin{aligned}
\bar{x} &= \frac{x}{R}, \quad \bar{y} = \frac{y}{R}, \quad \bar{\phi}_x = \phi_x, \quad \bar{\phi}_y = \phi_y, \\
\bar{\alpha}_k &= \alpha_k \quad \text{for } k = 1 \dots 4,
\end{aligned}$$

and the dimensionless time

$$\bar{t} = \Omega_{\text{cyl}} t.$$

Here Ω_{cyl} is the critical frequency that is associated with the cylindrical whirl, and it is given by $\Omega_{\text{cyl}} = \sqrt{\frac{k_{11}}{M}}$. Furthermore, we introduce the dimensionless parameters

$$\begin{aligned}
\bar{\Omega} &= \frac{\Omega}{\Omega_{\text{cyl}}}, \quad \bar{\varepsilon} = \frac{\varepsilon}{R}, \quad \bar{m} = \frac{m}{M}, \quad \bar{z} = \frac{z}{R}, \\
\bar{J}_t &= \frac{J_t}{MR^2}, \quad \bar{J}_p = \frac{J_p}{MR^2}, \quad \bar{\chi} = \chi, \quad \bar{c}_b = \frac{c_b}{m\Omega_{\text{cyl}} R^2}, \\
\bar{k}_{11} &= \frac{k_{11}}{M\Omega_{\text{cyl}}^2} \equiv 1, \quad \bar{k}_{12} = \frac{k_{12}}{M\Omega_{\text{cyl}}^2 R}, \quad \bar{k}_{22} = \frac{k_{22}}{M\Omega_{\text{cyl}}^2 R^2}, \\
\bar{c}_{11} &= \frac{c_{11}}{M\Omega_{\text{cyl}}}, \quad \bar{c}_{12} = \frac{c_{12}}{M\Omega_{\text{cyl}} R}, \quad \bar{c}_{22} = \frac{c_{22}}{M\Omega_{\text{cyl}} R^2}.
\end{aligned}$$

The equations of motion with respect to these non-dimensional quantities can be computed with the aid of the computer algebra system `Maple`, and are given as follows up to order $\mathcal{O}(\delta^2)$.

The overbars have been omitted for clarity and we start with the equations for the rotor motion, which are given by

$$\begin{aligned} & \begin{bmatrix} \mathbf{M} & \mathbf{0} \\ \mathbf{0} & \mathbf{M} \end{bmatrix} \ddot{\mathbf{x}} + \begin{bmatrix} \mathbf{C} & -\Omega(\mathbf{M}-\mathbf{G}) \\ \Omega(\mathbf{M}-\mathbf{G}) & \mathbf{C} \end{bmatrix} \dot{\mathbf{x}} + \begin{bmatrix} \mathbf{K}-\Omega^2(\mathbf{M}-\mathbf{G}) & -\Omega\mathbf{C} \\ \Omega\mathbf{C} & \mathbf{K}-\Omega^2(\mathbf{M}-\mathbf{G}) \end{bmatrix} \mathbf{x} \\ &= \Omega^2 \begin{bmatrix} \varepsilon \cos \beta \\ \chi(J_t - J_p) \\ \varepsilon \sin \beta \\ 0 \end{bmatrix} + m \sum_{k=1}^4 \begin{bmatrix} (\Omega + \dot{\alpha}_k)^2 & 0 & \ddot{\alpha}_k & 0 \\ 0 & (\Omega + \dot{\alpha}_k)^2 & 0 & \ddot{\alpha}_k \\ -\ddot{\alpha}_k & 0 & (\Omega + \dot{\alpha}_k)^2 & 0 \\ 0 & -\ddot{\alpha}_k & 0 & (\Omega + \dot{\alpha}_k)^2 \end{bmatrix} \begin{bmatrix} \cos \alpha_k \\ z_k \cos \alpha_k \\ \sin \alpha_k \\ z_k \sin \alpha_k \end{bmatrix} + \begin{bmatrix} 0 \\ n_{\phi_y} \\ 0 \\ n_{-\phi_x} \end{bmatrix}. \end{aligned} \quad (2.11)$$

Coupled with (2.11) are the equations of motion for the balancing balls which are

$$\begin{aligned} \ddot{\alpha}_k + c_b \dot{\alpha}_k = & \left((\ddot{x} + z_k \ddot{\phi}_y) - 2\Omega (\dot{y} - z_k \dot{\phi}_x) - \Omega^2 (x + z_k \phi_y) \right) \sin \alpha_k \\ & - \left((\ddot{y} - z_k \ddot{\phi}_x) + 2\Omega (\dot{x} + z_k \dot{\phi}_y) - \Omega^2 (y - z_k \phi_x) \right) \cos \alpha_k, \text{ for } k = 1 \dots 4. \end{aligned} \quad (2.12)$$

Here

$$\mathbf{M} = \begin{bmatrix} 1 + 4m & \sum_k m z_k \\ \sum_k m z_k & J_t + \sum_k m z_k^2 \end{bmatrix}, \quad \mathbf{G} = \begin{bmatrix} 0 & 0 \\ 0 & J_p \end{bmatrix}, \quad \mathbf{C} = \begin{bmatrix} c_{11} & c_{12} \\ c_{12} & c_{22} \end{bmatrix}, \quad \mathbf{K} = \begin{bmatrix} k_{11} & k_{12} \\ k_{12} & k_{22} \end{bmatrix},$$

are the mass, gyroscopic, damping and stiffness matrices respectively and $\mathbf{x} = [x, \phi_y, y, -\phi_x]^T$ is the vector of the rotor degrees of freedom. We have used $-\phi_x$ instead of ϕ_x in the definition of \mathbf{x} so that (2.11) assumes a more regular pattern. Finally the n_{ϕ_y} and $n_{-\phi_x}$ terms are given by

$$\begin{aligned} n_{\phi_y} = & m \sum_{k=1}^4 \left[(\ddot{x} - 2\Omega \dot{y} - \Omega^2 x) (\phi_y \cos \alpha_k - \phi_x \sin \alpha_k) - \cos^2 \alpha_k (\ddot{\phi}_y - 2\dot{\alpha}_k \dot{\phi}_x + (\Omega^2 + 2\Omega \dot{\alpha}_k) \phi_y) \right. \\ & \left. + \sin \alpha_k \cos \alpha_k (\ddot{\phi}_x + 2\dot{\alpha}_k \phi_y + (\Omega^2 + 2\Omega \dot{\alpha}_k) \phi_x) + \ddot{\alpha}_k \phi_x \right], \\ n_{-\phi_x} = & m \sum_{k=1}^4 \left[(\ddot{x} - 2\Omega \dot{y} - \Omega^2 x) \phi_y \sin \alpha_k + \sin^2 \alpha_k (\ddot{\phi}_x + 2\dot{\alpha}_k \dot{\phi}_y + (\Omega^2 + 2\Omega \dot{\alpha}_k) \phi_x) \right. \\ & \left. - (\ddot{y} + 2\Omega \dot{x} - \Omega^2 y) \phi_x \sin \alpha_k - \sin \alpha_k \cos \alpha_k (\ddot{\phi}_y - 2\dot{\alpha}_k \dot{\phi}_x + (\Omega^2 + 2\Omega \dot{\alpha}_k) \phi_y) \right]. \end{aligned} \quad (2.13)$$

We note that by taking $m = 0$ in (2.11), we recover the equations of motion for a four-degree-of-freedom rotor in the rotating frame [24, §3]. Similarly, by setting the tilt angles $\phi_x = \phi_y \equiv 0$, the system reduces to the equations of motion for the planar automatic balancer [28].

It is also worth remarking that there are certain asymmetries in the n_{ϕ_y} and $n_{-\phi_x}$ terms corresponding to the $\mathcal{O}(\delta)$ moments of the balancing balls. These arise because of the inherently

asymmetrical nature of an Euler angle formulation. With reference to Figure 2.2, we recall that ϕ_x is a rotation about the body ξ axis while ϕ_y is taken, not about the body η axis, but about an intermediate y' axis. With the standard rotordynamic assumptions of small tilt angles and small eccentricities these asymmetries do not survive the linearisation process. Here however, where the lever arm of the race cannot be neglected, extra terms including these asymmetries are present [25].

2.2 Steady state bifurcation analysis

In this section we consider the existence and stability of steady state solutions of the system given by equations (2.11) and (2.12). In order to simplify the bifurcation analysis, we shall restrict attention to a symmetric subsystem which displays all the primary features of the autobalancing process. A situation that is common in practice occurs when the rotor's centre of mass is located at the midspan and both supports are identical, so that

$$k_1 = k_2 = k, \quad c_1 = c_2 = c, \quad l_1 = l_2 = l, \quad \text{which leads to} \quad k_{12} = c_{12} = 0.$$

With this set-up, the lateral and inclination motions of the rotor remain coupled, but only through the motion of the balancing balls. In addition, we assume that $z_{1,2} = -z_{3,4} = z$, so that the autobalancing planes are equidistant from the midspan.

The rest of this section is organised as follows: in Section 2.2.1 we obtain the steady state solutions, noting various conditions governing their existence, and from Section 2.2.2 onwards we use the continuation package AUTO [16] to compute bifurcation diagrams showing the boundaries of stability in various parameter planes.

2.2.1 Explicit steady state solutions

Steady state solutions are obtained by setting all time derivatives in the equations of motion (2.11-2.12) to zero. Moreover, if we also set the vibrational coordinates $(x, y, \phi_x, \phi_y) = \mathbf{0}$, we arrive at the following conditions for a balanced steady state

$$\begin{aligned} \cos \alpha_1 + \cos \alpha_2 + \cos \alpha_3 + \cos \alpha_4 &= s_x, \\ \sin \alpha_1 + \sin \alpha_2 + \sin \alpha_3 + \sin \alpha_4 &= s_y, \\ \cos \alpha_1 + \cos \alpha_2 - \cos \alpha_3 - \cos \alpha_4 &= c_x, \\ \sin \alpha_1 + \sin \alpha_2 - \sin \alpha_3 - \sin \alpha_4 &= c_y, \end{aligned} \tag{2.14}$$

where

$$s_x = \frac{-\varepsilon \cos \beta}{m}, \quad s_y = \frac{-\varepsilon \sin \beta}{m}, \quad c_x = \frac{-\chi (J_t - J_p)}{mz}, \quad c_y = 0.$$

These are precisely the conditions for equilibrium between the centrifugal forces and moments acting on the rotor due to the imbalance and balancing balls [58]. By rewriting the above equation with respect to the average and differential angular displacements within each race, we find that

$$\begin{aligned}\cos \hat{\alpha}_{12} \cos \bar{\alpha}_{12} &= \frac{s_x + c_x}{4}, \\ \cos \hat{\alpha}_{12} \sin \bar{\alpha}_{12} &= \frac{s_y + c_y}{4}, \\ \cos \hat{\alpha}_{34} \cos \bar{\alpha}_{34} &= \frac{s_x - c_x}{4}, \\ \cos \hat{\alpha}_{34} \sin \bar{\alpha}_{34} &= \frac{s_y - c_y}{4},\end{aligned}\tag{2.15}$$

where

$$\bar{\alpha}_{12} = \frac{\alpha_1 + \alpha_2}{2}, \quad \hat{\alpha}_{12} = \frac{\alpha_1 - \alpha_2}{2}, \quad \bar{\alpha}_{34} = \frac{\alpha_3 + \alpha_4}{2}, \quad \hat{\alpha}_{34} = \frac{\alpha_3 - \alpha_4}{2}.\tag{2.16}$$

Because the balls are assumed to be identical, we may without loss of generality take $0 \leq \hat{\alpha}_{12}, \hat{\alpha}_{34} \leq \frac{\pi}{2}$, and equation (2.15) can now be solved to give the following physically unique balanced state

$$\begin{aligned}\bar{\alpha}_{12} &= \arctan\left(\frac{s_y + c_y}{s_x + c_x}\right) + \begin{cases} 0 & \text{if } s_x + c_x \geq 0, \\ \pi & \text{if } s_x + c_x < 0. \end{cases}, \\ \hat{\alpha}_{12} &= \arccos\left(\frac{1}{4}\sqrt{(s_x + c_x)^2 + (s_y + c_y)^2}\right), \\ \bar{\alpha}_{34} &= \arctan\left(\frac{s_y - c_y}{s_x - c_x}\right) + \begin{cases} 0 & \text{if } s_x - c_x \geq 0, \\ \pi & \text{if } s_x - c_x < 0. \end{cases}, \\ \hat{\alpha}_{34} &= \arccos\left(\frac{1}{4}\sqrt{(s_x - c_x)^2 + (s_y - c_y)^2}\right).\end{aligned}\tag{2.17}$$

This solution exists provided that the arguments for both the arccoses have modulus less than one, which ensures that the balls have enough mass to counteract the imbalance of the system. In what follows we refer to (2.17) as the balanced state **B**.

The steady state configurations for the special case of a rotor with a static imbalance are illustrated in Figure 2.4. The balanced state **B** is shown on the left, but there are also various other steady state solutions for which the rotor remains out of balance. In these cases we consider the equation for the balls (2.12), which upon setting time derivatives to zero, yield

$$(x + z_k \phi_y) \sin \alpha_k = (y - z_k \phi_x) \cos \alpha_k, \quad k = 1 \dots 4,\tag{2.18}$$

where $x + z_k \phi_y$ and $y - z_k \phi_x$, are recognised as the x and y deflections of the race centres. If

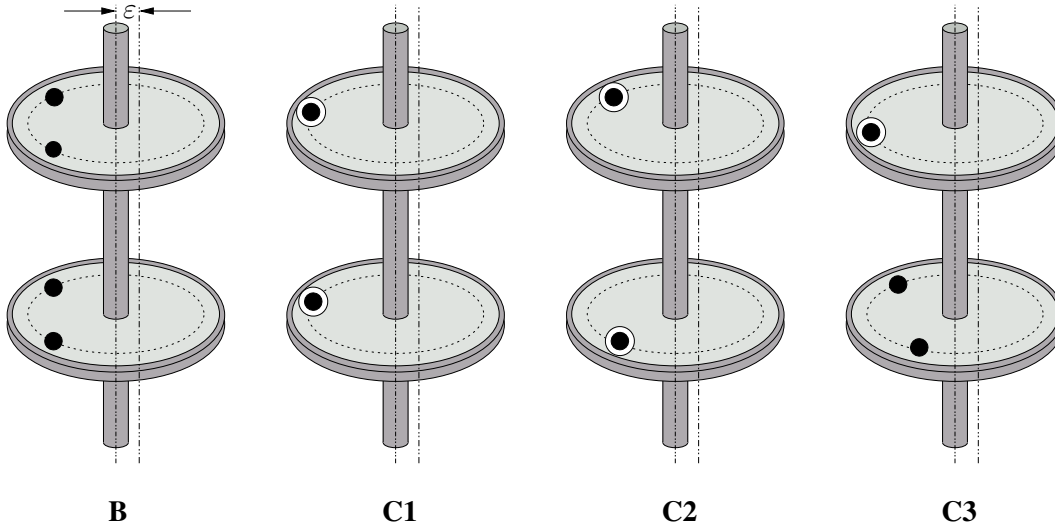


Figure 2.4. Schematic diagram of the steady states for the case of a static imbalance. White surrounds denote that both balls in the race are coincident.

for both of the races $(x + z_k\phi_y, y - z_k\phi_x) \neq \mathbf{0}$, then we may rewrite (2.18) as

$$\tan \alpha_k = \left(\frac{y - z_k\phi_x}{x + z_k\phi_y} \right), \quad k = 1 \dots 4,$$

with solutions

$$\alpha_1 = \alpha_2 + p\pi, \quad \alpha_3 = \alpha_4 + q\pi, \quad p, q \in \mathbb{Z}.$$

Therefore the balls in each race are either *coincident*, or *in-line* with the race centre and opposite each other. For example, in state **C1** all the balls have the same angle and this configuration results in the excitation of a cylindrical whirl. For state **C2**, the balls in each race are again coincident but there are now two distinct angular displacements. This arrangement generates a couple imbalance and leads to a conical type whirl. The inline states will not be discussed further because they are found to be always unstable and are never involved in bifurcations with the balanced state.

Next we consider the state **C3**, in which $(x + z_k\phi_y, y - z_k\phi_x) = \mathbf{0}$ is satisfied by one of the two races, so that its centre stays fixed at the undeflected position. The balls within this fixed race are now not constrained by equation (2.18), although the balls in the opposing race are again either coincident or inline. As an example, the arrangement for **C3** depicted in Figure 2.4 shows coincident balls in the top race while the bottom race balls are split. The corresponding state, where the roles of the races are swapped, is physically equivalent, because the symmetry between the two races is preserved by a static imbalance. However, this will not be the case for a general imbalance, as we shall discuss in Section 2.2.4. Finally, we note that if $(x + z_k\phi_y, y - z_k\phi_x) = \mathbf{0}$ for both of the races, then we are again led to the balanced state **B**, which has been covered previously.

For the remainder of this section we shall conduct numerical continuation studies on different steady state solutions using the software package **AUTO**. We consider a rotor with the following non-dimensional inertial and stiffness parameters

$$\begin{aligned} J_t &= 3.25, & J_p &= 0.5, & l &= 3, \\ k_{11} &\equiv 1, & k_{12} &= 0, & k_{22} &= 9. \end{aligned} \quad (2.19)$$

These values are based on a solid cylindrically shaped rotor with a height of six times its radius. A rotating machine on compliant bearings with this geometry would typically undergo a two-plane balancing procedure before going into service. The approximate natural frequencies for the cylindrical and conical modes occur respectively at

$$\Omega_{\text{cyl}} = \sqrt{\frac{k_{11}}{M}} \equiv 1, \quad \text{and} \quad \Omega_{\text{con}} = \sqrt{\frac{k_{22}}{J_t - J_p}} \simeq 1.81, \quad (2.20)$$

and we shall now investigate the results for both the static and dynamic imbalance cases.

2.2.2 Static imbalance

As mentioned above, a static imbalance occurs when the principal axis is displaced, but parallel to, the rotation axis so that there is an eccentricity $\varepsilon \neq 0$, but no misalignment $\chi = 0$. For this special case, we are able to recover all the bifurcations and steady state solutions that have been found previously in the studies of a planar automatic balancer [14, 28]. However, because our model includes the extra inclinational degrees of freedom, the rotor is now able to destabilise via out of plane motions, and so the steady states will necessarily have smaller regions of stability.

In Figure 2.5 we present results for the following non-dimensional parameter values

$$\begin{aligned} \varepsilon &= 0.01, & \chi &= 0, & (\beta &= 0), \\ z &= 2, & c_b &= 0.01, & \text{and} & c = 0.01, \\ && \text{so that} \\ c_{11} &= 0.02, & c_{12} &= 0, & c_{22} &= 0.18. \end{aligned} \quad (2.21)$$

For this value of the eccentricity, the balanced state **B** exists provided that

$$m \geq m_c := \frac{\varepsilon}{4} = 0.0025, \quad (2.22)$$

where m_c is the critical value of the non-dimensional ball mass. We also note that the balancing planes are appropriately spaced, and that the race and supports have low damping values, which match those in [14, 28].

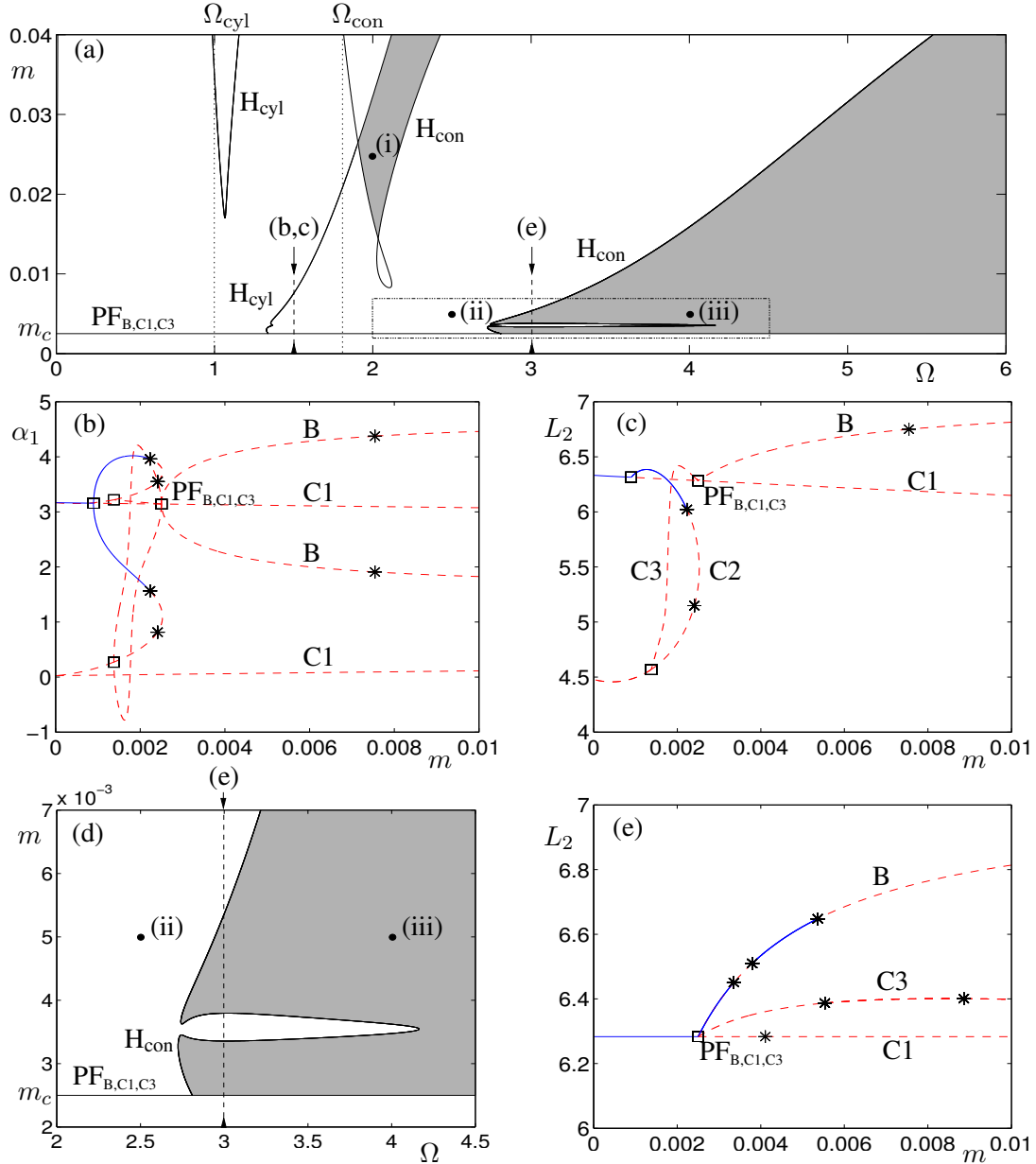


Figure 2.5. Bifurcation diagrams for the case of a static imbalance. We take $\varepsilon = c = c_b = 0.01$, with the other parameters given by (2.19–2.21). Panel (a) is a two-parameter bifurcation diagram in the (Ω, m) -plane, where the shaded regions correspond to a stable balanced state **B**. This state is born at the (degenerate) pitchfork $PF_{B,C1,C3}$, which occurs on the line $m = m_c$. Hopf bifurcation curves H of the balanced state are also shown, here the subscripts denote whether the cylindrical or conical mode is involved. Numerical simulations at the points indicated by a (•) are presented in Figure 2.11, and panel (d) shows the indicated detail around $\Omega = 3$. Panel (b) shows a one-parameter diagram in m with solution measure α_1 for $\Omega = 1.5$. Solid blue lines and red dashed lines represent stable and unstable steady states respectively, (\square) and (*) denote pitchfork and Hopf bifurcations respectively and the labels correspond to the solutions depicted in Figure 2.4. Panel (c) is the same as (b) except that the measure is changed to the Euclidean norm L_2 of the solution vector. Panel (e) shows a similar one-parameter bifurcation diagram for $\Omega = 3$.

Figure 2.5(a) shows the results of a two-parameter bifurcation analysis upon variation of the dimensionless parameters Ω and m , whilst we keep the other parameters fixed. The shaded regions correspond to the existence of a stable balanced state **B**, although as we shall discuss in Section 2.3, other less desirable stable states may coexist in these regions. For masses of the balls which satisfy $m \geq m_c$ the balanced state **B** always exists, but it is not necessarily stable. The curves marked H_{cyl} and H_{con} are Hopf bifurcations of **B**, at which oscillations are induced by the cylindrical and conical modes respectively. In a planar analysis only the H_{cyl} curves are present, and as such, they are always accompanied by a change in stability. Here with the inclusion of the inclinational degrees of freedom, the stability of **B** is predominately determined by the H_{con} curves, at which the conical type oscillations are either created or destroyed.

For large values of Ω , the balanced state **B** stabilises in a Hopf bifurcation H_{con} and there is also a secondary region of stability, for sufficiently large values of m , at rotation speeds just above the natural frequency Ω_{con} . We also draw attention to the similarities between the shape of the two Hopf curves H_{cyl} and H_{con} , suggesting that there is in some sense, a duality between the lateral and inclinational dynamics of the automatic balancer.

The one-parameter bifurcation diagrams of Figures 2.5(b) and (c) show the result of increasing m through m_c for $\Omega = 1.5$, which is a value of the rotation speed that lies in between the critical frequencies of the rotor. The angular displacement α_1 is used as the solution measure in Figure 2.5(b), and we see that an unstable balanced state **B** is born at $m = m_c$ in a pitchfork bifurcation involving the unstable coincident state **C1**. Note that the two copies of the balanced state **B** come from interchanging the ball positions, for example $\alpha_1 \leftrightarrow \alpha_2$. In Figure 2.5(c) we plot the same bifurcation diagram as shown in panel (b) but instead we use the Euclidean norm

$$L_2 = \sqrt{\sum_k q_k^2} \quad \text{where} \quad \mathbf{q} = (x, y, \phi_x, \phi_y, \alpha_1, \alpha_2, \alpha_3, \alpha_4).$$

Here only one copy of each physically unique state is generated, and we can see that the balanced state **B** is in fact produced at a degenerate pitchfork bifurcation involving the states **C1** and **C3**.

Next we consider the situation for the supercritical regime where $\Omega > \Omega_{\text{con}}$. Figure 2.5(d) is an enlargement of our region of interest and panel (e) shows a one parameter scan as we increase m through m_c , for a fixed rotation speed of $\Omega = 3$. Again we find that the balanced state **B** is born at a degenerate pitchfork bifurcation involving states **C1** and **C3**, but in contrast with the situation for subcritical rotation speeds, the coincident state **C1** and the bifurcating balanced state **B** are now both stable. Note also, that the balanced state changes stability through a series of three further Hopf bifurcations, which is in agreement with the vertical slice taken through panel (d) at $\Omega = 3$.

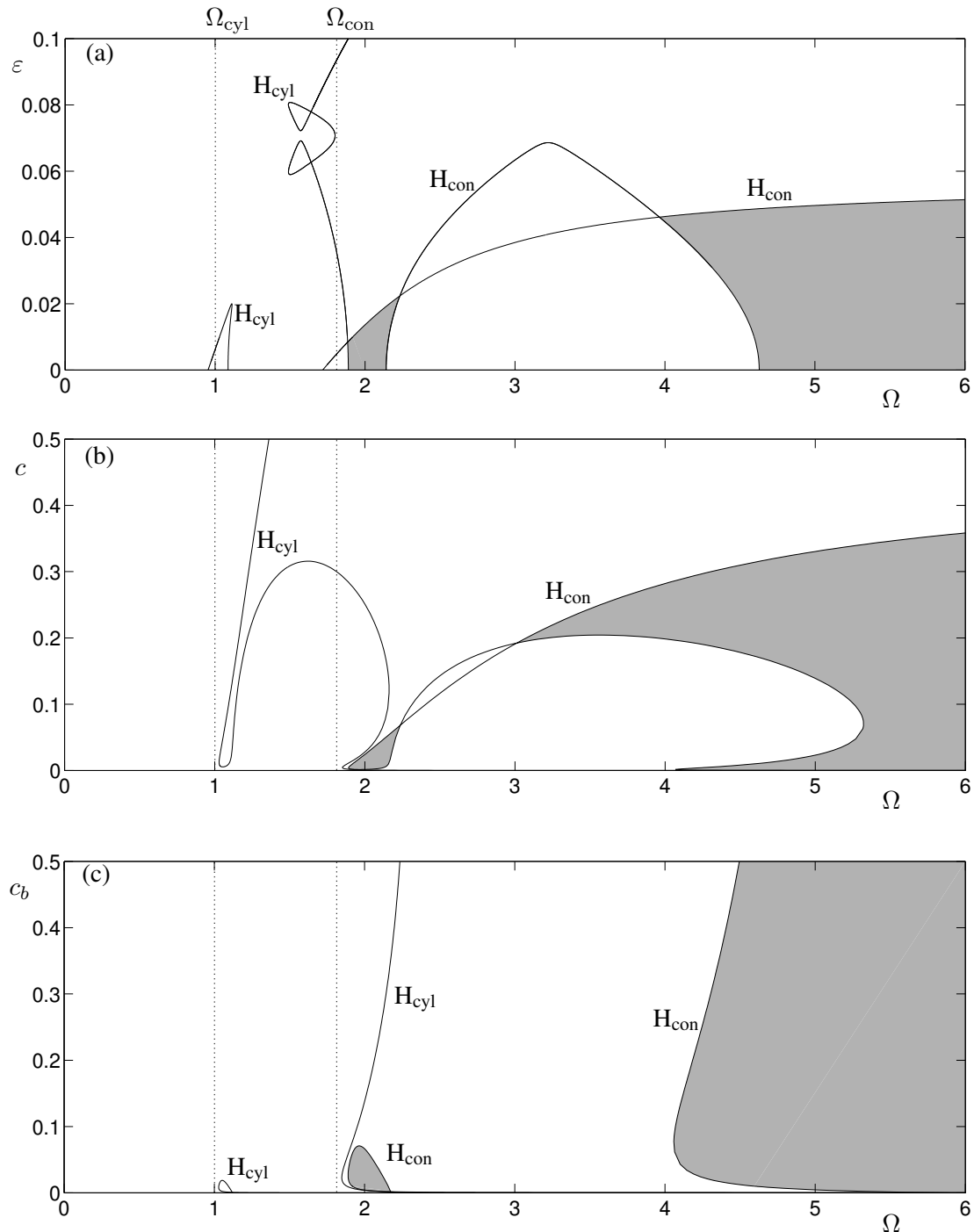


Figure 2.6. Two-parameter bifurcation diagrams, upon variation of the parameters: (a) ε against Ω , (b) c against Ω , and (c) c_b against Ω . The shaded regions correspond to a stable balanced state **B**, and Hopf bifurcations H are shown with subscripts indicating the mode of oscillation. Parameters when fixed are $m = 0.025$, $\varepsilon = c = c_b = 0.01$, with the other values as specified in the text.

Now let us consider some stability diagrams similar to Figure 2.5(a), in which we vary other dimensionless parameters. We take $m = 0.025$ so that condition (2.22) needed for balance is satisfied, and the values for the other parameters when fixed are again given by (2.19) and (2.21).

In Figure 2.6 we display some two-parameter stability charts upon variation of the eccentricity ε , the support damping c , and the race damping c_b , as the rotation speed Ω is increased. Here, we are again able to recover the H_{cyl} curves which are present in the planar analyses, but as before the H_{con} bifurcations have more influence on the stability of the balanced state. We also highlight some of the same features which were present in Figure 2.5, namely: the stabilisation of the balanced state through a H_{con} Hopf bifurcation for high enough rotation speeds, the smaller secondary stable region at rotation speeds just above Ω_{con} , and most notably in panel (c) the similarity between the shapes of the H_{cyl} and H_{con} curves.

Figure 2.7 shows the eccentricity ε , plotted against Ω , whilst we also vary the ball mass so that $m = 4m_c = \varepsilon$. Thus, for any given value of the eccentricity, the balls have a mass which is four times the minimum amount that is required to balance the system. A logarithmic scale is used for the vertical axis so that a wide range of eccentricities can be considered. Here, the main area of interest occurs for small eccentricities and supercritical rotation speeds where there is a large connected stable region. We also note that the H_{con} curve, which bounds this region, asymptotes towards $\Omega = \Omega_{\text{con}}$ as $\varepsilon \rightarrow 0$ so that there is no stable region in the subcritical regime.

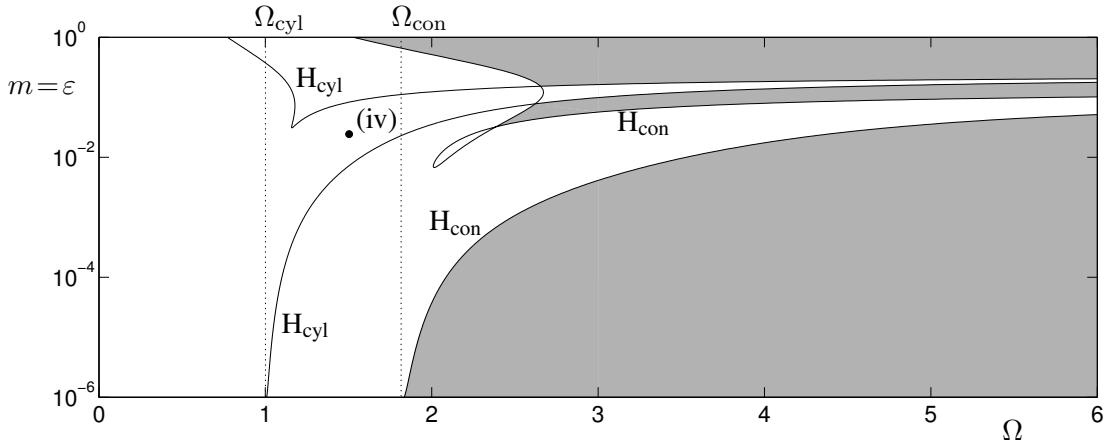


Figure 2.7. Diagram showing stable regions of the balanced state **B** upon variation of the parameters ε against Ω , whilst m is also varied so that $m = \varepsilon$. The vertical scale is logarithmic and $c = c_b = 0.01$.

2.2.3 Couple imbalance

Finally, before moving on to a general dynamic imbalance, we shall briefly discuss the case of a couple imbalance, for which there is a misalignment $\chi \neq 0$ but no eccentricity $\varepsilon = 0$. The steady states for this case are illustrated schematically in Figure 2.8. The only difference between the static imbalance steady states of Figure 2.4 is that here the bottom race has been rotated through an angle of π radians. Again, the symmetry between the two races is preserved by this type of imbalance, and the balanced state **B** is always born in a degenerate pitchfork bifurcation involving the coincident states **C1** and **C3**. Moreover, if the misalignment parameter χ is appropriately chosen so that we again have $m_c = 0.0025$, the results shown in Figure 2.5(a) for a static imbalance can be recovered. Thus, there is an equivalence between the properties of the automatic balancer for a pure eccentricity and for a pure misalignment and we shall not provide any explicit bifurcation diagrams for the couple imbalance case.

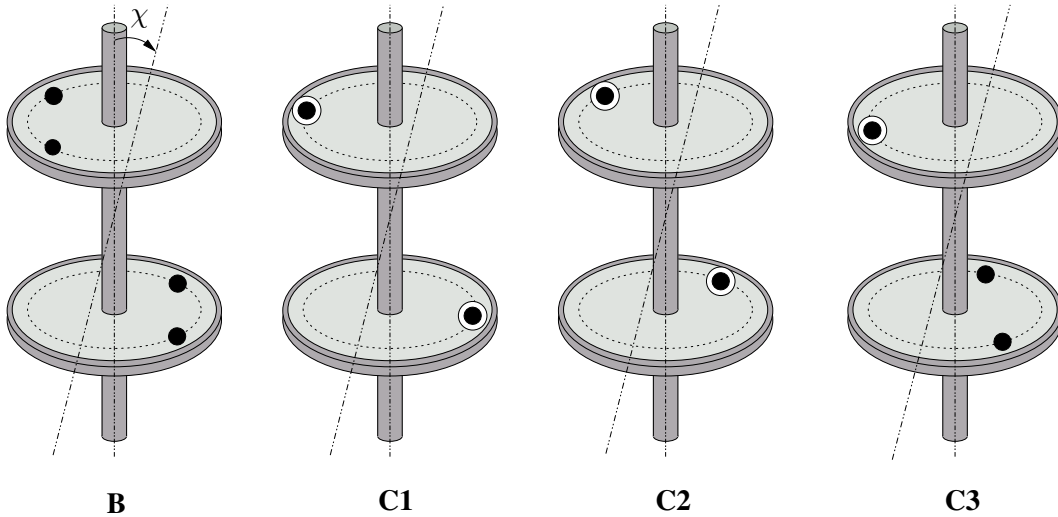


Figure 2.8. Schematic diagram of the steady states for the case of a couple imbalance. White surrounds again indicate that both balls in the race are coincident.

2.2.4 General dynamic imbalance

A dynamic imbalance arises when there is both an eccentricity $\varepsilon \neq 0$, and a misalignment $\chi \neq 0$. A phase angle β must also be included to describe the difference between the directions of the two imbalances.

The parameter set which was given in (2.19) and (2.21) is used again, except that we change the imbalance characteristics to

$$\varepsilon = 0.005, \quad \chi = 0.005, \quad \beta = 1.$$

The critical mass for the balls m_c , is now given by

$$m_c = \max\{m_t, m_b\} := \max\left\{\frac{1}{4}\sqrt{\left(\varepsilon \cos \beta \pm \frac{\chi(J_t - J_p)}{z}\right)^2 + (\varepsilon \sin \beta)^2}\right\} \simeq 0.00261, \quad (2.23)$$

where m_t and m_b are the critical masses at the top and bottom races respectively. The calculated value is similar to that of the static imbalance case of Section 2.2.2.

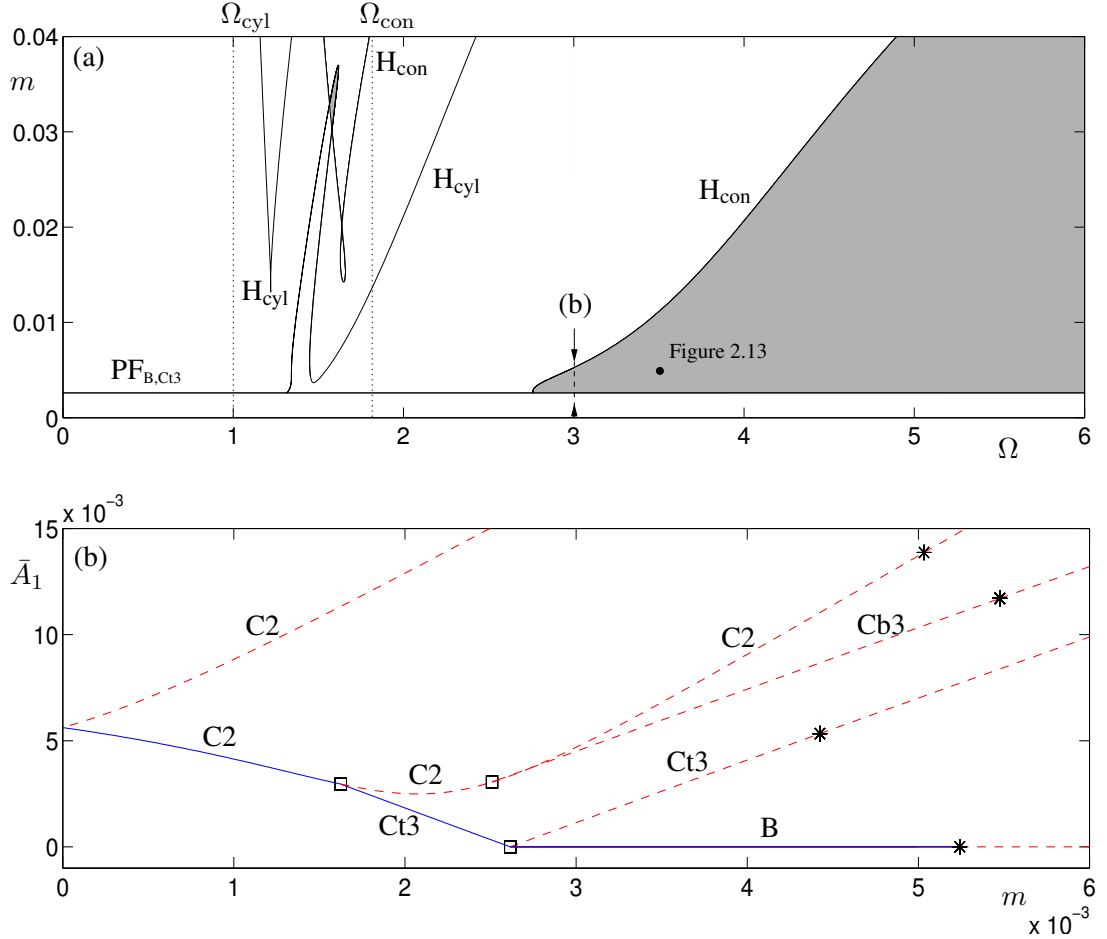


Figure 2.9. Panel (a) is a bifurcation diagram in the (Ω, m) -plane showing curves of the pitchfork PF and Hopf bifurcations H which involve the balanced state \mathbf{B} . Parameters when fixed are, $\varepsilon = \chi = 0.005$, $\beta = 1$, and $c = c_b = 0.01$ with the other values specified in the text. The shaded region corresponds to a stable balanced state, and the subscripts for the Hopf bifurcations denote which mode is involved. Numerical simulations at the point highlighted by a (\bullet) are presented in Figure 2.13. A one-parameter diagram in m for $\Omega = 3$ is shown in (b), with norm \bar{A}_1 given by (2.24).

In Figure 2.9 (a) we provide a two-parameter bifurcation diagram upon the variation of the ball mass m and the rotation speed Ω . Qualitatively the graph is similar to the static case

of Figure 2.5(a), in that the balanced state also stabilises in a Hopf bifurcation H_{con} for high enough rotation speeds in the supercritical regime. However the secondary stable region has now almost disappeared, and we see a sharp upward spike in the lower H_{cyl} curve which is indicative of mixing between the cylindrical and conical modes. In panel (b) we scan vertically through Figure 2.9(a) holding the rotation speed fixed at $\Omega = 3$, while increasing the ball mass m through m_c . In this diagram we use the norm \bar{A}_1 defined by

$$\bar{A}_1 = \frac{1}{2} \left(\sqrt{(x + \phi_y)^2 + (y - \phi_x)^2} + \sqrt{(x - \phi_y)^2 + (y + \phi_x)^2} \right). \quad (2.24)$$

Physically this measure corresponds to the average vibration level at points on the shaft that are a unit length from the rotor centre. We see that the degenerate pitchfork bifurcation that was present for the static imbalance case has been split into three separate non-degenerate pitchforks. For a generic dynamic imbalance this unfolding occurs because the symmetry between the two races has been broken. As a consequence, the unbalanced steady state **C3** separates into two physically different cases. The configuration with coincident balls in the top race is called **Ct3**, whereas the corresponding state with the bottom race balls coincident is **Cb3**. We find that the symmetry and resulting degenerate bifurcation is only preserved when there is a pure static or couple imbalance or if the phase is such that $\cos \beta = 0$. In all these cases there is no component of the eccentricity which lies in the direction of the misalignment. Thus from (2.17) we can see that $\hat{\alpha}_{12} \equiv \hat{\alpha}_{34}$ and so the balanced state **B** is born from a state where the balls in both races are coincident.

Finally, in Figure 2.10 we provide a two-parameter bifurcation analysis as we vary: (a) the support damping c versus Ω , and (b) the race damping c_b versus Ω . Again we choose $m = 0.025$ so that condition (2.23) for the existence of the balanced state is satisfied. By comparison with Figure 2.6 we note that in both cases the secondary stable regions have been lost. Also the stable region for high rotation speeds and high support damping c is dramatically reduced.

2.3 Numerical simulations

We build on the bifurcation analysis of the previous section by presenting some results which illustrate the important dynamics of the ABB. Here we use the Matlab routine `ode45` to perform a direct numerical integration of the equations of motion (2.11) and (2.12) that were derived in Section 2.1. As a check, we note that our simulations agree with those of [14, 28] for appropriate choices of the parameters and initial conditions.

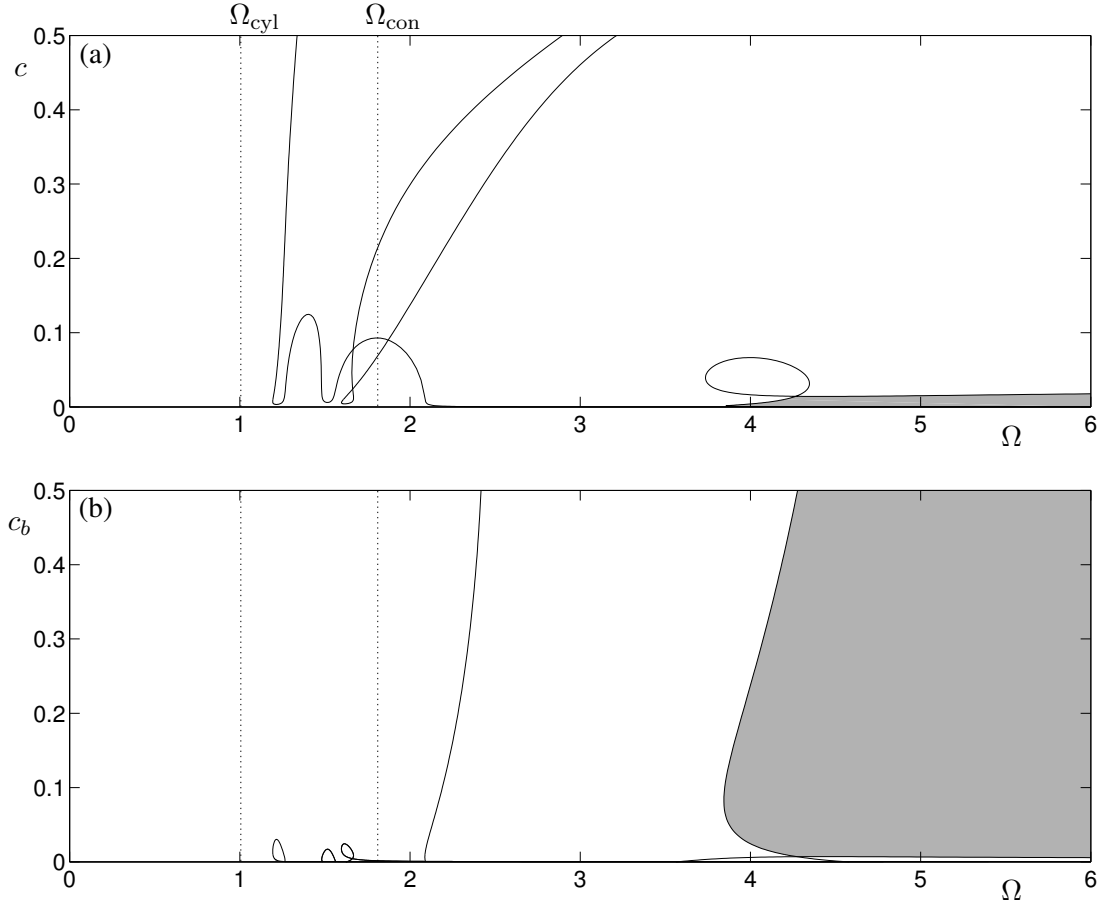


Figure 2.10. Two-parameter bifurcation diagrams, upon variation of the parameters: (a) c versus Ω , and (b) c_b versus Ω . The shaded regions correspond to a stable balanced state **B**. Parameters when fixed are $m = 0.025$, $\varepsilon = \chi = 0.005$, $\beta = 1$, and $c = c_b = 0.01$ with the other values specified in the text.

2.3.1 The effect of varying Ω , ε and m

Figure 2.11 shows the effect of varying the system parameters for the static imbalance case that was discussed in Section 2.2.2. The positions in parameter space of these runs are highlighted in Figures 2.5 and 2.7. We plot the vibration measure \bar{A}_1 against the dimensionless time t , here the black and grey curves represent the motion of the rotor with and without the ABB respectively. The initial conditions for all four plots are the same and are given by

$$\begin{aligned} \alpha_1 = -\alpha_2 = \alpha_3 = -\alpha_4 = \pi/2, \text{ and} \\ (x, y, \phi_x, \phi_y) = (\dot{x}, \dot{y}, \dot{\phi}_x, \dot{\phi}_y) = (\dot{\alpha}_1, \dot{\alpha}_2, \dot{\alpha}_3, \dot{\alpha}_4) = \mathbf{0}. \end{aligned} \quad (2.25)$$

Therefore the rotor starts in the undeflected position and the balls are initially stationary (with respect to the rotating frame) and are placed on opposite sides to each other so that they do not

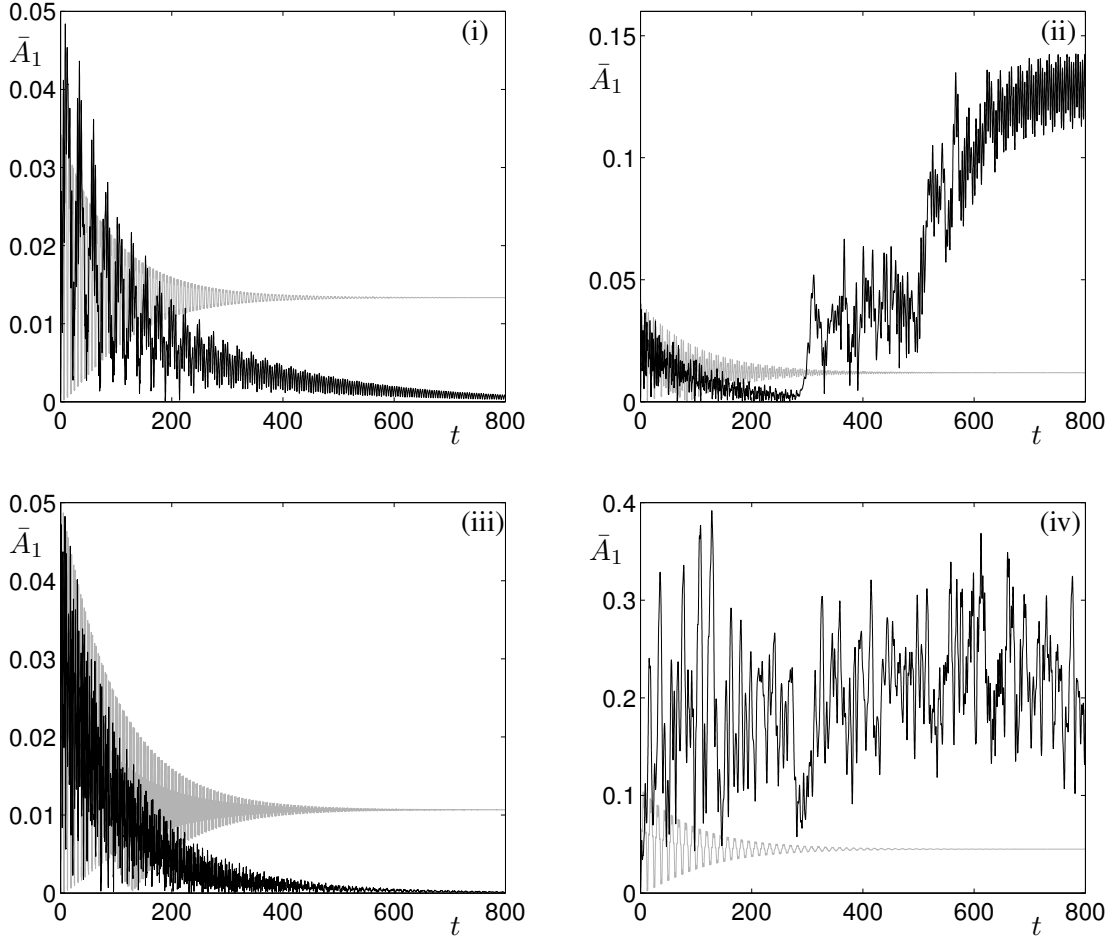


Figure 2.11. Numerical simulations showing vibration levels for the static imbalance case with low damping $c = c_b = 0.01$. The black responses are for the rotor with the ABB, and the grey responses represent the corresponding motion of the plain rotor without the balls. Initial conditions are fixed so that the rotor begins in the undeflected position and the balls in each race start on opposite sides with $(\alpha_1, -\alpha_2) = (\alpha_3, -\alpha_4) = \pi/2$. Values of Ω , ε and m are fixed at (i) $(\Omega, \varepsilon, m) = (2.0, 0.01, 0.025)$, (ii) $(2.5, 0.01, 0.005)$, (iii) $(4.0, 0.01, 0.005)$, and (iv) $(1.5, 0.025, 0.025)$. These points are specified in parameter space by a (\bullet) in Figures 2.5 and 2.7.

add to the imbalance of the rotor.

Panel (i) shows the simulation for $(\Omega, \varepsilon, m) = (2, 0.01, 0.025)$, which with reference to Figure 2.5, lies in the secondary region of stable balanced operation at a rotation speed just above the natural frequency Ω_{con} . We note that although the ABB eventually achieves balance, the transients produce slightly higher levels of initial vibrations. Also, if we perturb the initial conditions so that the shaft is slightly tilted, we find that the rotor can easily destabilise into a periodic type motion with significantly worse levels of vibration (not shown but qualitatively

similar to that of (ii)). This effect may be understood by considering the results of Figure 2.9, where we commented on the disappearance of the secondary stable region upon the introduction of a misalignment. The initial tilt of the rotor leads to a motion of the balls that produces a small couple imbalance, which in turn destabilises the operation of the ABB.

Figure 2.11 (ii) shows the time profile for $(\Omega, \varepsilon, m) = (2.5, 0.01, 0.005)$. This point lies outside the region of stability for the balanced state **B**, however the transient response dies down to a very low vibration level before eventually destabilising into periodic motion. This type of behaviour is typical of the dynamics near a saddle type fixed point when there are symmetrical initial conditions.

In panel (iii) our parameters are $(\Omega, \varepsilon, m) = (4, 0.01, 0.005)$, which lies in the larger primary region of stable balanced operation. For this case, balance is achieved after $t \approx 400$ and the transient period for both curves are approximately the same. Moreover the dynamics here are more robust than in (i) to perturbations in the initial tilt of the rotor. Again, with particular reference to Figures 2.5(a) and 2.9(a), we observe that the larger region of stability is not greatly influenced by the inclusion of a couple imbalance. Thus initial motions of the balls, which cause small inclinational motions, tend not to destabilise the device.

Finally, in panel (iv) we illustrate the behaviour for $(\Omega, \varepsilon, m) = (1.5, 0.025, 0.025)$, which as shown in Figure 2.7, lies well outside any region of balanced operation. This is a very undesirable state as the rotor now appears to undergo chaotic motion and reaches levels of vibration which are far higher than that for the rotor without an ABB mechanism.

2.3.2 The effect of race damping

Next the influence of race damping is considered. We take the dynamic imbalance set-up of Section 2.2.4 in which $(\varepsilon, \chi, \beta) = (0.005, 0.005, 1.0)$. In particular we select $(\Omega, m) = (3.5, 0.005)$, which as indicated in Figure 2.9, lies in the stable balanced region for $c_b = 0.01$.

The top graphs in Figure 2.12 display the vibration levels \bar{A}_1 for the rotor with and without the ABB mechanism. The corresponding angular displacements of the balancing balls α_1, α_2 (black curves) and α_3, α_4 (blue curves) are shown underneath. In all three cases the initial conditions are given by (2.25), thus the balls do not add to the starting imbalance of the rotor.

For the value of $c_b = 0.001$, there is not enough race damping for the ABB to operate successfully. At first the balls oscillate about the unstable balanced positions, before undergoing chaotic type motions and then destabilising completely at around $t \approx 650$. The resulting vibrations are an order of magnitude worse than the level for the rotor without the ABB.

As the race damping is increased to $c_b = 0.01$, the balls again oscillate about their balanced positions and the bottom race balls (blue curves) also initially complete some full revolutions of

the race. However, in this instance the balanced state is stable and the ABB eventually achieves balance.

For a higher value of race damping $c_b = 0.1$, these initial oscillations are significantly reduced, and the balls quickly reach their balanced positions. Furthermore, the balanced state was found to be globally stable, which as we shall discuss in Section 2.3.3, is not the case for the middle example with $c_b = 0.01$.

Thus, we ideally desire that the motions of the balls are overdamped, as this helps to eliminate the destabilised state in which the balls lag the rotor and whirl about the race. However, an appropriate choice for the race damping may prove difficult in practice. For example, if the balls whirl about the race during the rotor run-up then the temperature of the damping fluid may rise and its viscosity could fall as a consequence.

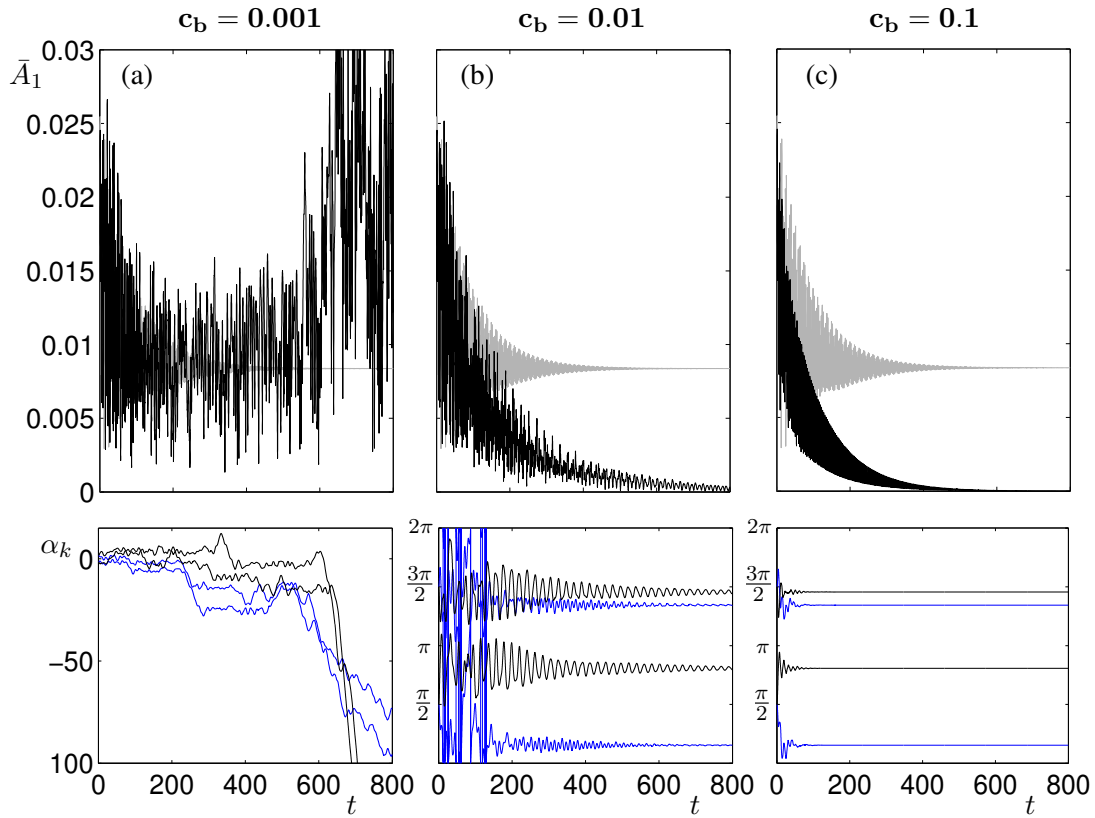


Figure 2.12. Influence of ball damping c_b on the support vibrations and ball positions. The parameter set used is the same as that in Section 2.2.4 with Ω and m fixed at $(\Omega, m) = (3.5, 0.005)$. The vibration levels \bar{A}_1 are plotted similarly to Figure 2.11 and the corresponding ball angles are shown below with black lines for α_1, α_2 (top race) and blue lines for α_3, α_4 (bottom race). Initial conditions are fixed so that the rotor begins in the undeflected position and the balls in each race start on opposite sides with $(\alpha_1, -\alpha_2) = (\alpha_3, -\alpha_4) = \pi/2$.

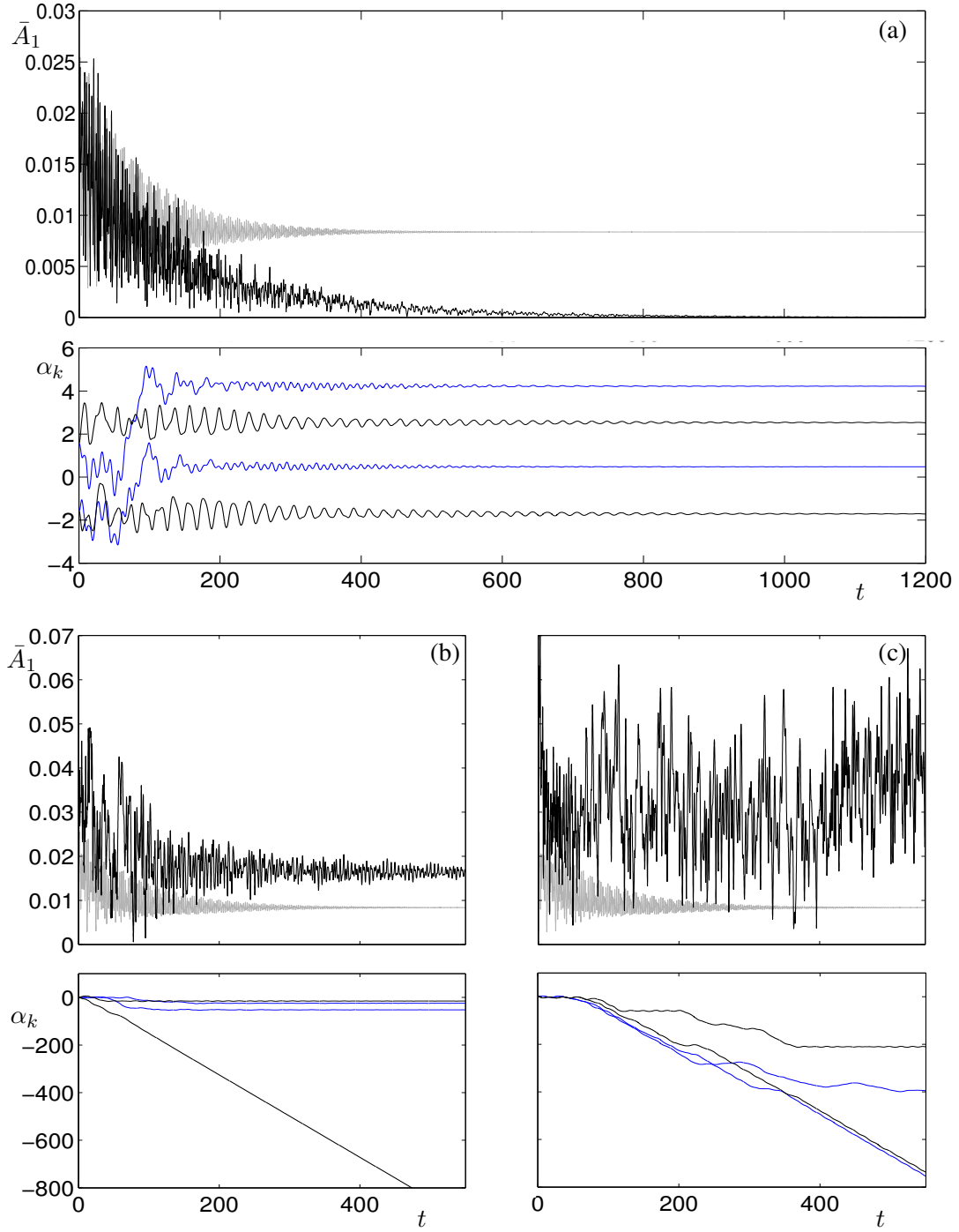


Figure 2.13. Numerical simulations for the dynamic imbalance $(\varepsilon, \chi, \beta) = (0.005, 0.005, 1.0)$. The parameter set used is the same as that in Section 2.2.4 with Ω and m fixed at $(\Omega, m) = (3.5, 0.005)$. This position is also highlighted by a (●) in Figure 2.9. The vibration levels \bar{A}_1 are plotted similarly to Figure 2.11 and the corresponding ball angles are shown below with black lines for α_1, α_2 (top race) and blue lines for α_3, α_4 (bottom race). Initial conditions are (a) $(\alpha_1, -\alpha_2) = (\alpha_3, -\alpha_4) = \pi/2$, (b) $(\alpha_1, -\alpha_2) = \pi/3$, $(\alpha_3, -\alpha_4) = 2\pi/3$ and (c) $(\alpha_1, \alpha_2) = 0$, $(\alpha_3, \alpha_4) = \pi$.

2.3.3 The effect of varying the initial conditions

We now turn to the effect that the initial conditions have on the operation of the ABB. It was found that there was little sensitivity to typical variations in the initial values of the vibrational coordinates (x, y, ϕ_x, ϕ_y) or their velocities $(\dot{x}, \dot{y}, \dot{\phi}_x, \dot{\phi}_y)$, however the initial value of the ball positions α_k can have a dramatic impact on the outcome of the system. We again consider the dynamic imbalance case in which $(\varepsilon, \chi, \beta) = (0.005, 0.005, 1.0)$ and $(\Omega, m) = (3.5, 0.005)$. In particular we focus on the case with $c_b = 0.01$, which is indicated in Figure 2.9 and lies in the stable balanced region. In Figure 2.13 we display the vibration level \bar{A}_1 for the ABB together with the angular displacement of the balancing balls plotted in the same manner as in Figure 2.12. Figure 2.13(a) illustrates the same results as that of Figure 2.12(b) in which the initial conditions were given by (2.25). Here the balls are attracted to the balanced state **B** with angular positions α_k given by (2.17).

In panel (b) we take the initial conditions $\alpha_1 = -\alpha_2 = \pi/3$, $\alpha_3 = -\alpha_4 = 2\pi/3$, this has the effect of increasing the initial couple imbalance of the rotor. Here the device settles down to a periodic motion where the vibration level is about twice that of the rotor without the ABB. We find that one of the balls in the top race lags behind the rotor with $\dot{\alpha} = -\frac{1}{2}\Omega$. Therefore, this ball only performs one revolution for every two of the rotor. Note that a model which included partitions of the race [27] or allowed for collisions between balls would prevent such dynamics. Finally, in Figure 2.13(c) we consider starting conditions where the initial couple balance is maximised so that $\alpha_1 = \alpha_2 = 0$, and $\alpha_3 = \alpha_4 = \pi$. In this case the rotor appears to undergo a chaotic motion and the vibration level of the rotor is an order of magnitude worse.

2.4 Discussion

In this chapter, we have provided the first nonlinear bifurcation analysis of a two-plane automatic balancer for rigid rotors. It has been demonstrated that the use of rotating coordinates enables an autonomous formulation for the equations of motion. Two-parameter stability charts obtained by numerical continuation show that the considered device can effectively eliminate imbalances arising from both mass eccentricity and principal axis misalignment. However, the balancing process only works for sufficiently high rotation speeds above the second critical frequency [58].

In our investigations, we have found all the bifurcations which appear in the planar analysis of the ABB [14, 28], together with additional bifurcations that occur as a result of the out-of-plane motions. Furthermore, we have highlighted how the symmetry properties of the imbalance affects the degeneracy of the bifurcation at which the balanced state is born.

In addition, we have presented numerical simulations which illustrate the coexistence of the balanced state with other less desirable dynamics. Here as expected, the probability of successful operation is maximised by releasing the balls from directly opposite positions on the race so that the initial imbalance is not increased.

The parameter set that we have so far considered has been highly symmetric, therefore care should be taken when making inferences as to the performance of an automatic balancer on a real machine. Consequently, in the next chapter we shall continue by assessing the robustness of the ABB dynamics with regards to asymmetries in the mechanical set-up.

Chapter 3

Breaking the symmetry

Many of the results that are presented in this chapter have been published in [51] and [50].

In the previous chapter an autonomous system of governing equations for the two-plane ABB was derived through the use of Lagrange's method and rotating coordinates. A symmetric set-up was then considered and numerical continuation techniques were used to map out the stability boundaries of the balanced state in various parameter planes. However, the set-up on a real machine is usually asymmetric. For example, the supports may be anisotropic or the balancing planes may not be equally spaced from the midspan.

The influence of support anisotropy in a single plane balancer was considered by both Olsson [45] and Ryzhik *et al.* [52]. In these studies, time averaging approximations were used in order to provide linear stability analyses. However, for such a highly nonlinear device as the ABB, these techniques cannot accurately predict the behaviour of the system. Here, we shall extend the research by providing a nonlinear bifurcation analysis of a two-plane ABB with various asymmetric set-ups. In particular, the robustness of the balanced state will be assessed.

The rest of this chapter is organised as follows. In Section 3.1 we develop the ABB model so that it includes effects such as support anisotropy and rotor acceleration. In Section 3.2 the symmetry of the imbalance is considered and we also derive a necessary condition for the stability of the balanced state. Next, in Sections 3.3 and 3.4 we investigate set-ups in which either the supports or the ABB device are asymmetric. Here we focus on using numerical bifurcation theory in order to compute the stable regions of balanced operation. Finally, in Section 3.5 we supplement the results of the steady state analysis by providing simulations of the ABB dynamics that also include the effect of the rotor run-up.

3.1 Equations of motion

In this section we shall extend the ABB model by including effects such as anisotropy of the supports and rotor acceleration. These features can be incorporated by adding the motion of the balls to the appropriate linear rotor equations.

3.1.1 Rotating coordinates

The governing equations for an isotropic two-plane ABB were given in the previous chapter in (2.11) and (2.12). This system was written with respect to rotating coordinates, and in addition, ball moment terms n_{ϕ_y} and $n_{-\phi_x}$ that are due to the rotor tilting motions were also included. However, the inclinational coordinates (ϕ_y, ϕ_x) are small, say $\mathcal{O}(\delta)$ with δ a small quantity. Therefore, provided the balancing planes z_k are set $\mathcal{O}(R)$ away from the midspan (where R is the race radius), then we shall have

$$z_k \gg R\phi_y, R\phi_x.$$

The above relation comes from comparing the sizes of the lever arms that give rise to the ball moment terms. This condition implies that the additional n_{ϕ_y} and $n_{-\phi_x}$ moments are negligible compared to the moments that are due to the z_k arm of the balancing plane. By comparing simulations and stability charts we have found that an excellent approximation is obtained by neglecting the contribution from the n_{ϕ_y} and $n_{-\phi_x}$ terms. This simplification enables (2.11) to be rewritten in a more concise format as

$$\begin{aligned} \begin{bmatrix} \mathbf{M} & \mathbf{0} \\ \mathbf{0} & \mathbf{M} \end{bmatrix} \ddot{\mathbf{x}} + \begin{bmatrix} \mathbf{C} & -\Omega(2\mathbf{M}-\mathbf{G}) \\ \Omega(2\mathbf{M}-\mathbf{G}) & \mathbf{C} \end{bmatrix} \dot{\mathbf{x}} + \begin{bmatrix} \mathbf{K}-\Omega^2(\mathbf{M}-\mathbf{G}) & -\Omega\mathbf{C} \\ \Omega\mathbf{C} & \mathbf{K}-\Omega^2(\mathbf{M}-\mathbf{G}) \end{bmatrix} \mathbf{x} \\ = \Omega^2 \begin{bmatrix} \text{Re}(\mathbf{f}_I) \\ \text{Im}(\mathbf{f}_I) \end{bmatrix} + \sum_{k=1}^4 \left[(\Omega + \dot{\alpha}_k)^2 \text{Re}(\mathbf{f}_{b_k} e^{i\alpha_k}) + \ddot{\alpha}_k \text{Im}(\mathbf{f}_{b_k} e^{i\alpha_k}) \right] \\ - \left[(\Omega + \dot{\alpha}_k)^2 \text{Im}(\mathbf{f}_{b_k} e^{i\alpha_k}) - \ddot{\alpha}_k \text{Re}(\mathbf{f}_{b_k} e^{i\alpha_k}) \right]. \end{aligned} \quad (3.1)$$

The above equation is coupled to the motions of the balancing balls, which from (2.12) are given by

$$\begin{aligned} m_k R_k^2 \ddot{\alpha}_k + c_b \dot{\alpha}_k = m_k R_k \left\{ \left[(\ddot{x} + z_k \ddot{\phi}_y) - 2\Omega (\dot{y} - z_k \dot{\phi}_x) - \Omega^2 (x + z_k \phi_y) \right] \sin \alpha_k \right. \\ \left. - \left[(\ddot{y} - z_k \ddot{\phi}_x) + 2\Omega (\dot{x} + z_k \dot{\phi}_y) - \Omega^2 (y - z_k \phi_x) \right] \cos \alpha_k \right\}, \quad k = 1, \dots, 4. \end{aligned} \quad (3.2)$$

In equation (3.1) the vector of the rotor degrees of freedom is $\mathbf{x} = [x, \phi_y, y, -\phi_x]^T$ and the mass, gyroscopic, damping and stiffness matrices are given respectively by

$$\mathbf{M} = \begin{bmatrix} M & 0 \\ 0 & J_t \end{bmatrix} + \sum_{k=1}^4 \begin{bmatrix} m_k & m_k z_k \\ m_k z_k & m_k z_k^2 \end{bmatrix}, \quad \mathbf{G} = \begin{bmatrix} 0 & 0 \\ 0 & J_p \end{bmatrix}, \quad \mathbf{C} = \begin{bmatrix} c_{11} & c_{12} \\ c_{12} & c_{22} \end{bmatrix}, \quad \mathbf{K} = \begin{bmatrix} k_{11} & k_{12} \\ k_{12} & k_{22} \end{bmatrix}. \quad (3.3)$$

In addition, the mass imbalance and ball vectors are given by

$$\mathbf{f}_I = \begin{bmatrix} M\varepsilon e^{i\beta} \\ \chi(J_t - J_p) \end{bmatrix} \quad \text{and} \quad \mathbf{f}_{b_k} = \begin{bmatrix} m_k R_k \\ m_k R_k z_k \end{bmatrix}, \quad k = 1, \dots, 4. \quad (3.4)$$

We have kept the equations in dimensional form as this will be more appropriate for the study of experimental ABBs. However, as shown in Section 2.1.4, the system can be non-dimensionalised by rescaling with respect to the mass of the rotor M , the race radius R and the critical frequency associated with the cylindrical whirl $\Omega_{\text{cyl}} = \sqrt{\frac{k_{11}}{M}}$. In practice this procedure can be easily achieved by choosing the parameter set

$$M \equiv 1, \quad R \equiv 1 \quad \text{and} \quad k_{11} \equiv 1.$$

3.1.2 Inertial frame and support anisotropy

As yet, we have only considered isotropic set-ups in which the equations of motion can be rendered autonomous by writing them with respect to rotating coordinates. However, if the rotor supports are anisotropic then the rotor angle Ωt cannot be eliminated in this way. Therefore it is more convenient to rewrite (3.1) and (3.2) in terms of the space frame coordinates which gives

$$\begin{aligned} & \begin{bmatrix} \mathbf{M} & \mathbf{0} \\ \mathbf{0} & \mathbf{M} \end{bmatrix} \ddot{\mathbf{X}} + \begin{bmatrix} \mathbf{C}_X & \Omega \mathbf{G} \\ -\Omega \mathbf{G} & \mathbf{C}_Y \end{bmatrix} \dot{\mathbf{X}} + \begin{bmatrix} \mathbf{K}_X & \mathbf{0} \\ \mathbf{0} & \mathbf{K}_Y \end{bmatrix} \mathbf{X} \\ &= \Omega^2 \begin{bmatrix} \text{Re}(\mathbf{f}_I e^{i\Omega t}) \\ \text{Im}(\mathbf{f}_I e^{i\Omega t}) \end{bmatrix} + \sum_{k=1}^4 \left[(\Omega + \dot{\alpha}_k)^2 \text{Re}(\mathbf{f}_{b_k} e^{i(\Omega t + \alpha_k)}) + \ddot{\alpha}_k \text{Im}(\mathbf{f}_{b_k} e^{i(\Omega t + \alpha_k)}) \right] \\ & \quad \left[(\Omega + \dot{\alpha}_k)^2 \text{Im}(\mathbf{f}_{b_k} e^{i(\Omega t + \alpha_k)}) - \ddot{\alpha}_k \text{Re}(\mathbf{f}_{b_k} e^{i(\Omega t + \alpha_k)}) \right], \end{aligned} \quad (3.5)$$

where the motion of the k th ball is given by

$$m_k R_k^2 \ddot{\alpha}_k + c_b \dot{\alpha}_k = m_k R_k \left((\ddot{X} + z_k \ddot{\phi}_Y) \sin(\Omega t + \alpha_k) - (\ddot{Y} - z_k \ddot{\phi}_X) \cos(\Omega t + \alpha_k) \right). \quad (3.6)$$

Here, $\mathbf{X} = [X, \phi_Y, Y, -\phi_X]^T$ are the space frame coordinates of the rotor degrees of freedom, and these are related to the rotating frame coordinates $\mathbf{x} = [x, \phi_y, y, -\phi_x]^T$ by the relations

$$\begin{bmatrix} X \\ Y \end{bmatrix} = \begin{bmatrix} \cos(\Omega t) & -\sin(\Omega t) \\ \sin(\Omega t) & \cos(\Omega t) \end{bmatrix} \begin{bmatrix} x \\ y \end{bmatrix} \quad \text{and} \quad \begin{bmatrix} \phi_Y \\ -\phi_X \end{bmatrix} = \begin{bmatrix} \cos(\Omega t) & -\sin(\Omega t) \\ \sin(\Omega t) & \cos(\Omega t) \end{bmatrix} \begin{bmatrix} \phi_y \\ -\phi_x \end{bmatrix}. \quad (3.7)$$

The mass, gyroscopic, damping and stiffness matrices are again given by (3.3), however, the stiffness and damping terms in the X and Y directions do not necessarily have to take the same values. The rotor and ball imbalance vectors \mathbf{f}_I and \mathbf{f}_{b_k} are also the same as those in (3.4), although as one can see from comparing (3.1) and (3.5) the angle Ωt now appears in their phases. We note that by ignoring the contribution from the balls in (3.5), we recover the equations of motion for a four-degree-of-freedom rotor on anisotropic supports [24, §6].

3.1.3 Complex coordinates

It is also possible to define a set of complex coordinates that allow the equations of motion to be written in a more compact form. For the rotating frame coordinates, we can take

$$\mathbf{r} = \begin{bmatrix} x + iy \\ \phi_y - i\phi_x \end{bmatrix}. \quad (3.8)$$

This definition allows the system of (3.1) and (3.2) to be written more concisely as

$$\begin{aligned} \mathbf{M}\ddot{\mathbf{r}} + [\mathbf{C} + i\Omega(2\mathbf{M} - \mathbf{G})]\dot{\mathbf{r}} + [\mathbf{K} - \Omega^2(\mathbf{M} - \mathbf{G}) + i\Omega\mathbf{C}]\mathbf{r} \\ = \Omega^2\mathbf{f}_I + \sum_{k=1}^4 \left((\Omega + \dot{\alpha}_k)^2 - i\ddot{\alpha}_k \right) \mathbf{f}_{b_k} e^{i\alpha_k}, \\ m_k R_k^2 \ddot{\alpha}_k + c_b \dot{\alpha}_k + \text{Im} \left\{ [(\ddot{\mathbf{r}} + 2i\Omega\dot{\mathbf{r}} - \Omega^2\mathbf{r}) \cdot \mathbf{f}_{b_k}] e^{-i\alpha_k} \right\} = 0, \quad k = 1, \dots, 4. \end{aligned} \quad (3.9)$$

Similarly, for the space frame coordinates we take

$$\mathbf{s} = \begin{bmatrix} X + iY \\ \phi_Y - i\phi_X \end{bmatrix}. \quad (3.10)$$

This enables the transformation that is given by (3.7) to be reduced to

$$\mathbf{s} = \mathbf{r} e^{i\Omega t}. \quad (3.11)$$

By introducing mean and deviatoric matrices, complex coordinates can also be used to describe an anisotropic set-up. For the stiffnesses we define

$$\begin{aligned}\mathbf{K}_m &= \frac{1}{2}(\mathbf{K}_X + \mathbf{K}_Y), \\ \mathbf{K}_d &= \frac{1}{2}(\mathbf{K}_X - \mathbf{K}_Y),\end{aligned}\quad (3.12)$$

and similar expressions for the damping matrices can also be given. The system of (3.5) and (3.6) can then be written in a more compact form as

$$\begin{aligned}\mathbf{M}\ddot{\mathbf{s}} + (\mathbf{C}_m - i\Omega\mathbf{G})\dot{\mathbf{s}} + \mathbf{K}_m\mathbf{s} + \mathbf{C}_d\dot{\bar{\mathbf{s}}} + \mathbf{K}_d\bar{\mathbf{s}} \\ = \Omega^2\mathbf{f}_I e^{i\Omega t} + \sum_{k=1}^4 ((\Omega + \dot{\alpha}_k)^2 - i\ddot{\alpha}_k)\mathbf{f}_{b_k} e^{i(\Omega t + \alpha_k)}, \\ m_k R_k^2 \ddot{\alpha}_k + c_b \dot{\alpha}_k + \text{Im}((\ddot{\mathbf{s}} \cdot \mathbf{f}_{b_k}) e^{-i(\Omega t + \alpha_k)}) = 0, \quad k = 1, \dots, 4.\end{aligned}\quad (3.13)$$

where $\bar{\mathbf{s}}$ is the complex conjugate of \mathbf{s} . For further details on complex coordinates and anisotropic rotors, see for example [24, §6].

3.1.4 Rotor acceleration

Finally, we shall include the effect of the rotor run-up and run-down procedures. For this case, the imbalance angle θ_0 can no longer be taken to be Ωt , but must be treated as an independent variable. In addition, the angle of the balls will be denoted by $\theta_k = \theta_0 + \alpha_k$. The model has been generated by adding the motions of the balls to the generic non-stationary multi-degree-of-freedom rotor system that was given in [24, §11.4]. This combination yields

$$\begin{aligned}\mathbf{M}\ddot{\mathbf{s}} + (\mathbf{C}_m - i\dot{\theta}_0\mathbf{G})\dot{\mathbf{s}} + \mathbf{K}_m\mathbf{s} + \mathbf{C}_d\dot{\bar{\mathbf{s}}} + \mathbf{K}_d\bar{\mathbf{s}} \\ = (\dot{\theta}_0^2 - i\ddot{\theta}_0)\mathbf{f}_I e^{i\theta_0} + \sum_{k=1}^4 (\dot{\theta}_k^2 - i\ddot{\theta}_k)\mathbf{f}_{b_k} e^{i\theta_k}, \\ \tilde{J}_p \ddot{\theta}_0 + c_r \dot{\theta}_0 + \sum_{k=1}^4 c_b (\dot{\theta}_0 - \dot{\theta}_k) + \text{Im}((\ddot{\mathbf{s}} \cdot \mathbf{f}_I) e^{-i\theta_0}) = \tau(\dot{\theta}_0), \\ m_k R_k^2 \ddot{\theta}_k + c_b (\dot{\theta}_k - \dot{\theta}_0) + \text{Im}((\ddot{\mathbf{s}} \cdot \mathbf{f}_{b_k}) e^{-i\theta_k}) = 0, \quad k = 1, \dots, 4.\end{aligned}\quad (3.14)$$

The second equation describes the torsional behaviour of the rotor, here $\tilde{J}_p = J_p + J_t \chi^2 + M\varepsilon^2$ is the modified polar moment of inertia, $\tau(\dot{\theta}_0)$ is the driving torque generated by the motor and c_r is the torque damping.

The form of (3.14) suggests that automatic balancing can be viewed as a synchronization phenomena of coupled oscillators, see also [56] and [5, §7]. Namely, for smooth operation

we require that the ball speeds $\dot{\theta}_k$ synchronize with the rotor speed $\dot{\theta}_0$ and furthermore that the phases of the balls $\theta_k - \theta_0$ are such that their forcing cancels out, or at least reduces, the forcing from the rotor imbalance. In addition, the structural similarities of the second and third equations allows us to consider the balls as oscillators that are not acted upon by any external torque, but are driven solely through their coupling with the underlying vibrations of the rotor.

It is usual to assume that the motor can provide enough torque to realise a given angular velocity profile. Therefore, we shall impose the spin speed $\Omega(t) = \dot{\theta}_0(t)$ instead of considering the second equation of (3.14) with a given driving torque. For an isotropic set-up the equations can then be rendered autonomous by eliminating the rotor angle θ_0 through the use of the transformation $\mathbf{s} = \mathbf{r}e^{i\theta_0}$, this gives, c.f. (3.9)

$$\begin{aligned} M\ddot{\mathbf{r}} + [\mathbf{C} + i\Omega(2M - \mathbf{G})]\dot{\mathbf{r}} + \left[\mathbf{K} - \Omega^2(M - \mathbf{G}) + i(\dot{\Omega}\mathbf{M} + \Omega\mathbf{C}) \right] \mathbf{r} \\ = (\Omega^2 - i\dot{\Omega})\mathbf{f}_I + \sum_{k=1}^4 \left((\Omega + \dot{\alpha}_k)^2 - i(\dot{\Omega} + \ddot{\alpha}_k) \right) \mathbf{f}_{b_k} e^{i\alpha_k}, \\ m_k R_k^2 (\dot{\Omega} + \ddot{\alpha}_k) + c_b \dot{\alpha}_k + \text{Im} \left\{ \left[(\ddot{\mathbf{r}} + 2i\Omega\dot{\mathbf{r}} - (\Omega^2 - i\dot{\Omega})\mathbf{r}) \cdot \mathbf{f}_{b_k} \right] e^{-i\alpha_k} \right\} = 0, \quad k = 1, \dots, 4. \end{aligned} \quad (3.15)$$

We have now developed all the ABB models that are necessary to describe the effects that are under consideration in this chapter. In the next section, we will discuss how the symmetry properties of the rotor can be used to analyse the bifurcation structure of the ABB.

3.2 Asymmetry of the imbalance

We shall consider a symmetric isotropic set-up which has a reflectional symmetry in the transverse plane that includes the centre of rotation C , see Figure 2.1. We then have the following parameter set

$$\begin{aligned} m_k = m, \quad R_k = R, \quad z_{1,2} = -z_{3,4} = z, \\ l_1 = l_2 = l, \quad k_1 = k_2 = k, \quad c_1 = c_2 = c, \end{aligned}$$

and from (2.8) and (2.10) we also obtain stiffness and damping matrices of the form

$$\mathbf{K} = \begin{bmatrix} 2k & 0 \\ 0 & 2kl^2 \end{bmatrix} \quad \text{and} \quad \mathbf{C} = \begin{bmatrix} 2c & 0 \\ 0 & 2cl^2 \end{bmatrix}.$$

In addition, because the interchange of ball races must leave the system invariant, we require that each race contains an equal amount of imbalance. This occurs, for example, when there is a pure static imbalance or a pure couple imbalance. The physical configurations of the possible

ABB steady states were illustrated for these cases in Figures 2.4 and 2.8, respectively. Here it was noted that the reflected **C3** state, with split balls in the top race and coincident balls in the bottom race, is physically equivalent to the illustrated arrangements in which the roles of the races are reversed.

An example of a bifurcation diagram for the static imbalance case is shown in Figure 3.1(a). Here the mass of the balls m is the varying parameter, the solution measure is the Euclidean norm L_2 and the rotation speed $\Omega = 3$ is supercritical to both the cylindrical and conical resonances. We find that the balanced state **B** is born at a degenerate pitchfork bifurcation that involves both the coincident states **C1** and **C3**. However, if we now add a small misalignment $\chi = 0.001$ to the mass imbalance, we can see that the bifurcation unfolds into three non-degenerate pitchforks, panel (b). This unfolding occurs because the symmetry between the two races is broken. When a misalignment is added, there is more imbalance at one race (in this instance the top one) than at the other. As a consequence, the steady state **C3** separates into two physically different solutions. The configuration with coincident balls in the top race is called **Ct3**, whereas the corresponding state with the bottom race balls coincident is **Cb3**.

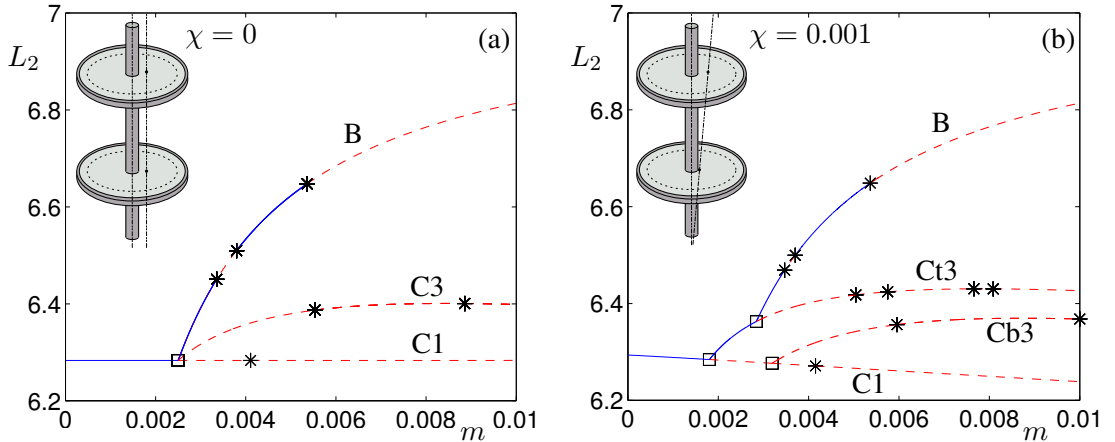


Figure 3.1. One parameter bifurcation diagrams in m that illustrate the unfolding of the pitchfork bifurcation at which the balanced state is born. Panel (a) is for a pure static imbalance with $\varepsilon = 0.01$, $\Omega = 3$ and the other parameters taking values as given in (2.19) and (2.21). In panel (b) we unfold the degenerate pitchfork by adding a small misalignment $(\chi, \beta) = (0.001, 0)$ that acts to break the symmetry between the two races.

Although we may intuitively expect the behaviour that is seen in Figure 3.1, a more detailed investigation into the effect of symmetries will require some of the techniques of equivariant bifurcation theory. For further details on this topic see for example [26], [12] and in particular [34].

3.2.1 Symmetry identification

We can recast the equations of motion into a first order system in the usual way by defining a state vector

$$\mathbf{u} = \left(x, \dot{x}, y, \dot{y}, \phi_x, \dot{\phi}_x, \phi_y, \dot{\phi}_y, \alpha_1, \dot{\alpha}_1, \alpha_2, \dot{\alpha}_2, \alpha_3, \dot{\alpha}_3, \alpha_4, \dot{\alpha}_4 \right),$$

and substituting it component-wise back into (3.1) and (3.2). The system then takes the form

$$\mathcal{M}(\mathbf{u}, \mu) \frac{d\mathbf{u}}{dt} = \mathcal{F}(\mathbf{u}, \mu). \quad (3.16)$$

where μ is the bifurcation parameter, $\mathcal{M} : \mathbb{R}^n \times \mathbb{R} \rightarrow \mathbb{R}^{n^2}$ is a generalised mass matrix and $\mathcal{F} : \mathbb{R}^n \times \mathbb{R} \rightarrow \mathbb{R}^n$ is a smooth function.

Let γ be a linear transformation that acts on the state variables. For γ to be a symmetry of the system, it must transform both the equations and the state variables in the same manner. Considering just the left hand side of (3.16) we require that

$$\begin{aligned} \gamma \mathcal{M}(\mathbf{u}, \mu) \frac{d\mathbf{u}}{dt} &= \mathcal{M}(\gamma\mathbf{u}, \mu) \frac{d}{dt} (\gamma\mathbf{u}), \\ &= \mathcal{M}(\gamma\mathbf{u}, \mu) \gamma \frac{d\mathbf{u}}{dt}, \end{aligned}$$

where the second equality comes from the fact that γ is time independent. Since this condition must hold for all values of $\frac{d\mathbf{u}}{dt}$, we have that

$$\gamma \mathcal{M}(\mathbf{u}, \mu) \gamma^{-1} = \mathcal{M}(\gamma\mathbf{u}, \mu). \quad (3.17)$$

Similarly, for the right-hand side of the system we require that

$$\gamma \mathcal{F}(\mathbf{u}, \mu) = \mathcal{F}(\gamma\mathbf{u}, \mu). \quad (3.18)$$

Together (3.17) and (3.18) are the *equivariance conditions* for the generalised mass matrix \mathcal{M} , and the right-hand side function \mathcal{F} , respectively.

The set of symmetries $\{\gamma_1, \gamma_2, \dots\}$ form a group Γ under composition. In order to determine the group structure of Γ , we first need to find all the physical transformations that leave the ABB setup invariant. Because each ball is identical, the interchange of balls within a race is a symmetry and we denote these operations by

$$\gamma_{12} = (\alpha_1, \dot{\alpha}_1) \leftrightarrow (\alpha_2, \dot{\alpha}_2) \quad \text{and} \quad \gamma_{34} = (\alpha_3, \dot{\alpha}_3) \leftrightarrow (\alpha_4, \dot{\alpha}_4).$$

If in addition the imbalance is purely static¹ so that

$$(\varepsilon, \chi, \beta) = (\varepsilon, 0, 0),$$

then the interchange of races γ_r is a further symmetry. However, because the switching of balls between races has the effect of reversing the direction of their moment terms, we must also change the sign of the angular state variables in order to keep the system invariant. Thus we have the symmetry

$$\gamma_r = (\alpha_1, \dot{\alpha}_1, \alpha_2, \dot{\alpha}_2, \phi_x, \dot{\phi}_x, \phi_y, \dot{\phi}_y) \leftrightarrow (\alpha_3, \dot{\alpha}_3, \alpha_4, \dot{\alpha}_4, -\phi_x, -\dot{\phi}_x, -\phi_y, -\dot{\phi}_y).$$

The transformations γ_{12} , γ_{34} and γ_r satisfy the equivariance conditions (3.17) and (3.18) and together they generate the symmetry group Γ .

Next, in order to determine the structure of Γ we consider the geometric realisation that is shown in Figure 3.2. By identifying the corner labels of a square with the ball indices, the group elements γ_{12} , γ_{34} and γ_r can be viewed as the indicated reflections. In addition, $\gamma_{12}\gamma_r$ is a rotation through an angle of $\pi/2$ and so the full symmetry group of the square D_4 can be generated. Thus we have the isomorphism $\Gamma \cong D_4$.

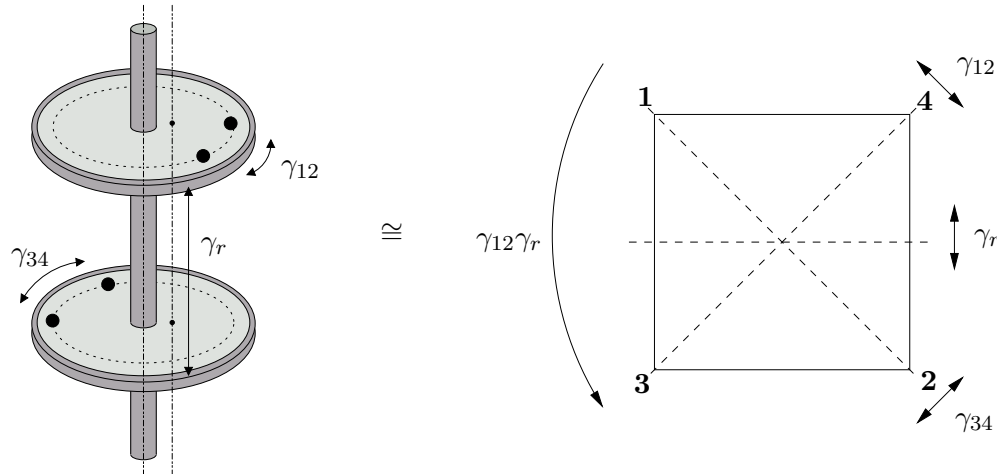


Figure 3.2. Physical and abstract realisations of the symmetry group that illustrates the isomorphism $\Gamma \cong D_4$ for the case of a static imbalance. Here the corner labels of the square represent the indices of the balls.

¹A sufficient condition; the necessary condition is that there is an equal amount of imbalance at each race.

3.2.2 Pitchfork bifurcation with \mathcal{D}_4 symmetry

Now that we have found the relevant symmetry group for our system, we may characterise the resulting solutions by employing some methods from equivariant bifurcation theory. The properties of steady state bifurcations with \mathcal{D}_4 symmetry are well known and we shall adapt the treatment that is given in [34, §4].

The normal form for a \mathcal{D}_4 -equivariant pitchfork bifurcation

From the equivariance conditions (3.17) and (3.18) we can deduce that the normal form for a pitchfork bifurcation in a system with this representation of \mathcal{D}_4 symmetry can be written in the form [34, (4.72)]

$$\begin{pmatrix} \dot{v}_1 \\ \dot{v}_2 \end{pmatrix} = \mu \begin{pmatrix} v_1 \\ v_2 \end{pmatrix} - a_1 \begin{pmatrix} v_1^3 \\ v_2^3 \end{pmatrix} - a_2 \begin{pmatrix} v_2^2 v_1 \\ v_1^2 v_2 \end{pmatrix}. \quad (3.19)$$

Here, a_1 and a_2 are real constants, μ is the bifurcation parameter and v_1 and v_2 correspond to the amplitudes of the eigenvectors that span the centre eigenspace. We can determine from the linearisation of the ABB system at the \mathcal{D}_4 -equivariant pitchfork bifurcation that the eigenvalues with zero real part have eigenvectors corresponding to the directions of $\hat{\alpha}_{12}$ and $\hat{\alpha}_{34}$; these are defined in (2.16) and relate to the angle between the two balls in each race. We can therefore identify the normal form variables v_1 and v_2 with $\hat{\alpha}_{12}$ and $\hat{\alpha}_{34}$.

Next, the bifurcation parameter is the mass of the balls m , and the bifurcation occurs when $m = m_c$ at which point the balls have enough mass to completely compensate for the imbalance. Therefore, in order to shift the bifurcation to zero we define

$$\mu = m - m_c, \quad (3.20)$$

and the critical ball mass for a static imbalance is

$$m_c = \frac{M\varepsilon}{4R}.$$

The normal form (3.19) can now be rewritten in the notation of the ABB system as

$$\begin{pmatrix} d\hat{\alpha}_{12}/dt \\ d\hat{\alpha}_{34}/dt \end{pmatrix} = \mu \begin{pmatrix} \hat{\alpha}_{12} \\ \hat{\alpha}_{34} \end{pmatrix} - a_1 \begin{pmatrix} \hat{\alpha}_{12}^3 \\ \hat{\alpha}_{34}^3 \end{pmatrix} - a_2 \begin{pmatrix} \hat{\alpha}_{34}^2 \hat{\alpha}_{12} \\ \hat{\alpha}_{12}^2 \hat{\alpha}_{34} \end{pmatrix}. \quad (3.21)$$

There are two non-trivial fixed point solutions for this reduced system. The first is given by

$$(\hat{\alpha}, \hat{\alpha}) \quad \text{with} \quad \hat{\alpha}^2 = \mu/(a_1 + a_2). \quad (3.22)$$

Here the balls are split evenly in both races and therefore this solution can be identified with the balanced state **B**. The second solution is of the type

$$(0, \hat{\alpha}) \quad \text{with} \quad \hat{\alpha}^2 = \mu/a_1. \quad (3.23)$$

In this case the balls are split in one of the races but remain coincident in the other, hence this solution can be identified with the state **C3**.

Determination of the coefficients a_1 and a_2 in terms of the ABB parameters

In the next part of this procedure we aim to find the coefficients a_1 and a_2 of the normal form (3.21) in terms of the ABB system parameters. One could use an explicit centre manifold reduction, however, this procedure is technically cumbersome. A simpler approach is to compute the best quadratic approximations to the bifurcation branches **B** and **C3** from the original system, and then compare these results with the corresponding solutions (3.22) and (3.23) that were obtained from the normal form.

In the case of a static imbalance, we have from the solution (2.17) for the balanced state **B**

$$\hat{\alpha}_{12} = \hat{\alpha}_{34} = \arccos\left(\frac{M\varepsilon}{4mR}\right).$$

Rearranging and expanding as a Taylor series for small angles we obtain

$$\begin{aligned} m &= \frac{M\varepsilon}{4R} \sec(\hat{\alpha}_{12}), \\ &= \frac{M\varepsilon}{4R} + \frac{M\varepsilon}{8R} \hat{\alpha}_{12}^2 + \mathcal{O}(4), \end{aligned}$$

and recalling (3.20) we have that

$$\mu \simeq \frac{M\varepsilon}{8R} \hat{\alpha}_{12}^2.$$

Thus, by comparing coefficients with the balanced state solution type (3.22) of the normal form we have

$$a_1 + a_2 = \frac{M\varepsilon}{8R}. \quad (3.24)$$

We shall now carry out the same procedure for the coincident state **C3**. In this case the steady state equations for the balls (2.18) yields

$$(x + z_k \phi_y) \sin \alpha_k = (y - z_k \phi_x) \cos \alpha_k, \quad k = 1 \dots 4, \quad \text{with} \quad z_{1,2} = -z_{3,4} = z, \quad (3.25)$$

where $x + z_k \phi_y$ and $y - z_k \phi_x$, are recognised as the x and y deflections of the race centres. For the solution type **C3** we require that $(x + z_k \phi_y, y - z_k \phi_x) = \mathbf{0}$ is satisfied by one of the

two races, so that its centre stays fixed at the undeflected position. Without loss of generality we assume that this occurs for the bottom race, that is to say for $z_{3,4} = -z$. We then have $(x - z\phi_y, y + z\phi_x) = \mathbf{0}$ so that

$$\phi_y = \frac{x}{z}, \quad \phi_x = -\frac{y}{z}. \quad (3.26)$$

The above relations allow the elimination of the tilt variables ϕ_x and ϕ_y from the steady state equations. Also, the balls in the top race are coincident $\alpha_1 = \alpha_2$ so that $\hat{\alpha}_{12} = 0$ and from (3.25) and (3.26) we obtain

$$\begin{aligned} \tan \alpha_1 &= \left(\frac{y - z\phi_x}{x + z\phi_y} \right) \\ &= \left(\frac{y}{x} \right). \end{aligned}$$

Next we consider the steady state equations for the vibrational coordinates. By setting all time derivatives of the system (3.1) to zero we arrive at

$$\begin{aligned} &\begin{bmatrix} \mathbf{K} - \Omega^2(\mathbf{M} - \mathbf{G}) & -\Omega\mathbf{C} \\ \Omega\mathbf{C} & \mathbf{K} - \Omega^2(\mathbf{M} - \mathbf{G}) \end{bmatrix} \mathbf{x} \\ &= \Omega^2 \begin{bmatrix} M\varepsilon \\ 0 \\ 0 \\ 0 \end{bmatrix} + 2mR\Omega^2 \begin{bmatrix} \cos \hat{\alpha}_{12} \cos \bar{\alpha}_{12} + \cos \hat{\alpha}_{34} \cos \bar{\alpha}_{34} \\ z (\cos \hat{\alpha}_{12} \cos \bar{\alpha}_{12} - \cos \hat{\alpha}_{34} \cos \bar{\alpha}_{34}) \\ \cos \hat{\alpha}_{12} \sin \bar{\alpha}_{12} + \cos \hat{\alpha}_{34} \sin \bar{\alpha}_{34} \\ z (\cos \hat{\alpha}_{12} \sin \bar{\alpha}_{12} + \cos \hat{\alpha}_{34} \sin \bar{\alpha}_{34}) \end{bmatrix}. \end{aligned} \quad (3.27)$$

Here the contributions from the balls have been rewritten in terms of the average and differential angular displacements, which are $\bar{\alpha}_{12}, \bar{\alpha}_{34}$ and $\hat{\alpha}_{12}, \hat{\alpha}_{34}$ respectively. It is not possible to find a closed form solution to (3.27), however, if we consider the case with no damping $\mathbf{C} = \mathbf{0}$ then the equations simplify due to the decoupling between the x and y directions. As a consequence, we find that part of the physically realisable solution is given by

$$y = 0 \quad \text{and} \quad \bar{\alpha}_{12} = \bar{\alpha}_{34} = \pi.$$

Thus summarising from (3.26) onwards, for the case with no damping we have a **C3** solution type of the form

$$\mathbf{x} = [x, \phi_y, y, -\phi_x]^T = [x, x/z, 0, 0]^T \quad \text{and} \quad [\bar{\alpha}_{12}, \hat{\alpha}_{12}, \bar{\alpha}_{34}, \hat{\alpha}_{34}]^T = [\pi, 0, \pi, \hat{\alpha}_{34}]^T. \quad (3.28)$$

Substituting this solution back into (3.27), we find that the bottom two rows are identically

zero, and from expanding the top two rows we obtain

$$\begin{aligned}(k_{11} - \Omega^2(M + 4m))x &= \Omega^2(M\varepsilon - 2mR(\cos\hat{\alpha}_{34} + 1)), \\ (k_{22} - \Omega^2(J_t + 4mz^2 - J_p))\left(\frac{x}{z}\right) &= 2mR\Omega^2z(\cos\hat{\alpha}_{34} - 1).\end{aligned}$$

Then by eliminating x and rearranging for mR we get

$$mR = \frac{M\varepsilon}{2} [(\kappa + 1)\cos\hat{\alpha}_{34} + (1 - \kappa)]^{-1}, \quad (3.29)$$

where

$$\begin{aligned}\kappa &= \frac{z^2(k_{11} - (M + 4m)\Omega^2)}{k_{22} - \Omega^2(J_t + 4mz^2 - J_p)}, \\ &= \frac{z^2\left(1 - \left(\frac{\Omega}{\Omega_{\text{cyl}}}\right)^2\right)}{l^2\left(1 - \left(\frac{\Omega}{\Omega_{\text{con}}}\right)^2\right)},\end{aligned} \quad (3.30)$$

with

$$\Omega_{\text{cyl}} = \sqrt{\frac{k_{11}}{M + 4m}} \quad \text{and} \quad \Omega_{\text{con}} = \sqrt{\frac{k_{22}}{J_t + 4mz^2 - J_p}}.$$

The above expressions can be recognised as the critical frequencies for the cylindrical and conical whirls respectively, which are modified to include the contribution from the balls. Next we expand (3.29) as a Taylor series for small angles to give

$$m = \frac{M\varepsilon}{4R} + \frac{M\varepsilon(1 + \kappa)}{16R}\hat{\alpha}_{34}^2 + \mathcal{O}(4),$$

so that

$$\mu \simeq \frac{M\varepsilon(1 + \kappa)}{16R}\hat{\alpha}_{34}^2.$$

By comparison with the coefficient of the **C3** solution type (3.23) of the normal form we may identify

$$a_1 = \frac{M\varepsilon(1 + \kappa)}{16R}.$$

Thus from (3.24) we finally obtain

$$a_1 = \frac{M\varepsilon(1 + \kappa)}{16R} \quad \text{and} \quad a_2 = \frac{M\varepsilon(1 - \kappa)}{16R}. \quad (3.31)$$

It is clear from (3.30) that when Ω is above or below both the critical speeds then $\kappa > 0$,

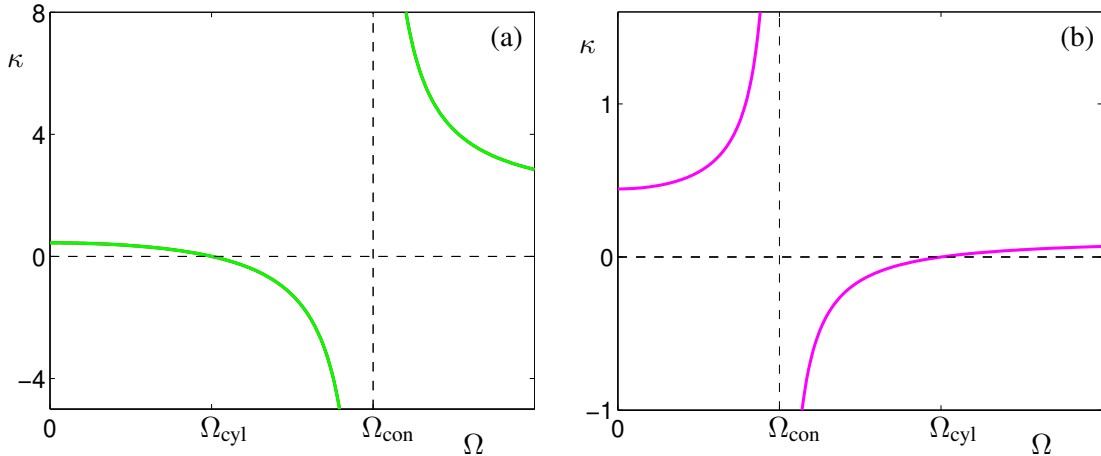


Figure 3.3. Plots of $\kappa(\Omega)$ as given by equation (3.30). Panel (a) is for the case with $\Omega_{\text{con}} > \Omega_{\text{cyl}}$, whereas panel (b) is for a set-up with $\Omega_{\text{cyl}} > \Omega_{\text{con}}$. In both cases κ is negative in between the critical speeds and is positive otherwise.

and so $a_1 > a_2$. Conversely, when Ω lies in between the two critical speeds then $\kappa < 0$ and so $a_2 > a_1$, see also Figure 3.3. In summary, we have the conditions

$$\begin{aligned} a_1 &> a_2 & \text{for } \Omega < \Omega_1 \text{ or } \Omega > \Omega_2, \\ a_2 &> a_1 & \text{for } \Omega_1 < \Omega < \Omega_2. \end{aligned} \quad (3.32)$$

Here, Ω_1 and Ω_2 are the first and second critical speeds respectively, and as we shall discuss next, the comparative sizes of a_1 and a_2 will determine the relative stabilities of the bifurcating branches.

Stability of the bifurcation branches

At this point, we remind the reader that the following stability analysis is only valid for the dynamics on the centre manifold of the \mathcal{D}_4 -equivariant pitchfork, that is to say, for the reduced system of (3.21). In the complete system, the trivial branch **C1** may be unstable due to additional pitchfork or Hopf bifurcations, see for example Figure 2.5(c). Nevertheless, a stable **B** type solution in the normal form is a prerequisite for stability of the balanced state in the full model.

The eigenvalues of the Jacobian matrix can be used to find the stability of the bifurcation branches. From the normal form (3.21) we can compute

$$Df = \frac{df_i}{d\hat{\alpha}_j} = \begin{pmatrix} \mu - 3a_1\hat{\alpha}_{12}^2 - a_2\hat{\alpha}_{34}^2 & -2a_2\hat{\alpha}_{12}\hat{\alpha}_{34} \\ -2a_2\hat{\alpha}_{12}\hat{\alpha}_{34} & \mu - 3a_1\hat{\alpha}_{34}^2 - a_2\hat{\alpha}_{12}^2 \end{pmatrix}. \quad (3.33)$$

Evaluating this at the **C3** type solution with $\hat{\alpha}_{12} = 0$, $\hat{\alpha}_{34}^2 = \mu/a_1$, gives

$$Df = \begin{pmatrix} \mu(1 - a_2/a_1) & 0 \\ 0 & -2\mu \end{pmatrix}, \quad (3.34)$$

and so this fixed point is stable if both $\mu > 0$ and $a_2 > a_1$. Hence, from condition (3.32) we require that $\Omega_1 < \Omega < \Omega_2$.

Next, if we evaluate the Jacobian at the **B** type balanced solution with $\hat{\alpha}_{12} = \hat{\alpha}_{34}$ and $\hat{\alpha}_{12}^2 = \mu/(a_1 + a_2)$, we get

$$Df = \begin{pmatrix} -2a_1\mu/(a_1 + a_2) & -2a_2\mu/(a_1 + a_2) \\ -2a_2\mu/(a_1 + a_2) & -2a_1\mu/(a_1 + a_2) \end{pmatrix}. \quad (3.35)$$

It is easy to check that this matrix has eigenvalues -2μ and $-2\mu(a_1 - a_2)/(a_1 + a_2)$ with eigenvectors $(1, 1)$ and $(1, -1)$ respectively. Therefore, the solution is stable if both $\mu > 0$ and $a_1 > a_2$. Thus, again from (3.32), we require that either $\Omega < \Omega_1$ or $\Omega > \Omega_2$.

Finally, the trivial solution **C1** with $\hat{\alpha}_{12} = \hat{\alpha}_{34} = 0$ is stable if $\mu < 0$ and unstable for $\mu > 0$.

The bifurcation diagrams of the \mathcal{D}_4 -equivariant pitchfork are illustrated for the various regions of the (a_1, a_2) plane in Figure 3.4. The condition $a_1 + a_2 = \frac{M_e}{8R}$, from (3.24), implies that the particular bifurcation type for the ABB system must always lie on the thick dashed line. The position of the pitchfork on this line is then determined by $\kappa(\Omega)$. For example, if we assume that the balancing planes are inside the bearings so that $z < l$, then by (3.30) we have $0 < \kappa(0) < 1$. Therefore, from the expressions for the coefficients (3.31), we have $a_1 > a_2 > 0$, and so, the bifurcation type for $\Omega = 0$ starts in region (ii).

With regards to Figure 3.3 (a), if $\Omega_{\text{con}} > \Omega_{\text{cyl}}$ then $k'(\Omega) < 0$. Therefore, from equation (3.31) we find that as Ω increases, a_1 decreases and a_2 increases. Thus, the solution type always moves upwards and to the left and follows the green route. As Ω passes through Ω_{cyl} the pitchfork crosses from region (ii) to (i) and the solutions **B** and **C3** exchange stability. Next, as Ω increases further, the bifurcation type goes from (i) to (vii) and **C3** also loses its stability. Then as Ω passes through Ω_{con} , κ switches from $-\infty$ to $+\infty$ and the pitchfork traverses, via infinity, from region (vii) to (iii). Hence, the stability of the balanced state **B** is regained.

The situation is similar for the less common set-up with $\Omega_{\text{cyl}} > \Omega_{\text{con}}$. With regards to Figure 3.3 (b), we have that $k'(\Omega) > 0$, and so the solution type moves down and to the right as Ω increases (magenta route). The balanced state **B** initially becomes unstable as Ω passes through Ω_{con} and the pitchfork switches via infinity from region (iii) to (vii). Its stability is later regained when the bifurcation type crosses from (i) to (ii) as Ω passes through Ω_{cyl} .

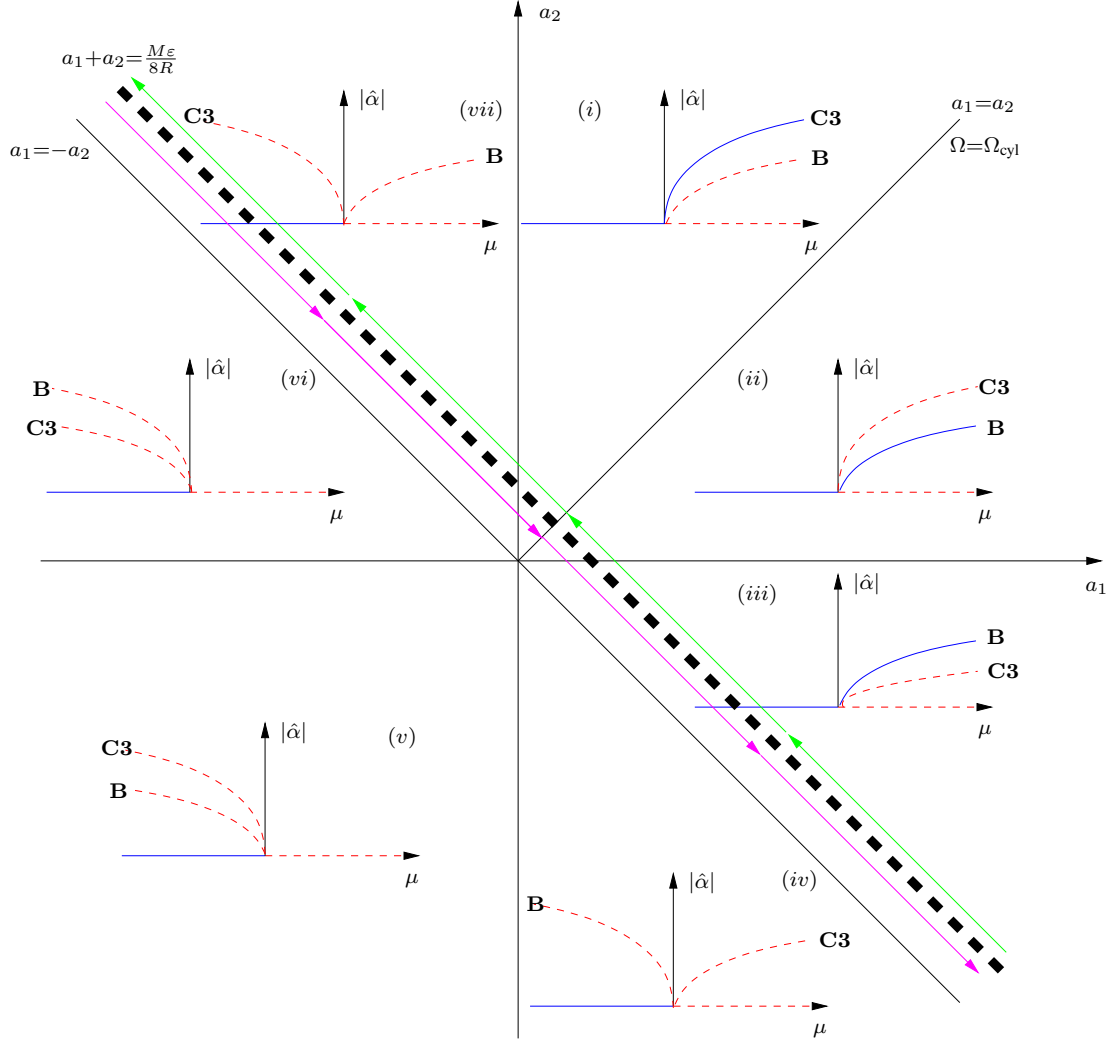


Figure 3.4. Bifurcation diagrams for the normal form of the \mathcal{D}_4 -equivariant pitchfork bifurcation for various values of the coefficients a_1 and a_2 in equation (3.21). Solid blue lines represent stable solutions and dashed red lines unstable solutions. Branches of the balanced state **B** are of the type $(\hat{\alpha}, \hat{\alpha})$ where the balls are split evenly in both races and branches of the state **C3** are of the type $(0, \hat{\alpha})$ where the balls are split in one race and remain coincident in the other. For the ABB system with eccentricity ε , the coefficients satisfy $a_1 + a_2 = \frac{M\varepsilon}{8R}$ and the bifurcation type must lie on the thick dashed line. If $\Omega_{\text{con}} > \Omega_{\text{cyl}}$ then as Ω increases the pitchfork type will follow the green route passing from (ii) to (i) at Ω_{cyl} and from (vii) to (iii) via infinity at Ω_{con} . Alternatively, if $\Omega_{\text{cyl}} > \Omega_{\text{con}}$ then the pitchfork will follow the magenta route initially switching from (iii) to (vii) at Ω_{con} and then passing from (i) to (ii) at Ω_{cyl} .

The \mathcal{D}_4 -equivariant bifurcation has now been characterised as it applies to a two-plane ABB. Furthermore, we have shown that the **B** type solution is stable at the pitchfork, provided that either $\Omega < \Omega_1$ or $\Omega > \Omega_2$. However, as mentioned above, the stability of the balanced state in the full system will be influenced by further bifurcations.

For example, when $\Omega < \Omega_1$, the trivial solution **C1** of the pitchfork is unstable whereas the stable branch is the corresponding **C̃1** state with coincident balls on the heavy side of the race. This behaviour for subcritical speeds is well established [60, 30] and can be understood intuitively by considering the ‘Working principle of the ABB’, see Section 1.3. More recently, Green *et al.* [28] demonstrated that the solutions **C1** and **C̃1** are connected via a saddle-node bifurcation. It was also shown that the states swap stability as the saddle-node passes through the pitchfork at the codimension-two bifurcation that occurs at $(m, \Omega) = (m_c, \Omega_1)$.

For $\Omega > \Omega_2$ the stability of the balanced state **B** is determined by the Hopf bifurcation curves that denote the onset of oscillatory instabilities. These boundaries were discussed in Chapter 2 and their computation will again form much of the basis for the remainder of this chapter. First, let us return to a consideration of the symmetry of the imbalance, this time focusing on the unfolding of the \mathcal{D}_4 -equivariant pitchfork as a misalignment is introduced.

3.2.3 Symmetry breaking between the races

The up-down symmetry of the ABB is broken when there is more imbalance at one race than at the other. We are then left with the two ball interchange symmetries $\gamma_{12} = (\alpha_1, \dot{\alpha}_1) \leftrightarrow (\alpha_2, \dot{\alpha}_2)$ and $\gamma_{34} = (\alpha_3, \dot{\alpha}_3) \leftrightarrow (\alpha_4, \dot{\alpha}_4)$, and together these form the symmetry group of the rectangle \mathcal{D}_2 . The appropriate reduced model can be adapted from the \mathcal{D}_4 -equivariant normal form (3.21) by breaking the imbalance symmetry between the races, this gives

$$\begin{pmatrix} d\hat{\alpha}_{12}/dt \\ d\hat{\alpha}_{34}/dt \end{pmatrix} = \begin{pmatrix} \mu_1 \hat{\alpha}_{12} \\ \mu_2 \hat{\alpha}_{34} \end{pmatrix} - a_1 \begin{pmatrix} \hat{\alpha}_{12}^3 \\ \hat{\alpha}_{34}^3 \end{pmatrix} - a_2 \begin{pmatrix} \hat{\alpha}_{34}^2 \hat{\alpha}_{12} \\ \hat{\alpha}_{12}^2 \hat{\alpha}_{34} \end{pmatrix}, \quad (3.36)$$

with

$$\mu_1 = m - m_t \quad \text{and} \quad \mu_2 = m - m_b.$$

Here m_t and m_b , which were introduced in (2.23), are the critical ball masses for the top and bottom races respectively.

The unfolding of the \mathcal{D}_4 -equivariant pitchfork is illustrated in Figure 3.5. The red and blue curves are the solutions of the full system, and except for the measure which is now $\|\hat{\alpha}\| = \sqrt{\hat{\alpha}_{12}^2 + \hat{\alpha}_{34}^2}$, these results are the same as those of Figure 3.1. The solid and dashed black curves are the approximations that have been computed from the reduced models (3.21) for panel(a) and (3.36) for (b). We find that the unfolding takes the correct form and also that

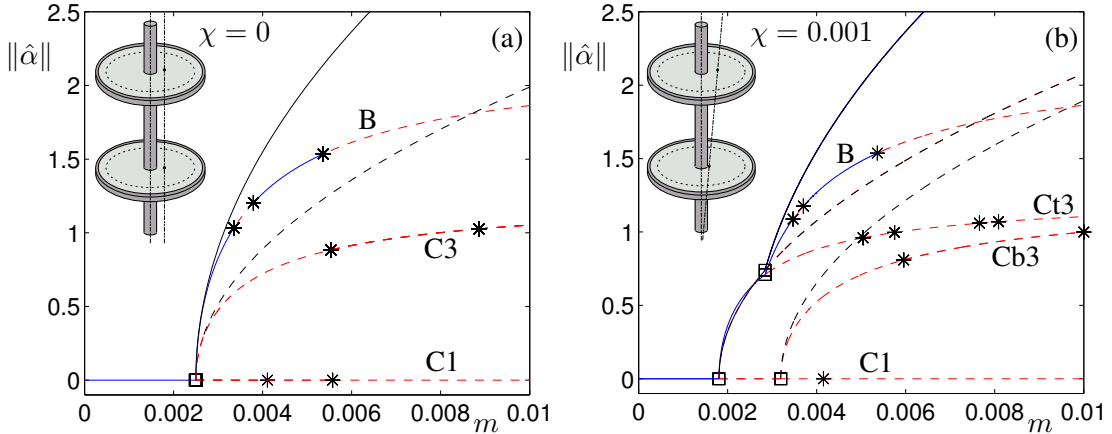


Figure 3.5. Comparison of the unfolding of the \mathcal{D}_4 -equivariant pitchfork as a small misalignment χ is introduced. The parameter values are the same as that of Figure 3.1, however, the norm is now given by $\|\hat{\alpha}\| = \sqrt{\hat{\alpha}_{12}^2 + \hat{\alpha}_{34}^2}$. The blue and red curves are the solutions to the full system (3.1) and (3.2), and the black solid and dashed curves are the approximations that are computed from the reduced models (3.21) for (a) and (3.36) for (b).

the relative stabilities of the solutions correspond. Furthermore, the quantitative match is good, and this is especially true for the \mathcal{D}_4 case (a). We note again that the method for finding the reduced model solutions was to calculate the best quadratic approximations to the branches of the \mathcal{D}_4 -equivariant bifurcation in the full system. Also, one should not expect to find the secondary Hopf bifurcations as this is beyond the scope of the normal form.

The advantage of investigating symmetric configurations is that the solution structure of the resulting bifurcations is often affected or determined by the symmetry properties of the experimental set-up. Furthermore, it is relatively easy to analyse small deviations from the symmetric case by unfolding the bifurcation in the appropriate manner. A relevant extension to this work would be the characterisation of the codimension-two pitchfork-Hopf bifurcations that give rise to the Hopf instability curves. This should first be carried out for an isotropic single-plane ABB, before then proceeding to more complicated mechanical set-ups. However, even for the simplest case, it is likely that the inclusion of important damping effects could make the problem intractable [47]. Therefore, we prefer to proceed with a numerical bifurcation analysis in which further asymmetries of a two-plane ABB are considered.

3.3 Asymmetry of the supports

As discussed previously, rotating machines often run on bearings that have different stiffness and damping characteristics. This set-up usually occurs due to an asymmetric geometry of

the external support structure. The installation of a gas turbine below an aeroplane wing is one such example, and this configuration leads to bearings which have directionally dependent stiffnesses. In this section we shall investigate how these effects influence the stability of the balanced state.

We consider the model given by (3.5) and (3.6), which is written with respect to inertial coordinates, and includes the effect of support anisotropy. The steady state solutions are obtained by setting all the time derivatives to zero. If we also set the vibrational coordinates $\mathbf{X} = \mathbf{0}$, then we arrive at the following condition for the balanced steady state

$$\mathbf{f}_I + \sum_{k=1}^4 \mathbf{f}_{b_k} e^{i\alpha_k} = 0. \quad (3.37)$$

This equation simply states that the forces and moments acting on the rotor due to the imbalance and the balancing balls must be in equilibrium. The solution is physically unique and exists provided that the balls have a mass that is large enough to compensate for the imbalance. We denote the balanced state ball positions by α^* , these can be determined in closed form and were presented previously in (2.17).

Next, we shall use the continuation package AUTO [16] to compute bifurcation diagrams that show the regions of stability in various parameter planes. Because equations (3.5) and (3.6) are periodically forced by the imbalance, the time t only enters explicitly in the form of $\sin(\Omega t)$ and $\cos(\Omega t)$. This property enables the system to be rendered autonomous by appending the 2D nonlinear oscillator [16, §10.5]

$$\begin{aligned} \dot{s} &= s + \Omega c - s(s^2 + c^2), \\ \dot{c} &= -\Omega s + c - c(s^2 + c^2), \end{aligned} \quad (3.38)$$

and then substituting its asymptotically stable solution $s = \sin(\Omega t)$ and $c = \cos(\Omega t)$ back into the other equations. Hence, the fixed points of the isotropic rotating frame system of Chapter 2 can be identified as circular periodic orbits in the present fixed frame system. Consequently, as the balanced state is now viewed as a limit cycle, the stability boundaries will be formed by torus bifurcations as opposed to Hopf bifurcations. We also remind the reader that the stability results that will be presented are only valid *locally* and there most likely exists competing dynamics in much of the stable range.

For the remainder of this section we will consider an ABB model with the following parameters

$$\begin{aligned} M &= 1, & R_k &= R = 1, & k_{11} &= 1, \\ J_t &= 3.25, & J_p &= 0.5, & l_1 &= -l_2 = 3, & m_k &= m, & z_{1,2} &= -z_{3,4} = 2, \\ \tilde{c} &= 0.02 \quad \text{where} \quad \mathbf{C}_X = \tilde{c}\mathbf{K}_X \quad \mathbf{C}_Y = \tilde{c}\mathbf{K}_Y, & \text{and} \quad \bar{c}_b &\equiv \frac{c_b}{m} = 0.01. \end{aligned} \quad (3.39)$$

The first three constraints are simply rescalings which make the equations equivalent to the non-dimensionalised system of Section 2.1.4. The other parameters are also compatible with those that are given in (2.19) and (2.21).

3.3.1 Isotropic supports – $\mathbf{K}_X = \mathbf{K}_Y$ and $\mathbf{C}_X = \mathbf{C}_Y$

Gyroscopically uncoupled rotor – $k_{12} = c_{12} = 0$

When the stiffness and damping matrices have no off-diagonal terms, the rotor's translational and inclinational degrees of freedom are only coupled through the motion of the balancing balls. This situation can occur, for instance, in the case of a rigid rotor on two equal bearings with the centre of mass exactly at the midspan. First, we shall consider the isotropic set-up with stiffness matrices

$$\mathbf{K}_X = \mathbf{K}_Y = \begin{bmatrix} 1 & 0 \\ 0 & 9 \end{bmatrix}, \quad (3.40)$$

and recall from (3.39) that this implies $\mathbf{C}_X = \mathbf{C}_Y$. These stiffness and damping values are the same as those that were considered in Chapter 2. Thus, the approximate critical frequencies for the cylindrical and conical whirls are again given respectively by

$$\Omega_{\text{cyl}} = \sqrt{\frac{k_{11}}{M}} = 1, \quad \text{and} \quad \Omega_{\text{con}} = \sqrt{\frac{k_{22}}{J_t - J_p}} \simeq 1.81. \quad (3.41)$$

Figure 3.6(a) illustrates the stability diagram for the static imbalance case. The ball mass m is plotted against Ω , whilst we also vary the eccentricity so that $\frac{m}{M} = \frac{\varepsilon}{R}$. Thus, the imbalance scales with the mass of the balls and the balanced state α^* does not change value. Physically the condition $\frac{m}{M} = \frac{\varepsilon}{R}$ means that each ball has enough mass to compensate for the rotor eccentricity. Therefore, as there are a total of four balls, the ABB is at 25% of its balance correction limit. In addition, a logarithmic scale is used for the vertical axis so that a wide range of eccentricities can be considered. The main area of interest for applications occurs where there is a large connected stable region for small eccentricities and supercritical rotation speeds. The torus instability curve which bounds this region asymptotes towards $\Omega = \Omega_{\text{con}}$ as $\frac{\varepsilon}{R} = \frac{m}{M} \rightarrow 0$, hence, there is no stable region in the subcritical regime. By comparing panel (a) with Figure 2.7 we find that the results are identical. This match serves both as a check on the numerics and also demonstrates the validity of the approximation that was made at the beginning of this chapter in which the the small ball moment terms n_{ϕ_y} and $n_{-\phi_x}$ were ignored.

A similar plot is illustrated in Figure 3.6(b) for a dynamic imbalance, that is to say, an imbalance which has both an eccentricity $\varepsilon \neq 0$ and a misalignment $\chi \neq 0$. Here, we take

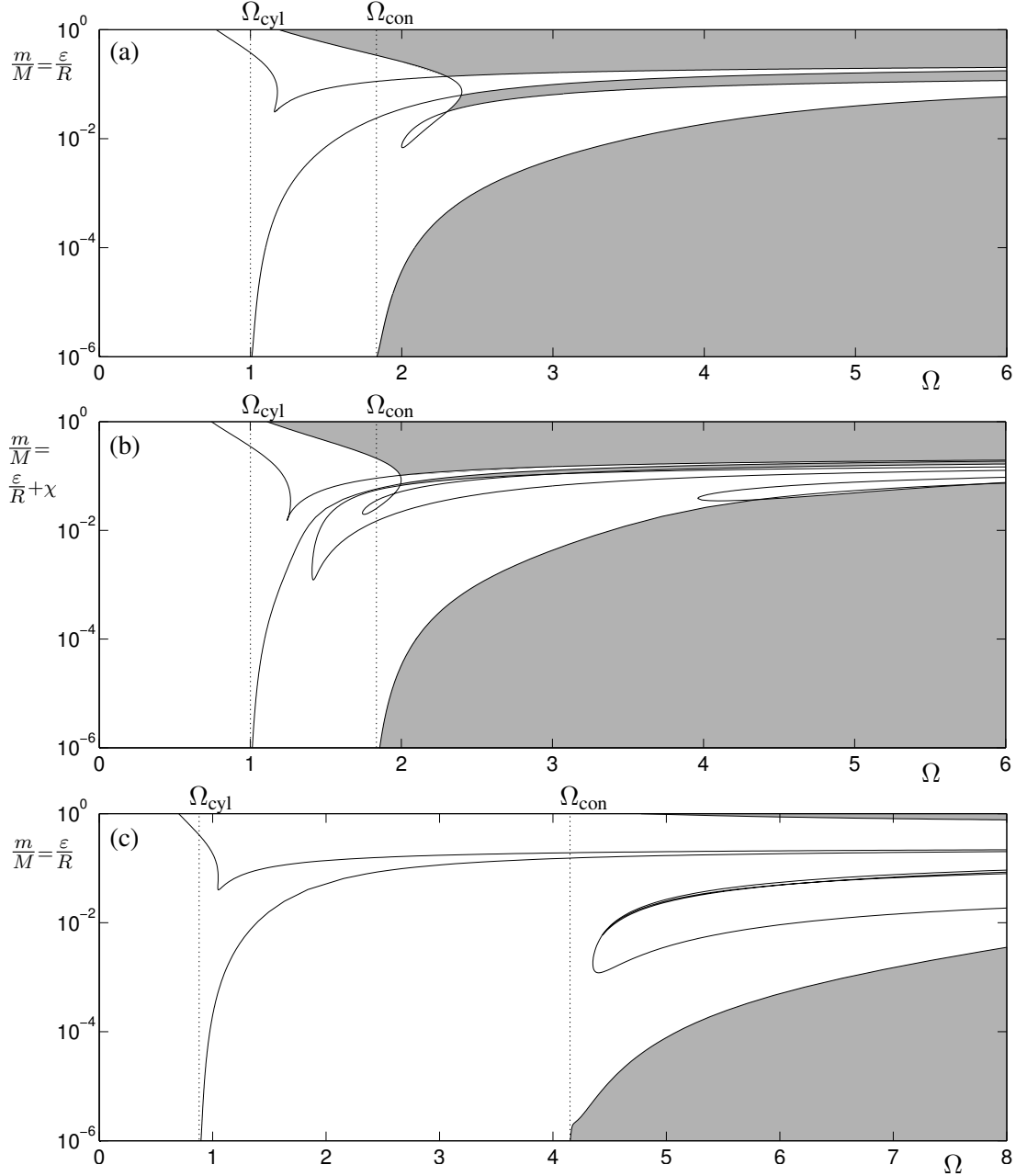


Figure 3.6. Stable regions of the balanced state (shaded) upon variation of m against Ω , whilst the imbalance is also varied so that the balanced state ball positions α^* remain constant. Panels (a) and (b) are for a static and dynamic imbalance respectively, in both cases the support parameters are gyroscopically uncoupled, see (3.40). Panel (c) is for a static imbalance case in which the support parameters are given by equation (3.42). These values correspond to a gyroscopically coupled set-up in which the centre of mass G is placed one quarter of the length along the shaft.

$\frac{m}{M} = \frac{\varepsilon}{R} + \chi$, $\frac{\varepsilon}{R} = \chi$ and constant phase $\beta = 1$, again the ABB is at $\approx 25\%$ of its balance correction limit. We find that the regions of stability remain largely unchanged, however, extra torus curves are now present. As discussed in Section 3.2, these arise because the introduction of a small misalignment breaks the symmetry between the two races.

Gyroscopically coupled rotor – $k_{12} \neq 0$ or $c_{12} \neq 0$

Next we consider the case in which the stiffness matrices remain isotropic, but where they also have off-diagonal terms. This would occur, for example, when the bearings have unequal stiffnesses or where the centre of mass is not at the midspan. Here, we take

$$\mathbf{K}_X = \mathbf{K}_Y = \begin{bmatrix} 1 & 3 \\ 3 & 45 \end{bmatrix}, \quad (3.42)$$

which corresponds to a set-up with $l_1 = 9$, $l_2 = 3$ in which the rotor's centre of mass G is three times further from one bearing than the other. This yields $\Omega_{\text{cyl}} \simeq 0.89$ and $\Omega_{\text{con}} \simeq 4.07$, for the critical speeds that are associated with the cylindrical and conical whirls respectively. Figure 3.6(c) shows the results for a static imbalance, and as in panels (a) and (b), bifurcation curves asymptote to the critical frequencies as the ball mass and eccentricity both tend to zero. The stable regions in the high eccentricity regimes have now almost disappeared, although more importantly, we find that the stable region for low eccentricities still exists, and has the same qualitative shape as before.

3.3.2 Anisotropic supports – $\mathbf{K}_X \neq \mathbf{K}_Y$ or $\mathbf{C}_X \neq \mathbf{C}_Y$

Finally, we consider the case of anisotropic supports. The main feature of this set-up is the splitting of circular whirls into distinct elliptical orbits that have different resonant frequencies. In addition, the rotor may undergo a backward whirling response in between the split resonances, that is to say, the whirl orbit may rotate in the opposite direction to the rotor's spin. For further details, see for example [24, §6], [64, §8.3] and [22, §6.2.5].

Here, we shall take the stiffness matrices given by

$$\mathbf{K}_X = \begin{bmatrix} 1 & 0 \\ 0 & 9 \end{bmatrix} \quad \text{and} \quad \mathbf{K}_Y = \begin{bmatrix} 5 & 0 \\ 0 & 45 \end{bmatrix}, \quad (3.43)$$

in which the stiffness in the Y -direction is 5 times greater than that in the X -direction. The approximate critical speeds have been computed numerically by determining the frequencies of the maximum response to imbalance. In this case, the translational and tilting critical frequencies are $\Omega_{\text{cyl},X} = 1$ and $\Omega_{\text{con},X} \simeq 1.65$ in the X -direction, and are $\Omega_{\text{cyl},Y} \simeq 2.24$ and $\Omega_{\text{con},Y} \simeq 3.79$ for the Y -direction.

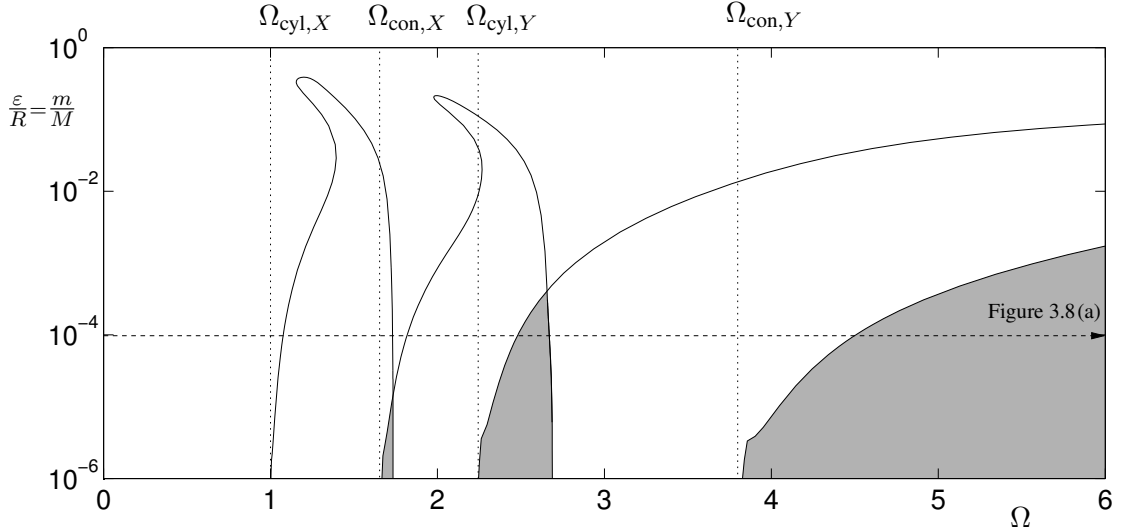


Figure 3.7. Stability chart for a set-up with anisotropic supports. Here the stiffness in the Y -direction is 5 times greater than that in the X -direction, see (3.43). A one parameter ‘brute force’ bifurcation diagram for the indicated section in Ω is displayed in Figure 3.8(a).

Figure 3.7 shows a stability chart for a static type imbalance c.f. Figure 3.6(a). The stable region for the high eccentricity regime no longer exists, however, new ‘wedge’ shaped stable regions now occur for low eccentricities when the speeds are in the vicinity of the rigid body resonances. The bifurcation curves again emanate at the critical frequencies and this type of behaviour is reminiscent of a ‘mode-locking’ phenomena in which coupled oscillators synchronize within specific parameter regions [46, §3]. The manner in which the stability regions of the ABB are influenced by the backward whirl orbits is a topic for future research. However, it is clear that there will be a complicated interdependence, this relationship is also investigated for a particular experimental set-up in Chapter 4.

Next, in Figure 3.8 we illustrate some ‘brute force’ bifurcation diagrams as Ω is varied, and $\frac{\varepsilon}{R} = \frac{m}{M} = 1 \times 10^{-4}$ is held constant. The results were obtained as follows: for each value of Ω we let the transients die away, and for the long term solution we plot the maximum value of \bar{A}_1 , the average rotor vibration level at points one unit length from the midspan. The initial conditions were such that the balls started at rest with respect to the rotor and on opposite sides of the race, that is to say, they do not add to the initial imbalance. Therefore, physically these results correspond to a set of experiments in which the balls are clamped during the run-up, and then released when a constant operating speed is reached.

Panel (a) is for a static imbalance and illustrates the results for the indicated one-parameter section through Figure 3.7. At certain intervals between resonances and for frequencies in excess of the highest critical speed the ABB (black curve) effectively eliminates rotor vibrations

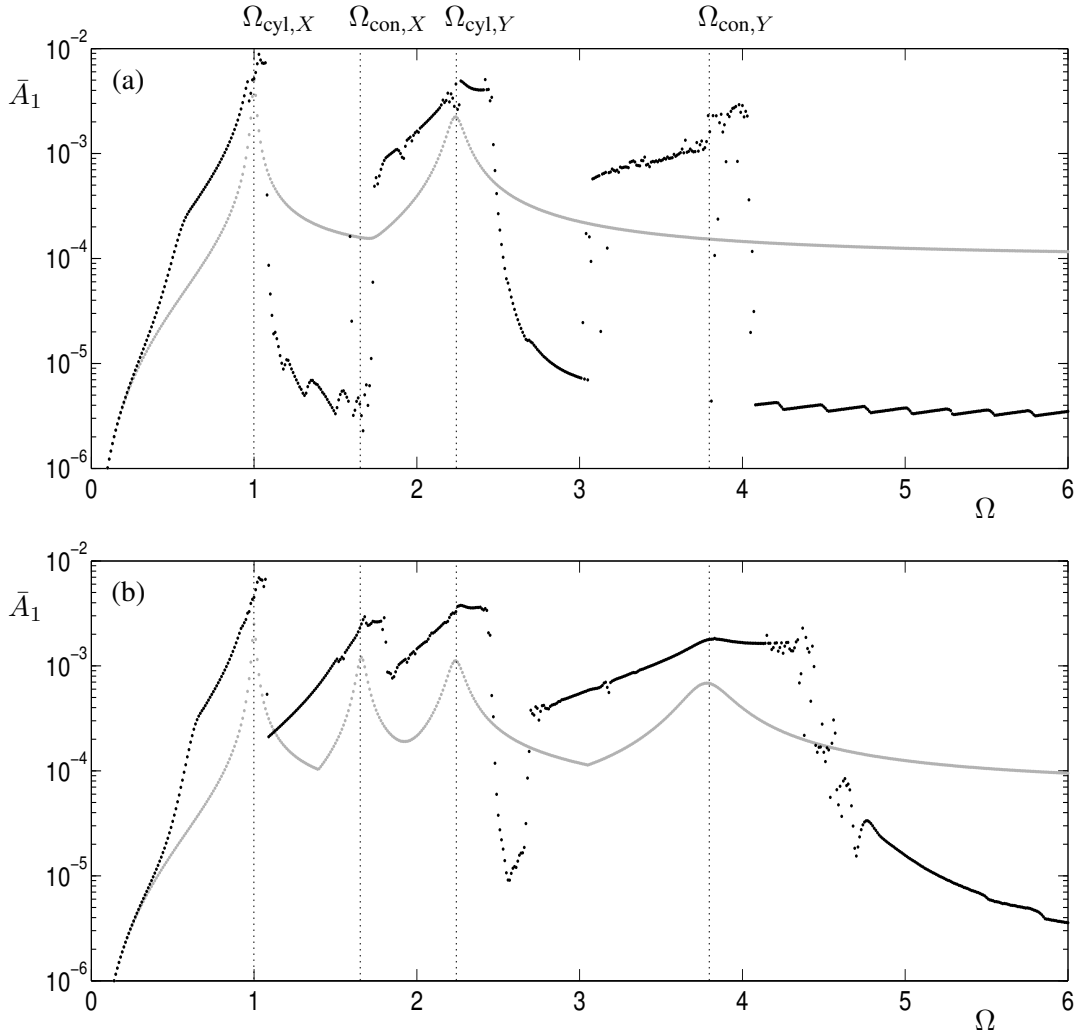


Figure 3.8. ‘Brute force’ bifurcation diagrams for a set-up with anisotropic supports. The rotor vibration \bar{A}_1 is plotted upon variation of Ω and the grey and black curves are for the plain rotor and ABB respectively. Panel (a) is for a static imbalance and illustrates the indicated one-parameter section through Figure 3.7; panel (b) is for a dynamic imbalance of a similar size.

whereas for the plain rotor (grey curve) $\bar{A}_1 \rightarrow \frac{\varepsilon}{R} = 1 \times 10^{-4}$ as $\Omega \rightarrow \infty$. By contrast, the ABB performs far worse than the plain rotor when in the vicinity of the critical speeds. We note that as $\chi = 0$ the conical resonances are not excited in the plain rotor, however, the balls still become unstable with respect to these modes. Also, the ABB seems to balance the rotor for a greater range of speeds than is predicted by the section through Figure 3.7. This discrepancy occurs because the symmetry of the initial conditions prevent the balls from destabilising as expected, c.f. the saddle-type behaviour of Figure 2.11(ii).

Therefore, we also present results for the case of a dynamic imbalance with $\frac{m}{M} = \frac{\varepsilon}{R} + \chi$, $\frac{\varepsilon}{R} = \chi$ and a constant phase $\beta = 1$. Here, there is a better agreement with the stability results of

Figure 3.7, and we find that the ABB still compensates for the imbalance in the far supercritical frequency range.

3.4 Asymmetry of the device

A real ABB device will always possess unavoidable errors that arise during the manufacturing process. For example, the race centre can never be made to coincide exactly with the rotation centre and the resulting error is called the *runway (or race) eccentricity*. The influence of imperfections in the race geometry was investigated in detail by Huang *et al.* [35] and Olsson [45]. Here it was shown that the vibrational amplitude of an ABB is bounded below by its runway eccentricity, therefore it is important that this error is minimised.

In this section we shall consider other such ABB asymmetries. In a practical two-plane balancing procedure, design constraints often dictate that the balancing planes are not chosen to be equally spaced from the midspan, therefore, we will investigate the case in which $z_{1,2} \neq z_{3,4}$. In addition we shall consider a set-up where one ball is heavier than the others.

For ease of analysis, we will restrict attention to the isotropic case with

$$\mathbf{K}_X = \mathbf{K}_Y = \mathbf{K} = \begin{bmatrix} 1 & 0 \\ 0 & 9 \end{bmatrix}. \quad (3.44)$$

Thus, we can use the autonomous rotating coordinates model that is given by (3.1) and (3.2). Also, unless otherwise stated, the values of the other parameters will again be given by (3.39). When the moments of inertia are such that $J_t > J_p$, the rotor is termed ‘long’ and there exists a critical speed Ω_{con} that is associated with the conical whirl. For the present case we have $J_t = 3.25$, $J_p = 0.5$ and so $\Omega_{\text{con}} \simeq 1.81$, see (3.41); these values correspond to a solid cylindrical rotor with a length of six times its radius.

Figure 3.9 shows various stability diagrams for a static type imbalance. As in Figure 3.6, the ball mass m is plotted against Ω , whilst we also scale the imbalance so that the balanced state α^* does not change value. Panel (a) serves as the control case and is the same (except for the aspect ratio) as that of Figure 3.6(a). By contrast, the results for a ‘disk’ type rotor in which $J_t < J_p$ are shown in panel (b). Here, the influence of the gyroscopic terms are such that the eigenfrequency corresponding to the conical whirl is always greater than the rotor speed Ω . This means that there is no conical critical speed Ω_{con} and thus no associated self-aligning process², hence the ABB is not stabilised with respect to conical motions. The method of direct separation of motion has been used by Sperling *et al.* [58] to derive this result and in

²Self-aligning is the phenomena whereby a rotor will tend to rotate about its principal axis of inertia at supercritical rotation speeds.

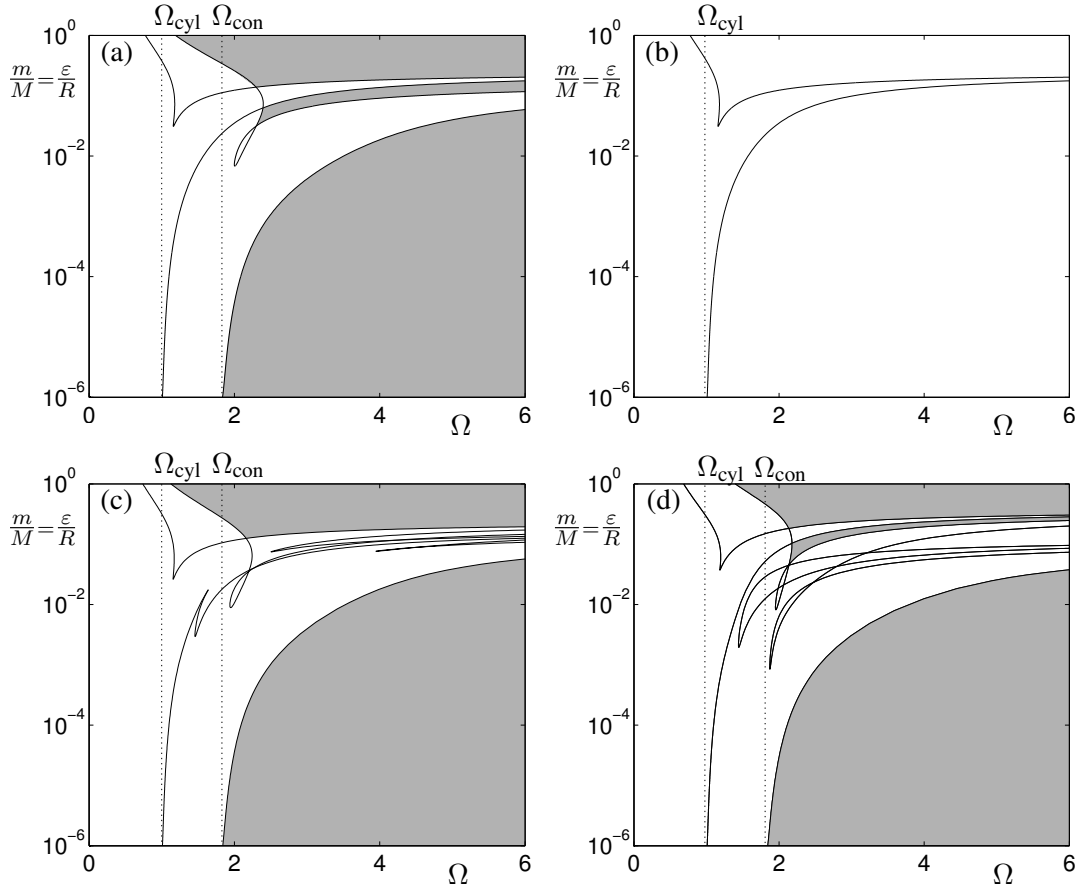


Figure 3.9. Bifurcation diagrams showing stable regions of the balanced state (shaded) in the case of a static imbalance. The mass of the balls m is varied against Ω , whilst $\frac{m}{M}$ is kept equal to $\frac{\varepsilon}{R}$ so that α^* remains constant. Panel (a) is a bifurcation diagram for a ‘long’ type rotor $J_p > J_t$ and panel (b) is for a ‘disk’ type rotor $J_p < J_t$. Similar diagrams for the ‘long’ type rotor are shown in (c) where one of the balls has a mass 20% greater than the others and in (d) where $z_{1,2} = 1$ and $z_{3,4} = 3$ so that the balancing planes are not equidistant from the midspan.

addition they discuss how it relates to Blekhman’s generalised self-balancing principle [5, §8]. From a practical viewpoint however, the prognosis for the autobalancing of ‘disk’ type rotors is not as bad as it may first seem. Because the conical mode has no associated critical speed, ‘disk’ rotors often need only to be balanced with respect to the static imbalance and a single plane ABB can be used to provide a partial imbalance compensation [57].

Next, we return to the ‘long’ type rotor case and investigate how the asymmetries of the ABB device can effect its stability. Panel (c) shows the situation where one of the balls has a mass that is 20% greater than the other balls. We see that the stable regions remain largely unchanged, however extra Hopf instability curves are present. These arise because the introduction of a different ball mass breaks the symmetry of the system. Another factor which must

be noted is that balls of different mass cannot counterbalance each other by settling to opposite sides of the race. Thus the overall capability of the ABB is reduced as unequal balls will inevitably add an imbalance to a rotor that is already well balanced [33]. Next the diagram in panel (d) shows the case where the balancing planes are not equally spaced from the midspan. We have taken $z_{1,2} = 1$ and $z_{3,4} = 3$, and again the main point to note is the robustness of the stable region for low eccentricities and supercritical rotation speeds.

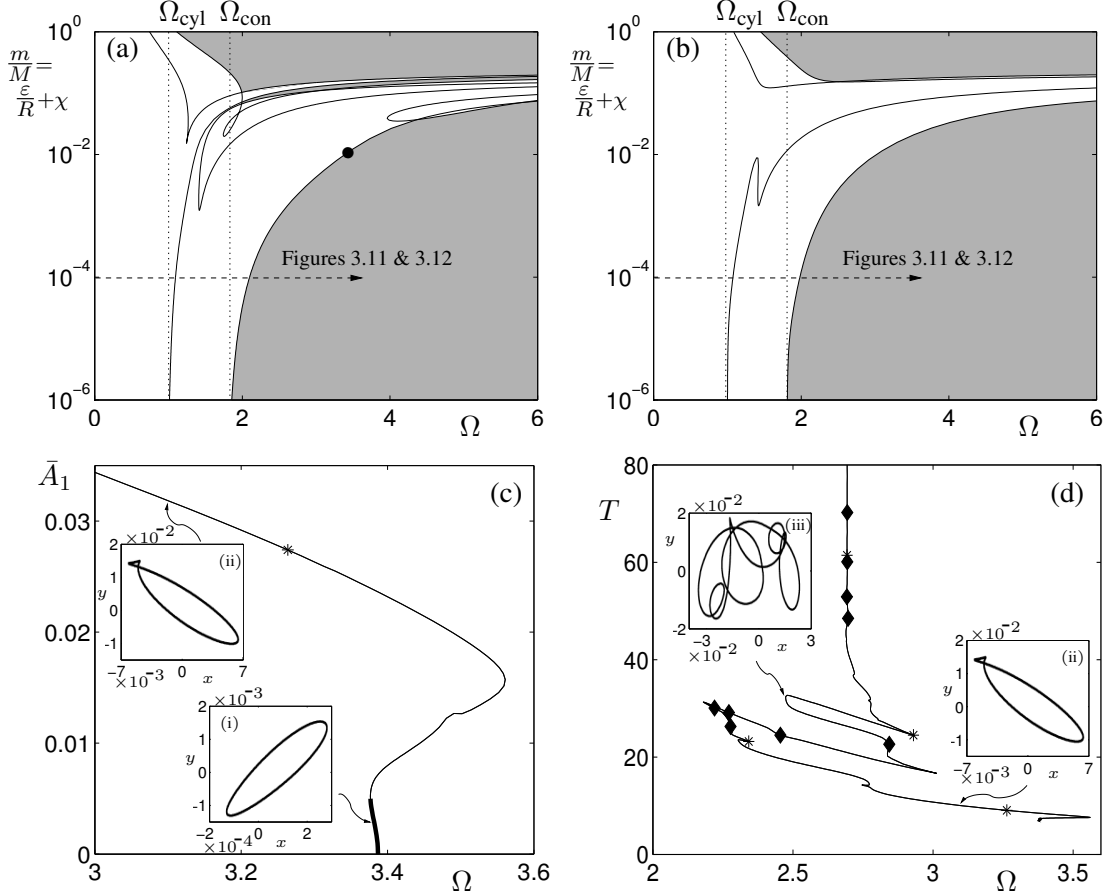


Figure 3.10. Bifurcation diagrams in the case of a ‘long’ rotor with a dynamic imbalance. Panel (a) is for a race damping value of $c_b = 0.01$ and panel (b) is for a higher race damping value of $c_b = 0.1$. The indicated one-parameter sweeps in Ω are illustrated in Figures 3.11 and 3.12. Panel (c) illustrates a continuation of the periodic orbit that emanates from the Hopf bifurcation marked by a (\bullet) in (a). Here, \bar{A}_1 is the vibration norm and the thick and thin curves represent stable and unstable limit cycles respectively. In panel (d) this branch is continued further in order to show its long-term behaviour, here T is the period of the orbit. Torus bifurcations are denoted by a (*) and period-doubling bifurcations by a (\blacklozenge). The insets illustrate the whirl orbits in the (rotating) x - y plane of the geometric centre C , at (i) $(\Omega, T) = (3.386, 7.081)$ (stable), (ii) $(\Omega, T) = (3.127, 9.856)$ (unstable) and (iii) $(\Omega, T) = (2.475, 32.453)$ (unstable).

We shall now return to the symmetric ABB setup and consider a rotor that suffers from a dynamic imbalance. Similar plots to those of Figure 3.9 are illustrated in Figure 3.10 for the dynamic imbalance case with $\frac{m}{M} = \frac{\varepsilon}{R} + \chi$, $\frac{\varepsilon}{R} = \chi$ and a constant phase $\beta = 1$. In panel (a) the race damping parameter is $c_b = 0.01$, whereas for panel (b) the race damping value has been increased to $c_b = 0.1$. As a consequence much of the complicated structure in the high eccentricity regime has been smoothed out.

The limit cycle which is born at the marked Hopf bifurcation for $c_b = 0.01$ and $m = 0.01$ is continued in panel (c), here the measure \bar{A} is the average rotor vibration at points one unit length from the midspan and is given by (2.24). We find that the Hopf bifurcation is supercritical and so there is a small region, as indicated by the bold curve, in which the limit cycle is stable. Therefore, in a controlled experiment we would expect, as Ω is decreased through this bifurcation, to see small oscillations of the balls about the balanced positions. The balls would then desynchronize with the rotor if Ω was reduced still further. For smaller values of the imbalance, say $\frac{\varepsilon}{R} + \chi = 1 \times 10^{-4}$, we have found that the Hopf bifurcation is subcritical and the transition to the desynchronized state would be immediate, see also Appendix A. The ability to follow the desynchronized limit cycles with continuation software is a topic for future work. Finally, panel (d) illustrates the long-term behaviour of the branch of limit cycles that was plotted in (c). We find that the solution ‘cuts-back’ on itself so that the period of the orbit does not increase monotonically. In addition, the insets show that the successive whirl orbits have an increasing number of loops. This behaviour, which was first described for a single plane ABB by Green *et al.* [28], is similar to the *zipper* bifurcation mechanism in which mode-locking periodic orbits merge with a homoclinic bifurcation at a resonance [31].

3.5 The effect of the rotor run-up

As yet, we have only considered set-ups in which the rotor speed Ω is assumed constant. However, if an ABB is to reach a stable region for balanced operation, then it must necessarily pass through at least one critical speed. Furthermore, the ABB usually increases the vibration levels of the rotor in the vicinity of a critical speed. In order to resolve this problem, various designs have been put forward in which the balls are locked in place during the rotor’s acceleration phase. For example, Thearle’s original 1932 ABB invention incorporated a hand operated clutch [60], and a constraint system was also utilised by Horvath *et al.* for a pendulum balancer [33]. Nevertheless, clamping mechanisms often detract from the simplicity of the design and can also fail to release the balls at the desired speeds. Thus, the majority of commercial ABBs do not have any locking mechanism for the balls.

This motivates a consideration of the ABB dynamics during the rotor run-up. In order to simplify the system, we will restrict attention to the isotropic case which has an imposed spin speed $\Omega = \Omega(t)$; the model for this set-up is given by (3.15).

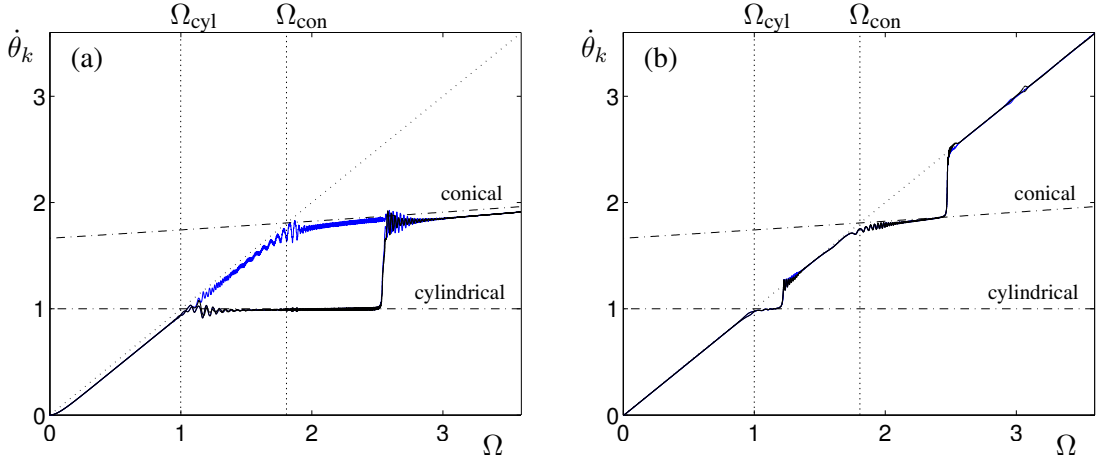


Figure 3.11. Diagram showing the ball speeds $\dot{\theta}_k$, $k = 1, \dots, 4$ against the rotor speed Ω for the dynamic imbalance case with $m = 1 \times 10^{-4}$. Black lines correspond to the top race balls ($\dot{\theta}_1$, $\dot{\theta}_2$) and blue lines correspond to those in the bottom race ($\dot{\theta}_3$, $\dot{\theta}_4$). Panel (a) is for a race damping value of $c_b = 0.01$ and panel (b) is for a value of $c_b = 0.1$, see Figures 3.10(a) and (b) for the corresponding sweeps in parameter space. The rotation speed increases from $\Omega = 0$ to $\Omega = 3.6$ with a constant acceleration over a time scale of $\Omega_{\text{cyl}} t = 6 \times 10^3$. Initial conditions are such that the rotor starts at rest in the undeflected position with the balls on opposite sides of the race.

In Figure 3.11 we plot the absolute ball speeds $\dot{\theta}_k$ against the rotor speed Ω for the sweeps with $\frac{m}{M} = 1 \times 10^{-4}$ that are shown in the dynamic imbalance stability charts of Figures 3.10(a) and (b). We slowly and uniformly increase the rotation speed over a time scale of $\Omega_{\text{cyl}} t = 6 \times 10^3$. For a rotor with $\Omega_{\text{cyl}} = 1000$ rpm, this corresponds to a constant acceleration phase that lasts approximately 1 minute with a final operating speed of $\Omega = 3600$ rpm.

Panel (a) illustrates the case for $c_b = 0.01$, here the race damping value is too low and the $\dot{\theta}_k$ curves lie below the line $\dot{\theta} = \Omega$. Thus we can infer that the balls lag the rotor and whirl backwards with respect to the race. Furthermore, as the rotor approaches and passes through its critical speeds, the balls tend to ‘stall’ and synchronize at a speed just below the rotor eigenfrequencies. The resulting vibration levels (not shown but similar to Figure 2.13(c)) are far higher than that of the rotor without the ABB. Therefore, this example serves to illustrate that even if the balanced state is locally stable, the conditions during the run-up can prevent the ABB from achieving balance. The stalling behaviour, which was first analysed for a single plane ABB by Ryzhik *et al.* [53], is similar to the Sommerfeld effect in which a rotating machine with an insufficiently powerful motor has difficulty in passing through the critical speeds.

Figure 3.11(b) is a plot of the corresponding results for the higher race damping value of $c_b = 0.1$. We find that the $\dot{\theta}_k$ again stall as the rotor passes through the critical speeds, however, as Ω is increased still further the balls resynchronize with the rotor and eventually this leads to balanced operation.

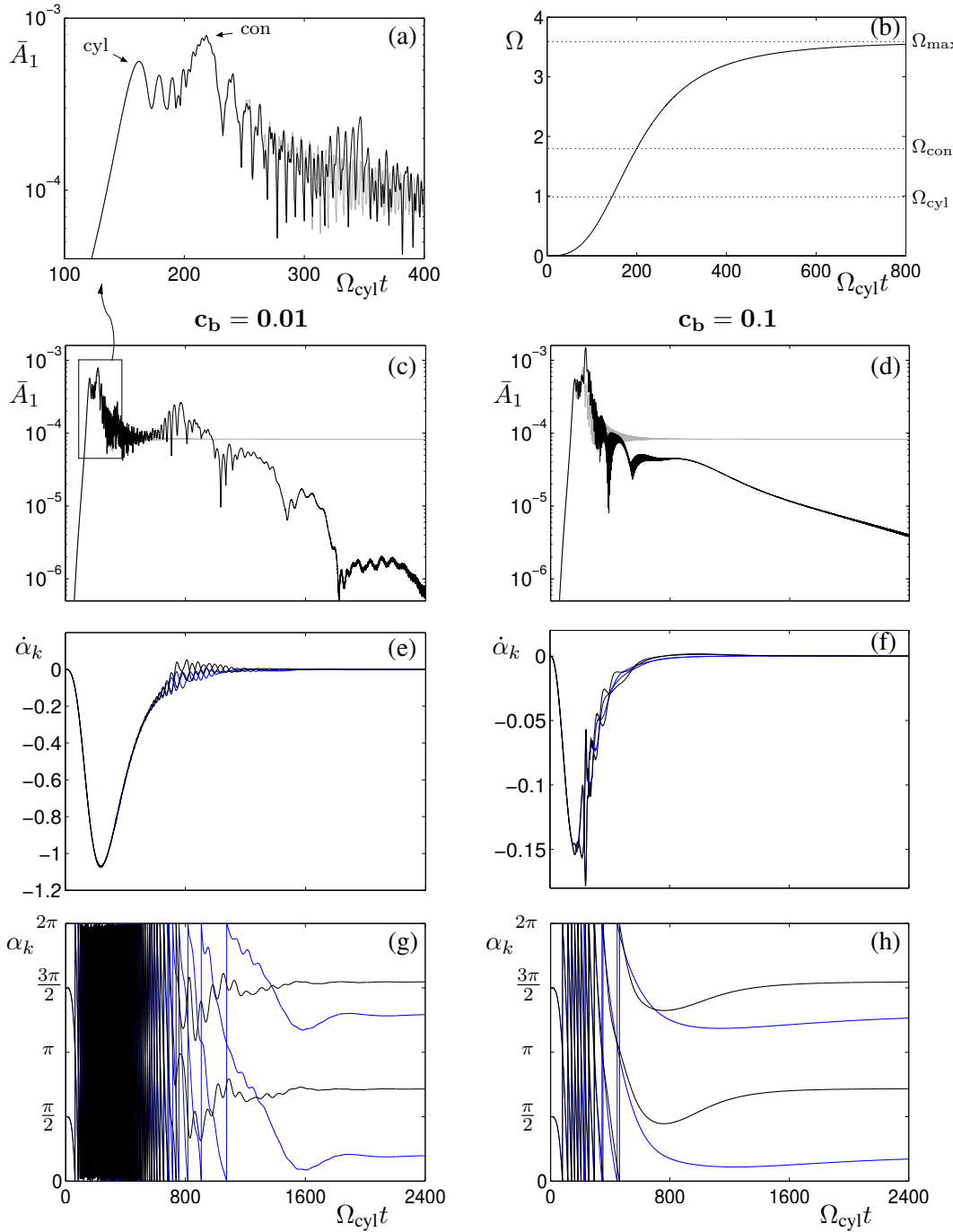


Figure 3.12. Simulations which include the effect of rotor run-up, the system parameters are the same as that for sweeps of Figure 3.11. Panel (b) shows the considered angular velocity profile. The case with $c_b = 0.01$ is displayed on the left column. Panel (a) shows the indicated detail of (c) in which the vibration levels \bar{A}_1 for the ABB (black curve) and the plain rotor (grey curve) are plotted. Panel (e) illustrates the ball speeds $\dot{\alpha}_k$ relative to the race and panel (g) displays the ball phases α_k . The corresponding plots for a higher race damping value of $c_b = 0.1$ are given in panels (d), (f) and (h). In both cases the initial conditions are again such that the rotor starts at rest in the undeflected position with the balls on opposite sides of the race.

The optimisation of the velocity profile for a particular application lies outside the scope of the present study, however, we shall now consider a more realistic rotor run-up that we can model by the Hill function

$$\Omega(\bar{t}) = \Omega_{\max} \frac{\bar{t}^n}{\bar{t}_{1/2}^n + \bar{t}^n} \quad \text{where} \quad \bar{t} = \Omega_{\text{cyl}} t. \quad (3.45)$$

This velocity profile is plotted in Figure 3.12(b) with the parameter values $(\Omega_{\max}, \bar{t}_{1/2}, n) = (3.6, 200, 3)$. For a set-up with $\Omega_{\text{cyl}} = 1000$ rpm, this profile would correspond to the rotor passing through the critical speeds during the 1 to 2 second time interval. We use this run-up to perform the same sweeps as for Figure 3.11, and the initial conditions are again such that the balls start on opposite sides of the race.

Figures 3.12 (a), (c), (e) and (g) illustrate the case for low race damping $c_b = 0.01$. Panel (a) shows a zoom of the run-up transient and we find that the rotor passes through its critical speeds by $\bar{t} = 250$. At this point the ball speeds lag behind Ω , however, they eventually catch up and begin to synchronize with the rotation speed, panel (e). Furthermore, they have phases which compensate for the rotor imbalance, that is to say, the ABB eventually achieves balanced operation, see panels (c) and (g). It is interesting that there is a period of increased vibrations as the balls approach the rotor speed. This occurs because the balls move from their positions on opposite sides of the race and begin to oscillate before they eventually synchronize with the rotor.

The resulting vibrations at around $\bar{t} \approx 800$ can be reduced if the race damping parameter is increased to say $c_b = 0.1$, see panels (d), (f) and (h). In this case the balls take less time to reach the speed of the rotor. However, during the rigid body resonance regime, the balls add to the imbalance and the vibration levels at the critical speeds are higher than that of the plain rotor. Nevertheless, and as mentioned previously, the lagging motions of the balls can be eliminated by using clamping mechanisms [60] or partitioned races [27].

3.6 Discussion

In this chapter, we have presented some simple models for a two-plane ABB. The equations were re-written in a more compact form, and effects such as support anisotropy and rotor acceleration were also included. We have shown that for a symmetric set-up the balanced state is born at a \mathcal{D}_4 -equivariant pitchfork bifurcation. Furthermore, the symmetry properties of this system have enabled us to demonstrate, that operation above both critical frequencies is a necessary condition for the stability of the balanced state.

Next, two-parameter bifurcation diagrams were obtained through the numerical continuation of Hopf and torus instability curves. We show that, if the machine has a small imbalance

and is operating above the rigid body resonances, then the addition of support and device asymmetries have little effect on the stable region of the balanced state. For example, in gas turbine and machine tool applications, typical eccentricities are $\frac{\varepsilon}{R} \approx 1 \times 10^{-5}$ [24, Appx. B]; and we find that with these values, the balanced state is stable for speeds just above the highest critical speed. However, for washing machine applications the imbalances are around $\frac{\varepsilon}{R} \approx 1 \times 10^{-2}$ [4], and the ABB remains unstable at frequencies that are far in excess of the critical speeds.

Finally, we considered the influence of the rotor run-up. Here, it was demonstrated that if the value of the race damping is too small, then the balls can ‘stall’ as the rotor passes through a critical speed. In addition, we have found that if the balls initially lag behind the rotor during a rapid run-up, then an increase in vibrations can occur as the balls desynchronize with each other before they reach the balanced state.

Even though the prospects for incorporating ABBs into high precision rotating machines seem promising, the stringent tolerances that are required for such applications present further difficulties with regards to implementation. For example, as the considered eccentricity range becomes smaller, the impact of ball positioning errors due to geometric defects and race friction become ever more important. In order to assess the significance of such effects, we will continue in the next chapter by describing an experimental study of a specific ABB.

Chapter 4

Experimental Study

In this chapter we describe an experimental study of a specific ABB system. Through this empirical investigation we aim both to validate some of the results of the previous chapters, and also, to assess the importance of effects that have so far been omitted from the mathematical model.

As discussed in the introductory review of Section 1.4.2, most recent experimental auto-balancing research has focused on systems that have been tailored towards use in specific applications. For example, the effects of rolling friction between the race and the balancing balls were observed in optical disk drive systems by Chao *et al.* [10], van de Wouw *et al.* [62] and Yang *et al.* [65]. Although these results are promising, the body of experimental evidence for the effective operation of an ABB device remains scarce. In particular, data for the performance of the ABB as it passes through multiple resonances is still unavailable. In light of the absence of this empirical data, we have set out to design a lightweight, low bearing stiffness, table top rig. The set-up has been specifically designed to possess both cylindrical and conical rigid body modes, and also, to allow the performance of the ball balancer to be safely observed up to sufficiently high rotational frequencies.

The rest of this chapter is organised as follows. In Section 4.1 we describe the overall experimental set-up and we also discuss the design of the automatic balancer. The rotor parameters are estimated in Section 4.2 and further details on the measurement of the mass imbalance are given in Appendix B. In Section 4.3 the response of the plain rotor (i.e. without balls in the ABB disk) is investigated, and in Appendix C we show how these measurements are used to estimate the values of the support parameters. Next, in Section 4.4 we present results of ABB frequency responses for a range of different imbalances. Finally, in Section 4.5 we compare these experimental results with numerical simulations that are generated with models from the previous chapters.

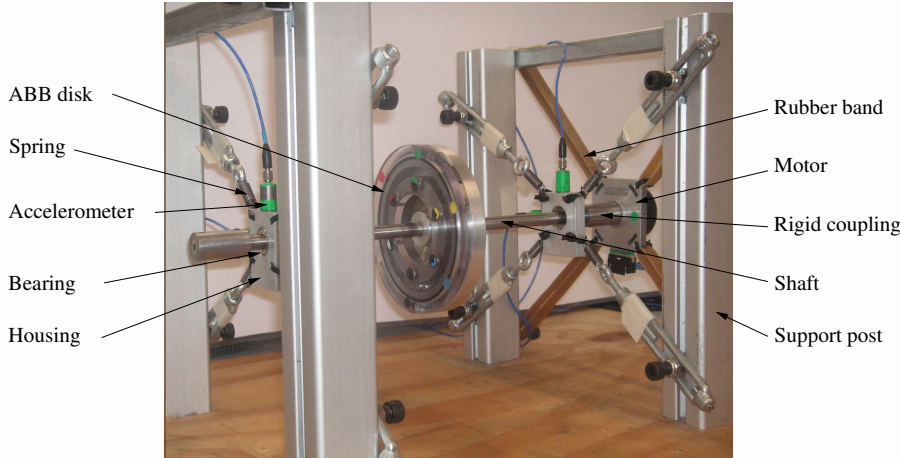


Figure 4.1. Photograph of the experimental rig.

4.1 Description of the experimental setup

A photograph of the experimental test rig is shown in Figure 4.1. The rig comprises of an ABB disk that is positioned midway along a horizontal silver steel shaft of 10 mm diameter. This shaft is mounted at each end onto nominally identical single-row ball bearings, which are fitted into housings and attached to the supports through a set of springs. The support structure consists of four posts that are reinforced with lateral beams and fixed to a wooden base board. Next, a motor that is suspended by rubber bands drives the shaft via a rigid coupling and the speed of this motor is controlled through a dSpace DS1104 digital signal processing board [17]. Finally, the lateral vibrations are measured with accelerometers that are attached to the bearing housings and the resulting accelerations are converted into displacements with a simple Matlab routine.

Before we move on to a description of the ABB disk, we shall first explain some of the design choices that led to this particular realisation of the experimental set-up. The requirement that the rotor should be capable of safely operating at highly supercritical rotation speeds made it necessary that the rig should be both lightweight and also have relatively low critical vibration frequencies. Therefore, we envisaged a rotor with a mass of around 1-2 kg and with critical frequencies somewhere in the 1000-3000 rpm range. By using the lower bounds of these values in the expression for the first critical frequency $\Omega_1 = \sqrt{k_{11}/M}$, we can gain a rough initial estimate of $k_{11} \approx 10,000 \text{ N m}^{-1}$ for the desired lateral stiffness. This value is more than an order of magnitude less than the corresponding stiffness coefficient of $k = 3.436 \times 10^5 \text{ N m}^{-1}$ for the system studied by Green *et al.* [27] in which the bearing housings were bolted to an external frame. In light of this observation, our housings are not rigidly fixed to ground but are

instead supported by springs that give an appropriate stiffness. As a consequence the stiffness coefficient of our system will be more comparable to that of the optical disk drive set-ups studied in [10, 62, 65].

Having established this ‘soft’ bearing support structure, the connection between the motor and shaft was required to be as rigid as possible in order that we could avoid any undesirable vibrational modes that a flexible coupling may have induced. With a rigid connection, the motor becomes an integral part of the rotor and therefore it must also be lightweight. The motor that we have chosen for our rig is an ebm-papst ‘Variodrive’ VD-3-35.06 [19], this model is a three phase brushless design that has a mass of 120 g and a nominal top speed of 6200 rpm. The motor is then suspended from rubber bands so that the lateral load on its spindle is reduced. The bands also allow the generated torque to react against the frame so that the motor can drive the rotor.

In order to determine the system’s response, the vibrations at the bearing housings are measured with accelerometers. An alternative would be to use a laser Doppler vibrometer, which would have the advantage of being able to measure the vibration level directly at the ABB disk. However, as the rig operates in the rigid regime, the vibration level at the disk can be inferred from those at the housings and the accelerometers are suitable for this purpose. Finally, in order to allow the efficient production of high resolution frequency response curves, a dSpace ControlDesk system was used to automate the experimental runs and data acquisition procedures.



Figure 4.2. Photograph of the automatic balancer. Note, in this picture the balls are larger than those used in the actual experiments cf. Figure 4.6.

The automatic balancer, which is shown in Figure 4.2, consists of an aluminium hub into which a hardened steel ball race of 50 mm outer radius has been fitted. Steel balls of 4.76 mm diameter and 0.44 g mass are used as the balancing masses. The balls can be viewed through a perspex cover that is attached to the balancer with a circular array of screws. A light coating

of oil, which provides damping for the motion of the balls, is applied to the race and a rubber seal is used to prevent any oil from escaping. The balance of the disk can be adjusted, either by adding washers to the screws, or by changing the angular position of adjustable outer masses that can be rotated around a groove in the hub and fixed in place with grub screws.

At this point, let us highlight some considerations relating to the design of the ABB disk. The steel ball race comes from the outer part of a single row, deep groove, SKF 16013 ‘explorer’ bearing. According to the company literature [55], these bearings are made from a high grade steel that is cleaner and more homogeneous than that which is used in their standard bearings. Also, the steel has been hardened through a heat treatment procedure and the finish on the contact surface has also been improved. It is hoped that these features reduce the rolling friction between the balls and the race and thereby improve the performance of the ABB [10, 62, 65]. In addition, the deep groove in the race prevents the balls from rattling between the hub and the perspex cover, as during operation a centrifugal force acts on the balls so that they are confined to lie in the deepest part of the channel. Further discussion of the ABB design, including details about its geometrical accuracy, will be given later at the end of the next section. First, let us turn to the parameter estimation of the basic rotor.

4.2 Estimating the rotor parameters

During the design stage, a model of the plain rotor was constructed using the finite element method (FEM) rotordynamics package DynRot [23]. This model, which is shown in Figure 4.3, was used to predict the rotor’s critical speeds and also to determine its response to imbalance. As each element in the DynRot package is modelled with deformable Timoshenko beams [24, §5.3], we were able to estimate that the first flexible critical speed (commonly called the skipping rope mode, due to its shape) would occur at ≈ 9000 rpm. Hence we may assume that the rotor is in the rigid regime for our operating speeds which are less than 5500 rpm. Once the rig was built, experiments were conducted that enabled the FEM model to be updated and improved.

Some separate tests were performed in order to estimate the rotor parameters and a summary of these values is given in Table 4.1. The rotor was weighed on standard digital scales which were accurate to the nearest gram. However, it is not possible to measure the mass M to that precision as some parts of the rig, such as the power supply wires and springs, lie only partially within the vibratory structure, and so it is difficult to determine the inertial contributions from these components. The mass of the balls m was measured to the nearest 10 mg with some high precision digital scales and the radial distance to the balls R was determined with a micrometre and vernier callipers. Note that, as R is the distance from the race centre to the

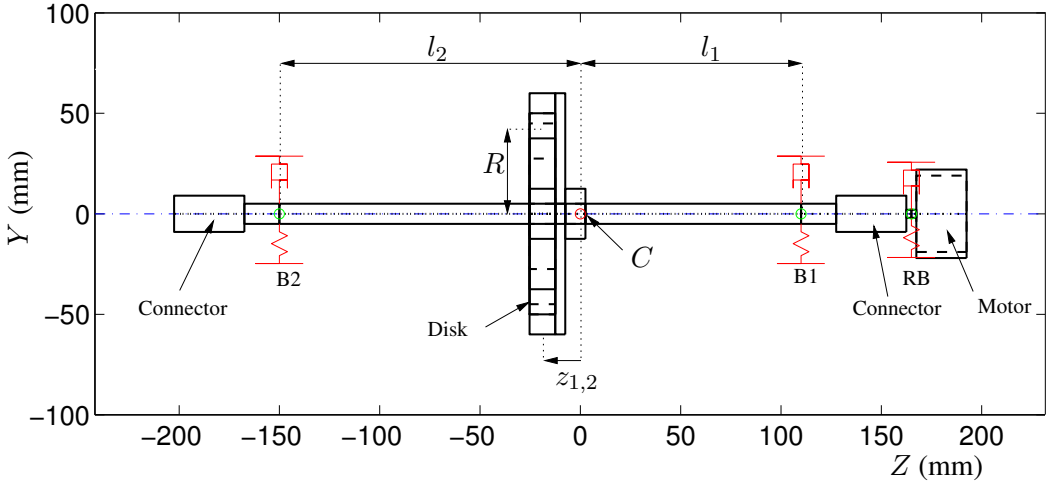


Figure 4.3. Finite element model of the rotor cf. Figure 4.1. Here B1, B2 and RB represent the axial positions of the bearings and rubber bands respectively and the point C is the centre of rotation in the plane of the centre of mass. The lengths R and $z_{1,2}$ denote the radial and axial distances from C to the balancing balls, and l_1 and l_2 are the axial distances from C to the respective bearings.

Table 4.1. Estimated rotor parameters.

Parameter	Dimensional	Non-dimensional
Rotor mass, M	$1.28 \pm 0.005 \text{ kg}$	$\equiv 1$
Radial distance from C to the balls, R	$42.8 \pm 0.05 \text{ mm}$	$\equiv 1$
Ball mass, m	$0.44 \pm 0.005 \text{ g}$	$3.44\text{e-}4$
Transverse moment of inertia, J_t	$(1.38 \pm 0.05) \times 10^{-2} \text{ kg m}^2$	5.89
Polar moment of inertia, J_p	$(1.24 \pm 0.05) \times 10^{-3} \text{ kg m}^2$	0.53
Axial distance from C to the balls, $z_{1,2}$	$-20 \pm 5 \text{ mm}$	-0.47
Axial distance from C to bearing B1, l_1	$110 \pm 5 \text{ mm}$	2.57
Axial distance from C to bearing B2, l_2	$150 \pm 5 \text{ mm}$	3.50

centre of mass of the balls it is calculated as $R = R_s - r$, where R_s is the radius to the race surface and r is the ball radius.

Next, the moments of inertia were estimated through calculation and verified with measurements of the period of free oscillations when individual components such as the balancing disk and motor were placed on a trifilar suspension [6]. Clearly, as the motor is rigidly connected to the shaft, its contribution to the inertial parameters must also be included. In the original design there was a motor at each end, however one motor was removed so that spindle-connector misalignment problems could be avoided. Therefore, the mass of the single motor at the B1 bearing end of the shaft draws the centre of mass in that direction, see Figure 4.3. Hence, the

Table 4.2. Estimated imbalance parameters. The number of washers removed from the pre-balanced disk is denoted by n_w , the dimensional and non-dimensional eccentricities are ε and ε/R respectively, χ is the misalignment and β is the phase between the misalignment and the eccentricity, see Appendix B for further details.

n_w	Imbalance [g mm]	ε [mm], (ε/R)	χ [rads]	β [degs]
0	5.9	0 (0)	6.1e-5	n/a
1	12.4	1.0e-2 (2.3e-4)	4.8e-5	282°
2	24.8	1.9e-2 (4.5e-4)	5.1e-5	247°
3	37.2	2.9e-2 (6.8e-4)	6.8e-5	224°
4	49.6	3.9e-2 (9.0e-4)	9.2e-5	211°

axial distance l_1 from bearing B1 to the centre of rotation C is less than the corresponding distance l_2 , for bearing B2. As a consequence, the ABB disk is not quite in the plane of C even though it is mounted at the bearing midspan. We also note that the errors in the measurements of the axial lengths arise mainly due to the difficulty in determining the precise axial plane of C .

The inherent rotor imbalance was identified with the ‘four-run no phase’ balancing procedure [63, §9], which is more reliable than alternative single-plane procedures in situations where the vibrations are not solely due to the rotor imbalance. The balancing operation was performed on our set-up at a supercritical rotation speed of 4000 rpm. A washer was used as the trial mass and this was fixed to alternate screws during the trial runs. The mass distribution of the rotor was then altered by making fine adjustments to the position of the outer masses. By the end of the process the rotor’s imbalance was reduced to less than 6 g mm, for further details we refer the reader to Appendix B. The remaining imbalance was mainly of the couple type and so could not be eliminated through a single-plane balancing process. In the following set of experiments we shall apply a known imbalance by removing washers from the screws. The washers have a mass of 0.38 ± 0.01 g and the screw radius is 32.5 mm, so each washer provides an imbalance of 12.4 ± 0.5 g mm. The eccentricity and misalignment parameters for the rotor with different amounts of washers removed are given in Table 4.2.

Finally, let us turn to a discussion of the geometrical accuracy of the ABB disk. Recall from Section 3.4 that the runway eccentricity is the distance between the geometric centre of the race and the axis of rotation. In order to minimise this error, the race recess and the bore of the hub were machined without removing the aluminium piece from the lathe. The steel race was then inserted into the hub using an interference fit so that the centres of the bore and the race would be as close to each other as possible. Once the ABB was mounted onto the shaft and carried by the bearings, the runway eccentricity was measured using a G308 Mercer

dial test indicator to be $5 \pm 1 \mu\text{m}$. From Table 4.2, we find that this distance is about half the mass eccentricity value that arises from a 1-washer imbalance. Thus, the runway eccentricity is small but not negligible as compared to the imbalance eccentricities, and it will therefore be a possible source of experimental error. We mention that the circularity of the race was also measured with the dial test indicator and no additional defects such as runway ellipticity were detected.

4.3 The plain rotor response and support parameter estimation

The frequency response of the plain rotor (i.e. with the balls removed from the ABB disk) can be used to give a good estimate of the support parameter values. In addition, the results of these tests provide a control against which the performance of the ABB can be compared. Figure 4.4(a) shows the measured vibration levels of the plain rotor with an applied imbalance of 3 washers. The red curve corresponds to the rotor run-up while the blue curve corresponds to the rotor run-down.

During the experimental procedure the dSpace ControlDesk is used to set the motor to a desired frequency which is maintained for 0.25 seconds in order to allow any transient behaviour to die down. Over the next 0.25 second interval, the X and Y vibrations at both bearing housings are measured with accelerometers, and these accelerations are converted into displacements with a simple Matlab program. Finally, the speed of the motor is incremented by approximately 10 rpm and the process is repeated.

The vibration measure is taken to be the average of the maximum displacements at each bearing, which is given by

$$\bar{A}_{\max} = \frac{1}{2} \left(\max \sqrt{(X_1^2 + Y_1^2)} + \max \sqrt{(X_2^2 + Y_2^2)} \right). \quad (4.1)$$

The four resonance peaks that are present in the 1400-2400 rpm speed region arise from the excitation of the rigid body modes by the rotor imbalance and the corresponding whirl orbits at these resonances are shown in panels (b) to (e).

If the bearing stiffnesses were isotropic then we would expect the static imbalance to excite only one cylindrical whirl which would then be circular. (Recall in relation to whirl orbits, cylindrical denotes that the displacements at the bearings are in phase, whilst conical denotes that the displacements at the bearings are out of phase). Here, because the support stiffness is not perfectly isotropic, this circular cylindrical whirl has been split into two elliptical cylindrical whirls. The first was measured to occur at $\Omega_{\text{cyl},Y} = 1415$ rpm (b) and to have a major axis in the Y direction. The second whirl occurs at $\Omega_{\text{cyl},X} = 1675$ rpm (c) and has its major axis along the X direction. For some frequency range in between these two critical speeds

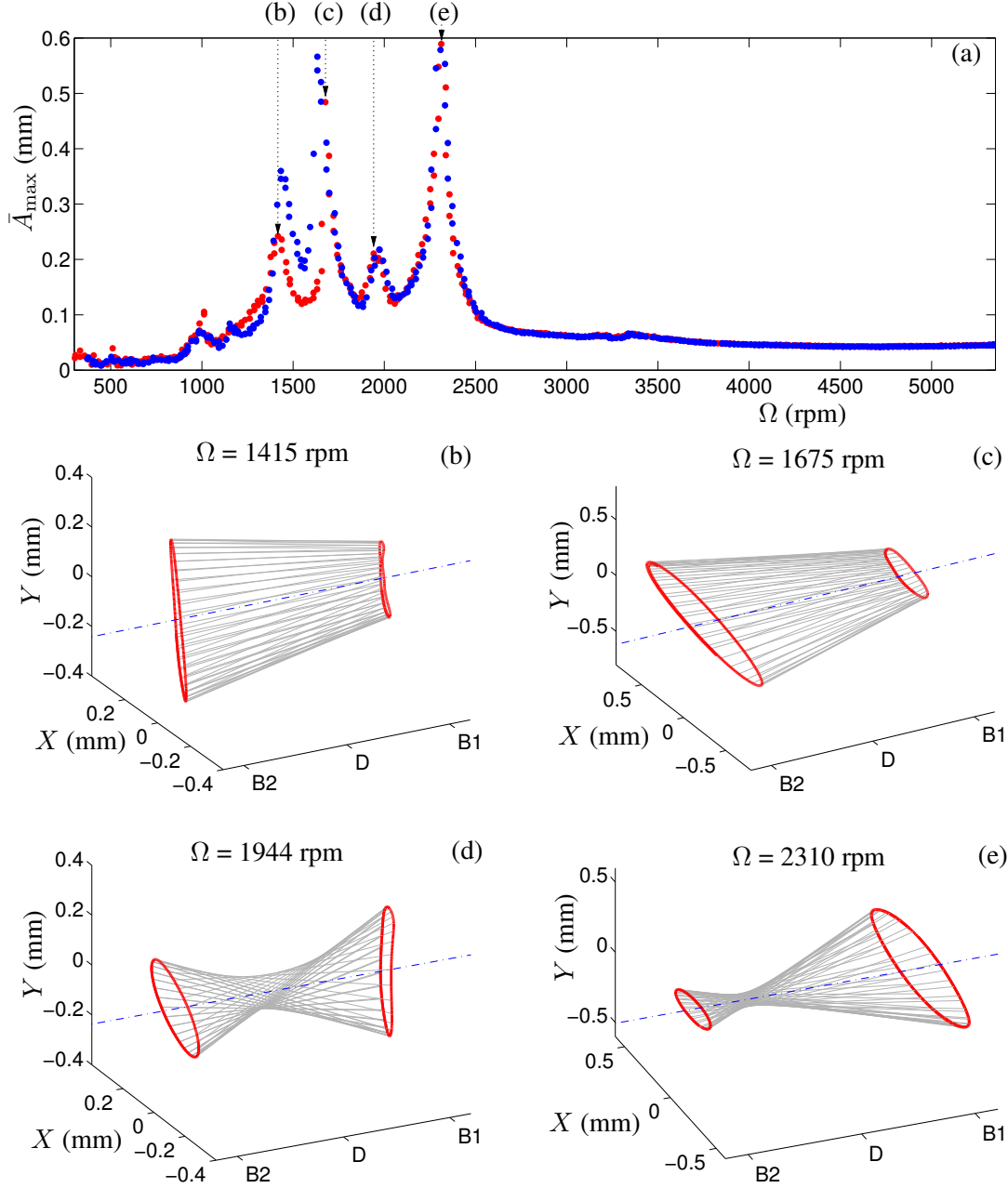


Figure 4.4. Measured response of the plain rotor with a 3-washer imbalance. Panel (a) shows the lateral vibration level \bar{A}_{\max} upon variation of the rotor speed Ω for both the rotor run-up (red points) and run down (blue points). The measured whirl orbits at the data points indicated are illustrated in panels (b) to (e). Here B_1 , B_2 and D denote the axial positions of the bearings and balancing disk respectively. Note that the vibration levels along the length of the shaft have been inferred from those at the bearings by assuming that the rotor is rigid.

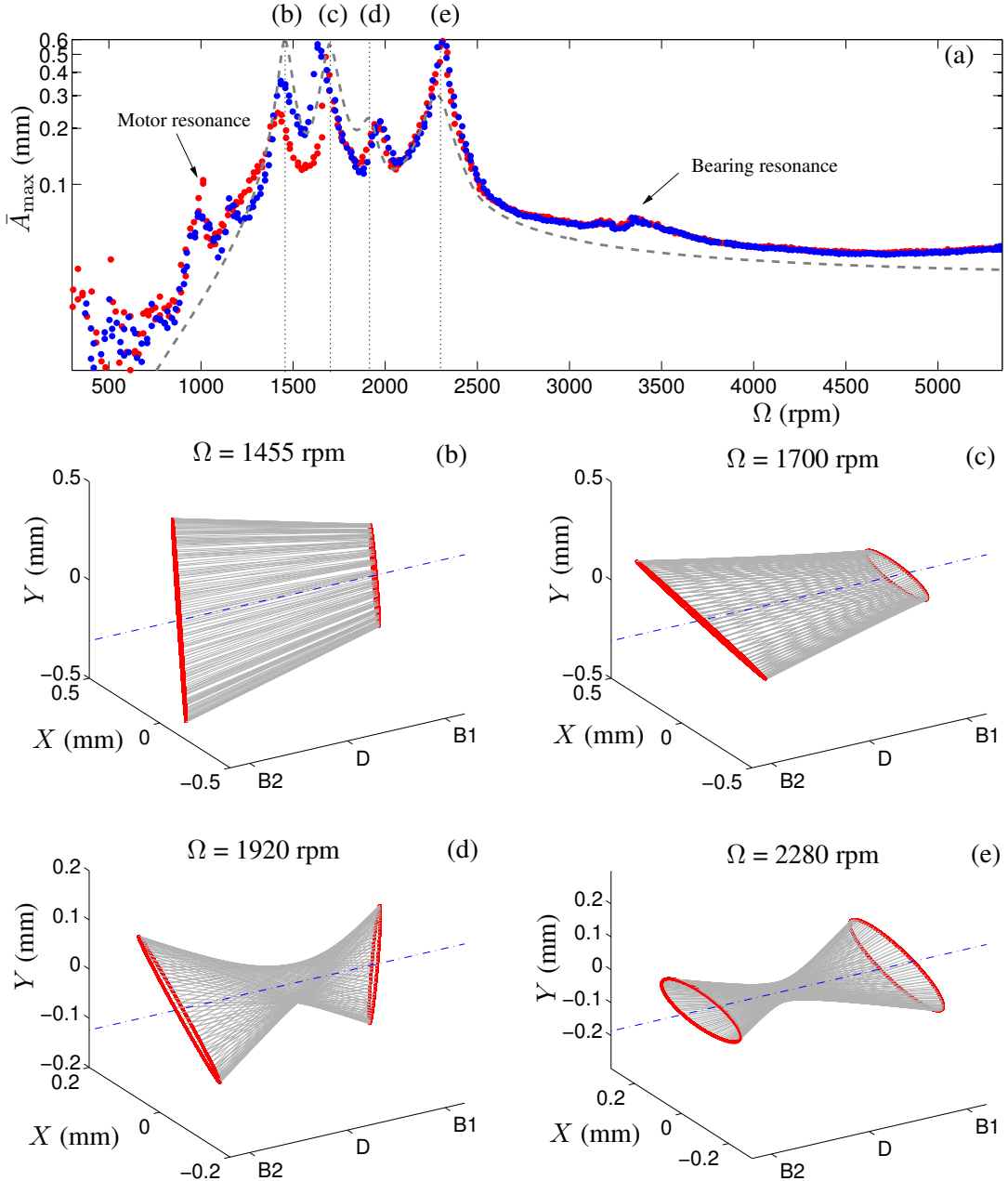


Figure 4.5. Comparison of the measured response with theory for the plain rotor with a 3-washer imbalance. Panel (a) shows the log scaled lateral vibration level \bar{A}_{\max} upon variation of the rotor speed Ω for the rotor run-up (red points), run down (blue points) and the numerical approximation (grey dashed line). The simulated whirl shapes at the resonance peaks are illustrated in panels (b) to (e), compare with the experimental results of Figure 4.4.

Table 4.3. Estimated rotor support parameters, see Appendix C for details.

Parameter	Dimensional	Non-dimensional
Bearing stiffness in the X direction, k_{1X} and k_{2X}	$10,750 \text{ N m}^{-1}$	$\equiv 1$
Bearing stiffness in the Y direction, k_{1Y} and k_{2Y}	$7,900 \text{ N m}^{-1}$	0.735
Ratio between the stiffness and damping matrices, \tilde{c}	2.5e-4 s	4.58e-2

the rotor undergoes a backwards whirling motion whereby the direction of the whirl orbit is opposite to that of the rotor's spin. The next two resonances arise from conical whirls that are excited by the couple imbalance. As with the cylindrical resonances, the presence of stiffness anisotropy causes the split of a single circular conical whirl into two elliptical conical whirls that were measured to occur at $\Omega_{\text{con},Y} = 1944 \text{ rpm}$ (d) and $\Omega_{\text{con},X} = 2310 \text{ rpm}$ (e); again, the rotor undergoes a backwards conical whirl motion for a range of speeds in between these two resonances.

We note here that the support anisotropy does not arise from differences in the individual spring stiffnesses, but comes from the off-square manner in which the springs are attached from the bearing housings to the support structure, see Figure 4.1. Also, no effort has been made in order to reduce the anisotropy as we do not expect it to hinder the overall performance of the ABB. In fact, we hope that this property of the supports will provide extra interest especially in view of possible industrial applications where perfect isotropy of rotor supports is rarely achieved in practice.

A small amount of hysteresis can be seen in the frequency response curve around the 1400–1700 rpm range in Figure 4.4(a). In order to obtain enough data points to capture the resonance peaks during the experimental runs, the rotor is held at the critical speeds for longer than would otherwise be necessary. Hence, the bearings can become slightly misaligned and change character as a relatively high degree of energy is dissipated through them. It is this effect that we believe to be the main cause of the discrepancy between the red and blue response curves; for runs with a smaller imbalance or where there is a more rapid sweep through the resonances, the hysteresis effect is much less noticeable.

As mentioned above, the frequency response curve of the plain rotor is used to infer the values of the support parameters. Specifically, the critical speeds of the cylindrical resonances are used to determine the stiffnesses in the X and Y directions whilst the heights and widths of the peaks are used to estimate the amount of support damping. By an appropriate choice of these three parameters, which are given in Table 4.3, we were able to find a good fit between the numerical response curve and the data, see Appendix C for further details.

An appropriate model for the plain rotor set-up is given by equation (3.5) with the contribution from the balls ignored, see Section 3.1.2. Recall that this system is written in terms of the space frame coordinates and includes the effect of support anisotropy but not the effect of the rotor acceleration. The run-up can be neglected because during the experimental tests the rotation speed was maintained at each frequency, and this allowed the transients to die away before the data was recorded. Taking the relevant parameter values from Tables 4.1-4.3 we have performed a direct numerical simulation for the set-up with a 3-washer imbalance. The numerical results were obtained using the same procedure that was carried out in the experiments; namely for each value of Ω the transients are allowed to die away, and for the long term solution we plot the average value \bar{A}_{\max} of the maximum displacements at each bearing.

The comparison between this simulation (dashed grey curve) and the previously discussed experimental data (red and blue curves) is shown in Figure 4.5(a). We find a good agreement for most of the curve characteristics, especially for the positions and shapes of the rigid body resonances. However, there is also a slight underestimation of the vibration levels in the 4000-5000 rpm speed range; this may indicate that the applied imbalance is larger than that we have calculated, or that other causes of vibration such as shaft bow and higher order modes are present. Nevertheless, this discrepancy is relatively small ($\approx 15\%$) and it is clear that the applied mass imbalance is the dominant cause of vibrations in the supercritical regime. Also, by plotting the vibration measure \bar{A}_{\max} on the log scale we are able to identify at least two additional rotor resonances. We believe that the resonance at 1000 rpm is due to a torsional motor vibration and that the peak at around 3300 rpm is caused by a non-linear resonance of bearing B2.

Figures 4.5(b) through to (e) display the simulated whirl orbits at the rigid body resonance peaks. A comparison with the experimental plots of Figure 4.4 indicates both a good qualitative and quantitative agreement. We note that some of the elliptical orbits of the numerically generated whirls appear to be more elongated than those of the measured responses. However, this difference only arises because of the difficulty in matching the numerical and experimental whirl orbits for speeds near the resonances. We can infer from the observed changes in the whirl directions that the minor axes of the measured whirls must also vanish for certain frequencies as the rotor passes through the resonances.

4.4 The response of the ABB

In this section we shall build on the results of the plain rotor investigations by considering the response of the two-ball ABB for a range of different imbalances.

4.4.1 An applied imbalance of 3 washers

In order for the balls to be added to the rotor, the perspex cover is removed and the balls are placed inside the disk. At this time we also apply six drops of 10W-40 grade motor oil to the race which provides some damping to the motion of the balls. The amount of oil is chosen so that the balls are able to overcome gravity and be ‘picked up’ by the rotation of the race when the disk is spun gently by hand. The cover is then replaced back onto the disk at the same orientation relative to the hub. During this procedure it is important to minimise any potential for an unwanted change in the rotor’s imbalance. This is achieved by carefully replacing the screws back into the holes from where they came and also by tightening them up to the same degree. To aid this operation the screws and holes are marked with coloured reference stickers, see Figure 4.2. The estimated change in imbalance due to the removal and replacement of the cover is estimated to be between 1-2 g mm, which is small compared to the 12.4 ± 0.5 g mm imbalance of each applied washer. An alternative to this procedure would be to incorporate holes in the perspex through which the balls could be placed [65], however this solution was unsuitable for the considered set-up as oil may have escaped through these openings.

The measured vibration response for the rotor with an applied imbalance of 3 washers and with two balls added to the ABB disk is illustrated in Figure 4.6. Panel (a) shows the rotor run-up (red curve) and run-down (blue curve) compared against the ‘without balls’ control case (grey curve) that was described in the previous section. Here we find that for speeds below the first resonance the vibration amplitude for the rotor with the balls is increased, whereas, for speeds higher than this resonance the vibration level is reduced. This automatic balancing effect can be further highlighted through a comparison of the ball positions and whirl orbits at specific rotation speeds. Panel (b) shows the response during the rotor run-up at the first rigid body resonance. The whirl shape is the same as that of the control, however, the amplitude has more than doubled. This occurs because the balancing balls find positions that add to the imbalance, see panel (d). By contrast, for supercritical speeds the balancing balls move to the opposite side of the race track (e). Hence, the balls act to reduce the imbalance and the resulting reduction in the vibration amplitude is clearly evident, see panel (c).

As given in Table 4.2, the 3-washer imbalance has a magnitude of ≈ 37 g mm. By comparison, each balancing ball has a mass of 0.44 g and acts at a radius of 42.8 mm. Thus, the total imbalance correction capability of the two balls can be calculated as $2 \times 0.44 \times 42.8 = 37.7$ g mm.

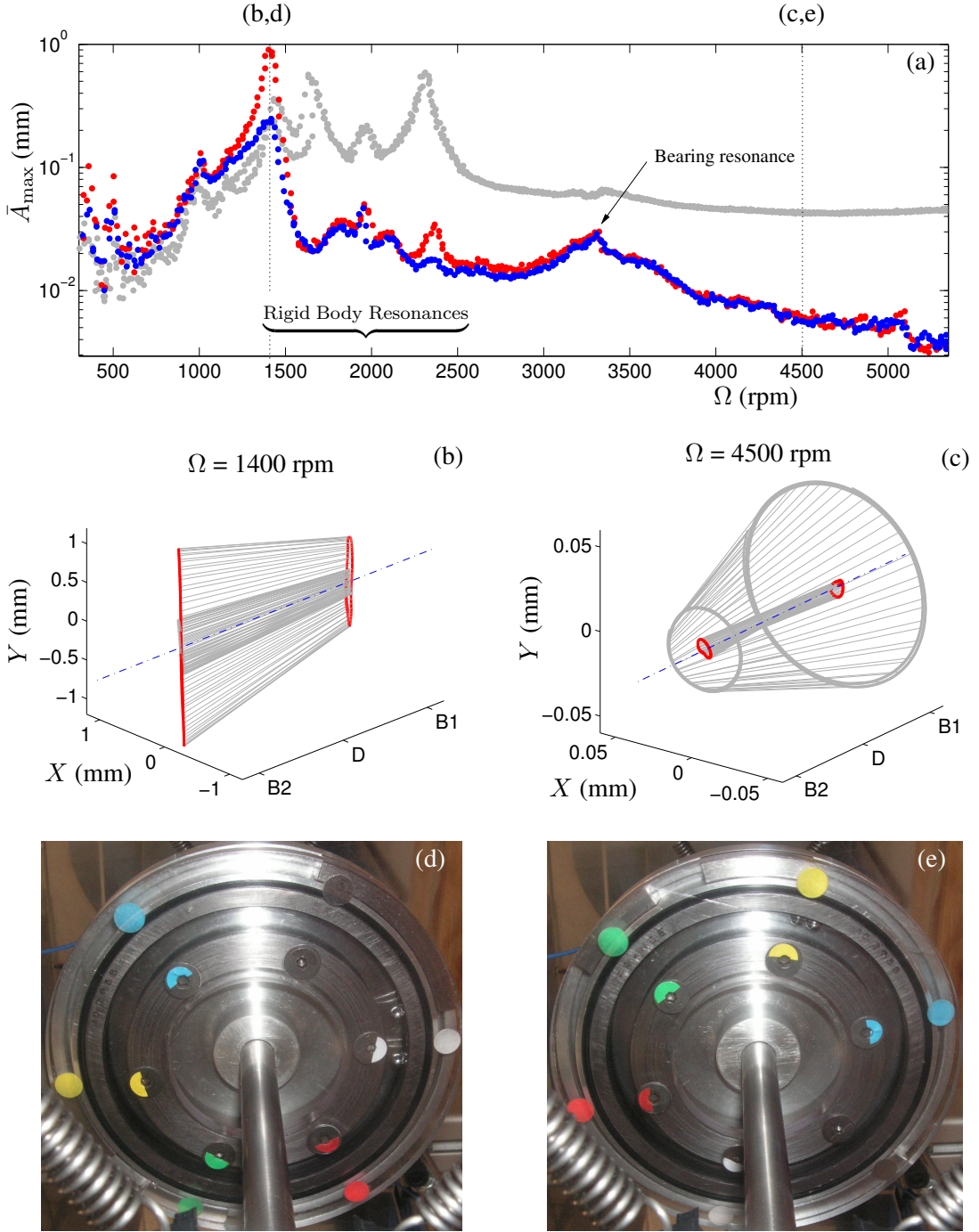


Figure 4.6. Measured response of the rotor with 2 balls in the ABB disk. An imbalance has been applied by removing 3 washers from the yellow screw. Panel (a) shows the lateral vibration level \bar{A}_{\max} upon variation of the rotor speed Ω for both the run-up (red), run down (blue) and control (grey) cf. Figure 4.5(a). The whirl orbits at the indicated data points are illustrated in panels (b) and (c) for the ABB (red) and control (grey). The corresponding ball positions are shown in panels (d) and (e), here the yellow screw is the light spot and the white screw is the heavy spot. The pictures were taken with a standard Konica Minolta DiMAGE X60 digital camera with the flash light enabled.

Therefore, to within experimental error, the imbalance of the balls matches that of the applied imbalance of the rotor. As a consequence, when the system is in the balanced state the balls are touching and lie directly in line with the light spot. In fact, a close inspection of Figure 4.6(e) reveals that the balls seem to be forced together with enough pressure that they slide past one another and ride partway up the groove so that they can occupy close to the same angular position.

A hysteresis effect can be seen in the frequency response curve of Figure 4.6(a) around the 1200-1500 rpm and 2200-2500 rpm ranges that contain the first and fourth rigid body resonances respectively. The blue curve of the rotor run-down has a lower vibration level than the red curve of the run-up, and for almost all the other test runs the same situation was found. We believe that this hysteretic behaviour occurs because once the balls have settled at the balanced positions the subsequent reduction in vibration levels at the critical speeds means that they are less likely to destabilise at the corresponding resonances on the run-down. In addition, the presence of a small amount of friction between the balls and the race acts to keep them in the positions that they have found.

As noted during the control study of Section 4.3, our rotor system possesses a non-linear resonance of the B2 bearing at around 3300 rpm. We believe that this occurs due to an incorrect installation of the bearing into the housing. (When installing a bearing it is important to push only on the ring that is being mounted, i.e. on the outer ring when fitting into a housing and on the inner ring when fitting onto a shaft. Otherwise the rolling elements will be pushed against the race which could lead to indentations and a damaged bearing). Because the bearing resonance is not caused by a mass imbalance, the balls are not able to eliminate the vibrations to the same extent that they have achieved in the higher 4000-5000 rpm operating range. Nevertheless, it is encouraging that the balls are not destabilised by the bearing resonance and that the ABB still effects a reduction in the vibration levels as compared with the plain rotor control case.

At this point it should be mentioned that the frequency response curves presented in Figure 4.6(a) is an example of a particularly good performance by the ABB. In other test runs there was some variability in the vibration levels for the ABB in the 1500-3000 rpm range, and these amplitudes were sometimes higher than that of the plain rotor case. Nevertheless, for operating frequencies above 3000 rpm that are supercritical to the rigid body resonances the vibration levels were consistently reduced and the balls were repeatedly observed in the balanced state positions. Furthermore, the striking of the base or support structure with a rubber mallet did not move the balls from those positions, or in other words, the balanced state was found to be robust to external perturbations. In order to illustrate and support these findings we shall present the results of further tests. However, we shall also reduce the applied imbalance to 2 washers so that the ABB is not at the limits of its imbalance capability.

4.4.2 An applied imbalance of 2 washers

The response of the ABB for an applied imbalance of 2 washers is illustrated in Figure 4.7. The measured vibration level for two separate runs are shown in panel (a), again the red curves are for the rotor run-ups, the blue curves are for the run-downs and the grey curves are for the control case with no balls. During the rotor run-up the vibration level of the ABB is worse than that of the control case for speeds below the first rigid body resonance. Between the first and last rigid body resonances the vibration level can either be reduced or increased depending on the specific speed of the rotor. Nevertheless, at supercritical speeds greater than 3000 rpm the vibration levels of the ABB are consistently less than that of the plain rotor for both the run-ups and run-downs. As discussed previously, in the 1200-2800 rpm range the amplitude of vibrations for the rotor run-downs are usually less than that for the corresponding run-ups. However, in this speed range there can be much variability in the system's response suggesting that there is a coexistence between competing states. If we compare the vibration levels of Figures 4.6(a) and 4.7(a) in the supercritical range, we find that the vibration levels of the ABB are higher for the reduced imbalance of 2 washers as compared to the 3-washer case. Again this result was repeatable, however, further discussion as to the possible reasons for such behaviour will be left until Section 4.4.4.

First we shall investigate the relationship between the ball positions and the ABB vibration amplitudes. To this effect, three separate runs were performed where the rotor speed was held constant at certain frequencies of specific interest. During each run and at each of these speeds three photographs were taken in order to identify the ball positions. In addition, the ball motions were confirmed with a Photron Fastcam SA1.1 high-speed video system. Because the bearing housing obscures the field of vision, the photographs could not be taken from an orthogonal viewpoint, see Figures 4.6 (d) and (e). Therefore, the photographs are first registered onto an orthogonal base image by applying a projective transformation using the Matlab 'Image Processing Toolbox'. The ball angles can then be determined directly from the transformed photographs, and the estimated error in these measurements is less than $\pm 2^\circ$. An alternative procedure would be to apply a protractor, for example via acetate, to the perspex cover. However, the photographs may still need to be registered with an orthogonal base image so as to avoid any perspective error when reading off the angles.

Figures 4.7 (b) and (c) illustrate that below the first rigid body resonance the balls are positioned on the heavy side of the rotor and this leads to a greater imbalance and higher vibration levels. At 700 rpm there was some evidence of periodic motion of the balls (magenta run) but by 1200 rpm they are in a steady state and lie close to the heavy spot.

For speeds between the rigid body resonances there is evidence of a variety of coexisting system behaviours which causes a variable performance of the ABB in this operating range. Figure 4.7(d) shows that at 1600 rpm, an oscillatory touching ball solution (green and magenta

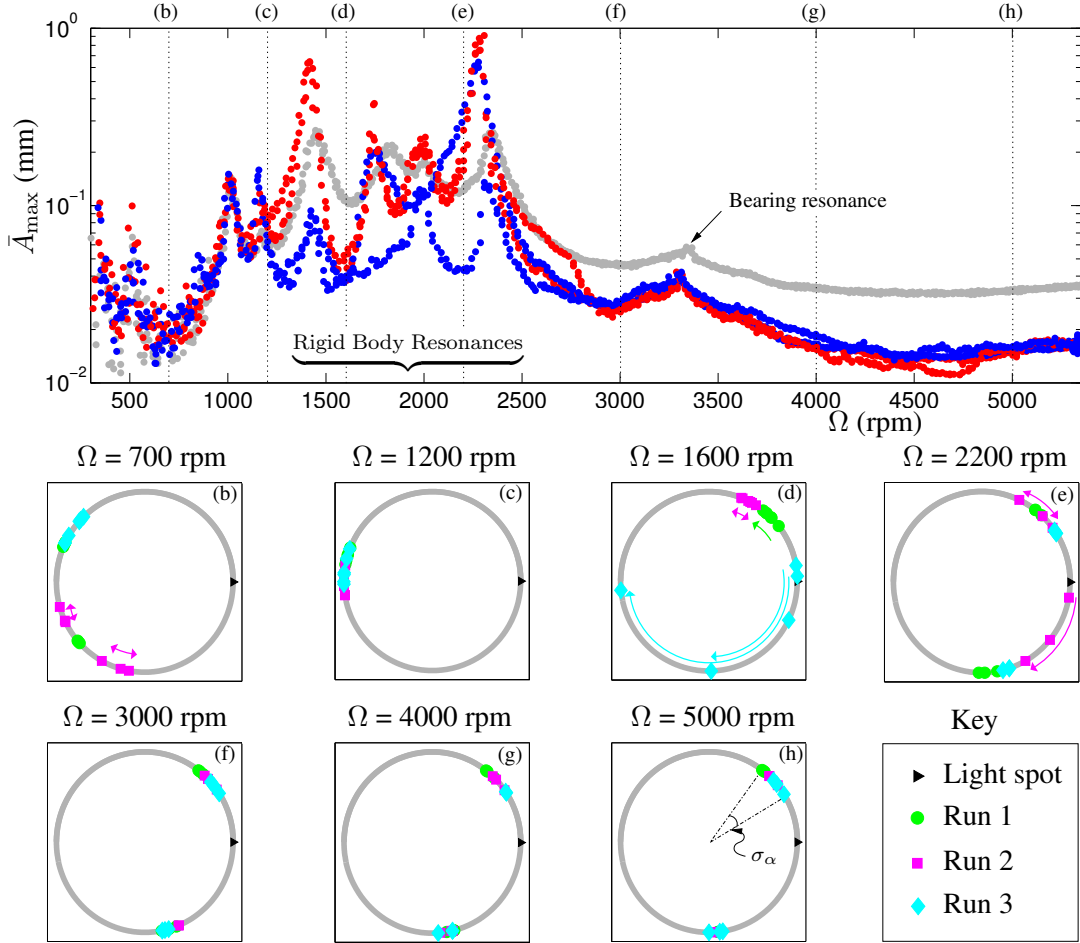


Figure 4.7. Measured frequency response and ball positions for the rotor with two balls in the ABB disk and an applied imbalance of 2 washers. Panel (a) shows the lateral vibration amplitude \bar{A}_{\max} upon variation of the rotor speed Ω for two rotor run-ups (red) and run-downs (blue) together with the control case (grey) cf. Figure 4.6. Panels (b) to (h) illustrate the ball positions for separate runs of the same system at which the rotor speed was held constant at the indicated rotation frequencies. The ball positions were again captured with a standard Konica Minolta DiMAGE X60 digital camera, and the ball motions were confirmed with a Photron Fastcam SA1.1 high-speed video system. The typical angular spread σ_α of the balanced state ball positions between different runs was measured to be $\sigma_\alpha \approx 20^\circ$.

runs) coexist with a destabilised solution in which the balls whirl about the race (cyan run). The destabilised ball state is accompanied by both a markedly higher vibration amplitude and an audible high pitched whirring sound that is produced as the balls travel around the race. As the system is rotating in the anti-clockwise direction we can see that the balls in this state tend to lag behind the rotor when whirling. This is in agreement with the theory of Section 3.5, here it was found that under certain conditions the balls may stall at a critical speed and continue to rotate at the eigenfrequency associated with the corresponding mode, see Figure 3.11. Applying these results to this case we may expect that the balls could stall at $\Omega_{\text{cyl},Y} \approx 1450$ rpm and remain whirling at this speed even as the rotor accelerates up to 1600 rpm. However, the determination of the ball speed lies outside the scope of the present work and we shall leave its study to subsequent investigations. For a higher rotation speed of 2200 rpm, panel(e), we can see that in two of the runs (green and cyan) the balls are split and reside near the balanced state whilst in the other run (magenta) there is a motion of the balls within the race. Whether this motion of the balls is periodic, chaotic or transitory could not be determined. However, it is evident that in the region of the rigid body resonances the behaviour of the ABB is unpredictable and that the system displays a rich variety of dynamics.

By contrast, for speeds above the rigid body modes the balls consistently find steady state positions that compensate for the imbalance of the rotor, see panels (f), (g) and (h). This leads to a reduced vibration level, and we also note that the non-linear B2 bearing resonance at 3300 rpm has little effect on the ball positions. Under perfect conditions, we would expect that the balls would reside in positions such that the angle between them would be bisected by the light spot. However it was found that the balls were rotated clockwise by between 15-20° from their ideal positions. This discrepancy between the predicted and measured ball positions could arise for a variety of reasons including errors relating to both the runway eccentricity and also to the measurement of the imbalance. In addition, it can be seen that the balls do not find the exact same positions for the three different runs. We believe that this behaviour occurs due to the presence of rolling friction between the balls and the race. If the balls lie within a certain angular range σ_α then the tangential autobalancing force is not large enough to overcome the frictional force and the balls remain at the same position. Thus, the effect of friction is to ‘spread out’ the equilibrium set of the balanced state from two point positions into two intervals on the race. Nevertheless, it is evident that the ABB reduces the vibration amplitudes for speeds above the rigid body resonances and that this occurs because the balls consistently find positions at which they act to compensate for the imbalance.

4.4.3 Effect of rolling friction

We shall briefly discuss an order of magnitude calculation for the effect of rolling friction on the range of possible residing positions for the balancing balls. We follow the treatment presented

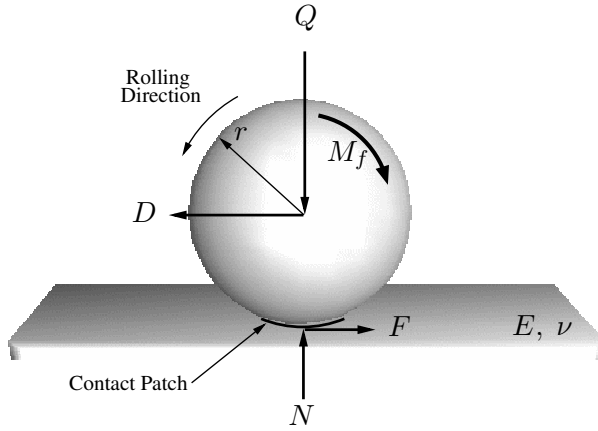


Figure 4.8. Free body diagram of the ball/race contact (adapted from [10]). Here Q is the centrifugal ‘force’, N is the normal reaction force, D is the autobalancing driving force and F is the opposing frictional force. See the text for definitions of the other variables.

by Chao *et al.* [10], in which an elastic race with Young’s modulus E and Poisson’s ratio ν is taken to be in Hertzian contact with a rigid ball of radius r , see Figure 4.8. By assuming that the moment of rolling friction M_f is proportional to the hysteretic energy loss W as the ball rolls and elastically deforms the race, we may write

$$\begin{aligned} M_f &\propto W, \\ &\propto \int_A p(x, y) d(x, y) dA, \end{aligned} \quad (4.2)$$

where $p(x, y)$ and $d(x, y)$ are the pressure and deformation distributions respectively, and A is the contact patch on the race which is assumed to be circular. After some calculation (omitted here, for further details see also [7, §14]) the moment of rolling friction can then be given as

$$M_f = \frac{3\mu_f}{16} Q^{\frac{4}{3}} \left[\frac{3}{4r^2} \left(\frac{1-\nu^2}{E} \right) \right]^{\frac{1}{3}}. \quad (4.3)$$

Here

$$Q = m(\Omega + \dot{\alpha})^2 R,$$

is the centrifugal load that the ball imparts on the race and μ_f is the rolling friction coefficient which has units of length and incorporates the information on the size of the contact patch. The quantity $\mu_f [(1 - \nu^2)/E]^{\frac{1}{3}}$ can then be thought of as a property of the race material and its value should be minimised for the optimum performance of the ABB. For steel this value has been measured to be $0.8 \times 10^{-7} \text{ N}^{-1/3} \text{ m}^{5/3}$ which is lower than the corresponding values of $1 \times 10^{-7} \text{ N}^{-1/3} \text{ m}^{5/3}$ for copper and $2 \times 10^{-7} \text{ N}^{-1/3} \text{ m}^{5/3}$ for aluminium [10]. In more detailed treatments of the effects of ball/race friction [10, 62, 65] there is a complicated relationship

between the coefficient of friction, and the typical spread of final ball positions σ_α , however, for the purposes of this discussion we shall use the relation $\sigma_\alpha \propto M_f$ which is an approximation that holds well when σ_α is small.

Table 4.4. Comparison of system parameters. The values of M_f are calculated using (4.3) and have been scaled with respect to the value given in Chao *et al.* [10].

Parameter	Present study	Chao <i>et al.</i> [10]
Ball mass, m	0.44 g	0.261 g
Ball radius, r	2.38 mm	1.25 mm
Rotation speed, Ω	3000-5000 rpm	7000 rpm
Race radius, R	42.8 mm	16.5 mm
Race material	Hardened Steel	Steel
	0.49 (3000 rpm)	
Moment of rolling friction, M_f	1.05 (4000 rpm) 1.90 (5000 rpm)	$\equiv 1$
Typical spread in angle of final ball positions, σ_α	20° (Figure 4.7(f)-(h))	30°

In Table 4.4 we compare the experimental parameters for the present set-up with that of Chao *et al.* [10]. Here, we find similar values for the moment of rolling friction M_f when the operating speed of our rig is 4000 rpm. From Figures 4.7 (f)-(h) we can determine that the spread in ball angles is $\sigma_\alpha \approx 20^\circ$ which is a smaller value than that found by Chao *et al.* for the set-up studied in [10]. This result has a variety of possible explanations, for example, in our device the balls and race surface have been especially hardened and polished by the manufacturer. Also, the application of oil to the race provides lubrication to the contact surfaces and it is expected that the effective race friction factor $\mu_f [(1 - \nu^2)/E]^{1/3}$ has been reduced by these efforts.

During our experimental runs the rotation speed is gradually increased and the balls settle at their steady state positions at a frequency of around 3000 rpm, again see Figure 4.7. For this operating speed the value of M_f is only about 50% of its value at 4000 rpm, therefore, one might conclude that the balls find positions close to the balanced state at 3000 rpm and are then progressively pushed further into the race as the rotation speed is increased. (Note from 4.3 that the moment of rolling friction scales like $\Omega^{8/3}$ and so the balls are more likely to stick for higher rotation speeds.) Thus, if the rotor run-up is too rapid, the balls may not have time to settle before they are fixed at locations other than their predicted balanced positions. Indeed, this was sometimes observed to be the case in experimental tests where a rapid run-up to a fixed rotation speed was performed rather than the slow quasi-static sweeps that were used to generate Figures 4.6 and 4.7. If such events occurred an immediate reduction in the rotor speed

was required in order to avoid dangerously high vibration levels.

Although it is clear that more work is required in order that the ball/race interactions can be described in more detail, we hope that we have highlighted a possible approach towards its study. Also, we note that this future research will be especially important if ABBs are to be used in applications such as gas turbines for which the centrifugal loads can be many orders of magnitude higher than the levels that were present in our experiments.

4.4.4 Further changes to the applied imbalance

We complete this section by presenting some further frequency response results for different amounts of the applied imbalance. Figure 4.9 shows the vibration amplitude as we increase the imbalance from 0 washers (nominally balanced) up to 4 washers. Most of the common features of the ABB performance have been discussed previously and we summarise them here as:

1. An increase in the vibration levels for rotation speeds below the first rigid body resonance.
2. Variable performance in the speed range of the rigid body resonances.
3. Good performance in the frequency range that is supercritical to the rigid body resonances.
4. Usually the vibration levels are lower on the run down than on the run up.

Figure 4.10 shows the vibration levels for the different amounts of imbalance during the 4000 to 5000 rpm operating range. Again, the vibration level for the plain rotor (grey) is plotted against the ABB for the rotor run up (red) and run down (blue) and the theoretical predictions are shown with the dashed lines. As expected, there is a linear relationship between the amount of imbalance and the vibration level for the plain rotor. Next, with the balls inside the balancing disk we find that the ABB does not have much effect on the amplitude of vibration for a 0 or 1 washer imbalance, however, the vibrations are noticeably reduced for the higher applied imbalances of 2–4 washers. It is also clear that the ABB performs best with a 3-washer imbalance which is the set-up where the ABB is at the limits of its balancing capability.

As discussed in Section 4.4.3, if we were to include the effects of rolling friction into the mathematical model then we would find that the equilibrium set of the balanced state would ‘spread out’ from point positions, into intervals on the race that are centred around the desired balanced state [10]. As a consequence, the balls may then have errors in their positions that are proportional to the amount of rolling friction and it is this effect that we believe is responsible for some of the discrepancies between the measured and theoretical ABB vibration levels for the cases with 0–2 washer imbalances.

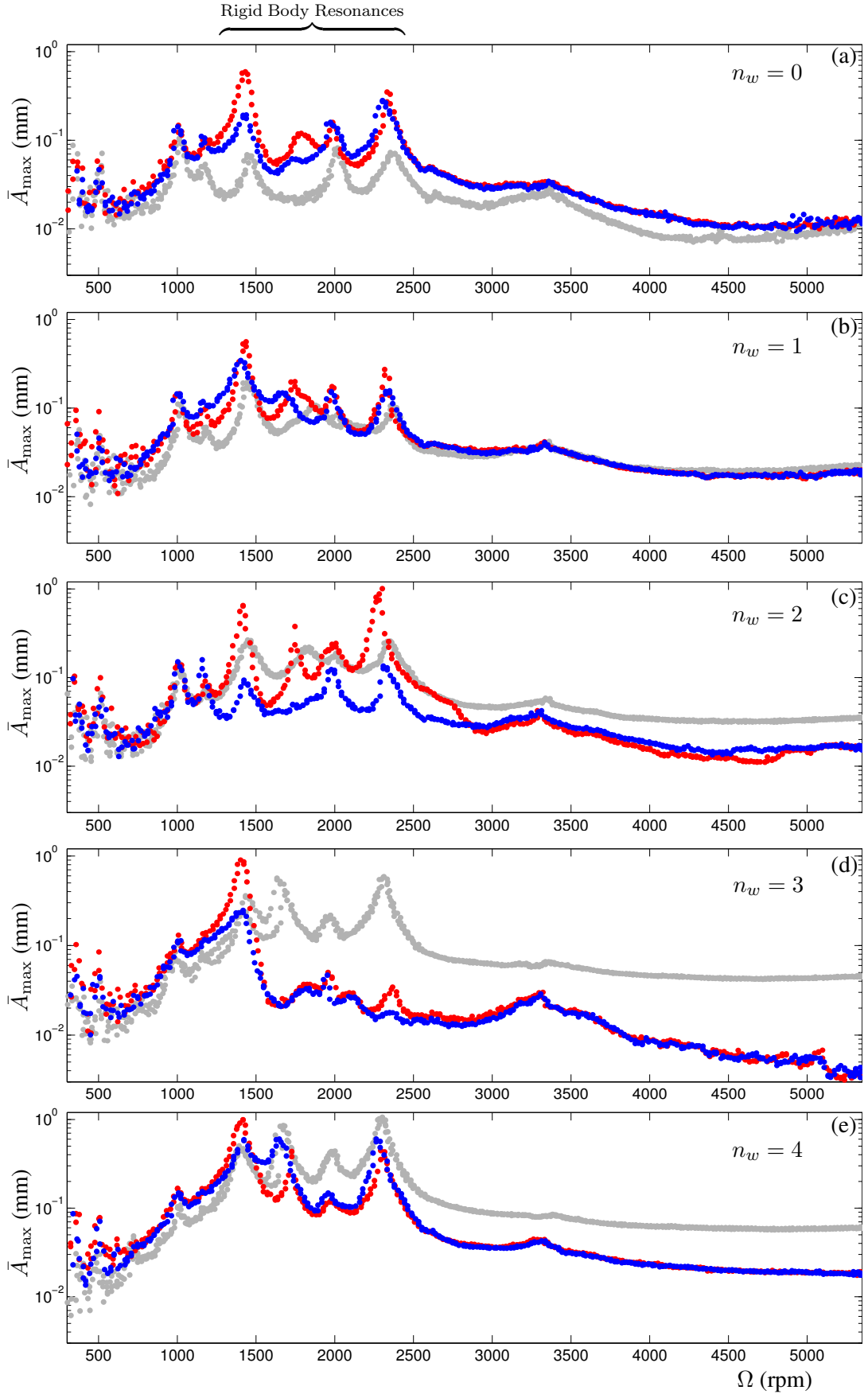


Figure 4.9. Measured frequency responses for different amounts of removed washers n_w , see Table 4.2 for the estimated imbalance parameters. The lateral vibration amplitude \bar{A}_{\max} is plotted upon variation of the rotor speed Ω for the run-up (red), run down (blue) and control (grey). All graphs are displayed on the same logarithmic scale.

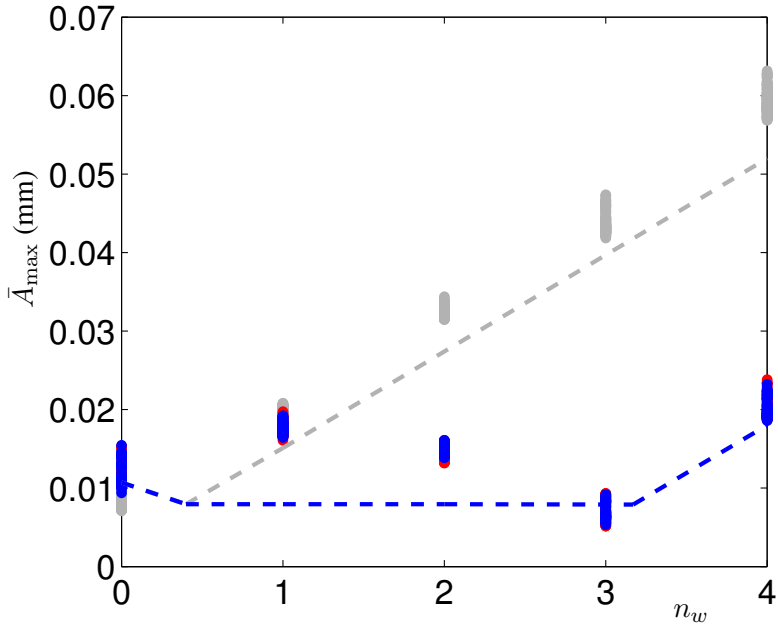


Figure 4.10. Vibration amplitudes \bar{A}_{\max} of the plain rotor (grey) and the ABB (red and blue) for a different number of applied washer imbalances n_w in the 4000-5000 rpm speed range. The theoretical vibration levels for the corresponding steady states are shown with the dashed lines.

Applying a similar reasoning, one may assume that the good performance of the ABB for the 3 and 4 washer cases occurs because the increase in the amount of imbalance helps the balls to overcome the rolling friction force so that they can reside closer to their desired positions. Also, for these amounts of imbalances the balls are touching, see Figure 4.6(e), and they may ride up the race in order to achieve almost exactly the same angular position. More tests will be needed in order to assess whether the ABB generally performs best when the balancing ball masses are matched to the rotor imbalance.

4.5 Numerical simulation

We shall now compare some of the results of the experimental investigations with numerical simulations that are generated from the model that is given by equations (3.5) and (3.6). We take the relevant dimensional parameters from Tables 4.1-4.3, however a simple routine is incorporated into the software that performs the non-dimensionalisation procedure of Section 2.1.4. The system is then numerically integrated with the Matlab solver `ode45` and the results are converted back into dimensional quantities before they are plotted.

The only parameter that we have yet to consider is the race damping value c_b . This quantity was initially estimated from the decay rate of the motion of a ball as it was placed on the

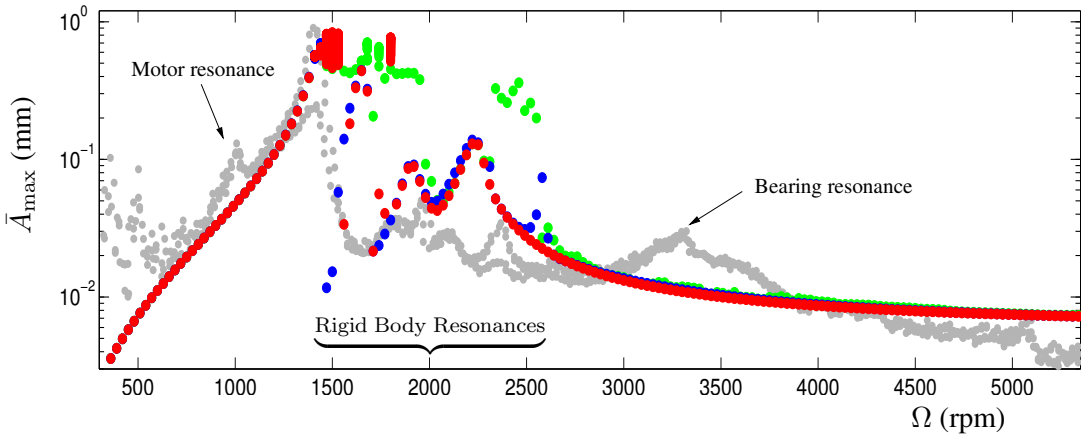


Figure 4.11. Comparison of simulations with the measured response for the ABB with a 3-washer imbalance. The log scaled lateral vibration level \bar{A}_{\max} is plotted against the rotor speed Ω for three different values of the non-dimensional race damping parameter c_b , namely $c_b = 0.01$ (green), $c_b = 0.1$ (red) and $c_b = 1$ (blue). In all cases initial conditions are such that the rotor begins in the undeflected position and $(\alpha_1, \alpha_2) = (\beta, \beta)$, that is the balls start at the same angle as the heavy spot. The experimental data is shown with the grey curve cf. Figure 4.6.

side of the race and allowed to fall from rest. However, this method leads to a substantial overestimation of the value of c_b because the oil pools at the bottom of the race and stops the ball almost immediately. Therefore, as c_b is an uncertain quantity we shall produce plots for three different values of the dimensionless race damping.

4.5.1 An applied imbalance of 3 washers

The response of the ABB for the 3-washer imbalance case that was discussed in Section 4.4.1 is illustrated in Figure 4.11. The vibration amplitudes are displayed for three different values of the non-dimensional race damping, namely, $c_b = 0.01$ green, $c_b = 0.1$ red, and $c_b = 1$ blue. The initial conditions for the system are such that the balls begin at rest with respect to the disk and in line with the heavy spot, therefore the initial imbalance of the rotor is maximised. For each value of the rotation speed Ω the system's response is simulated and after the transients have died away the maximum values of the vibration amplitude \bar{A}_{\max} are plotted.

We find that for speeds below the first rigid body resonance the numerical vibration levels for all values of the race damping are the same, furthermore these vibration amplitudes agree closely with the experimental results. We recall that in this subcritical speed range the balls find positions on the heavy side of the rotor and act to maximise the imbalance.

By contrast, in the frequency range of the rigid body resonances the simulations have different responses that depend on the amount of race damping. For the low damping value $c_b = 0.01$

(green curve), we find the highest vibration levels. This occurs because in certain speed ranges the balls destabilise and subsequently whirl about the race. For the other race damping values the vibration amplitudes are again variable, however the qualitative characteristics of these responses find a better match with the experimental data. It is interesting to note that for this particular experimental run the ABB has performed better than anticipated. As mentioned in Section 4.4.1, we believe that this has occurred because once the balls found their balanced positions after the first resonance, the resulting reduction in vibration levels meant that they were less likely to destabilise at the subsequent critical speeds. Nevertheless, other experimental test runs illustrate that the performance of the ABB is highly variable in the 1500-3000 rpm speed range and so quantitative agreements in this regime should not be expected.

Next, for speeds higher than 3000 rpm the simulated steady state responses for all values of the race damping are the same, and we also find a good quantitative agreement with the experimental results. We recall that in this frequency regime the balls are positioned on the light side of the rotor and act to minimise the imbalance.

From a design perspective these results are encouraging. We have demonstrated that a good fit to the experimental data can be achieved with the simple model of (3.5) and (3.6). Furthermore, we have found that the determination of an accurate value for the amount of race damping is not necessary for the prediction of the performance of the ABB in the supercritical operating frequency regime.

Finally, we note that the rotor run-ups and run-downs have not been included in the considered equations of motion. This is justified because during the experimental tests the rotation speed was maintained at each frequency, and so the effect of the torsional acceleration can be assumed to be small. Also, one should not expect to find the motor and bearing resonances in the simulated responses as these are beyond the scope of the model. In the next section we shall present the results of further simulations in which the ball motions and positions are also highlighted.

4.5.2 An applied imbalance of 2 washers

Figure 4.12 illustrates simulated responses of the ABB for the 2-washer imbalance case that was discussed in Section 4.4.2. Panel (a) shows the vibration amplitudes for the three different race damping values that were considered in Figure 4.11 and the initial conditions are again such that the starting imbalance of the rotor is maximised. In panel (b) the corresponding maxima and minima of the ball angles α_1 (dots) and α_2 (circles) are illustrated for the case with $c_b = 0.1$. These values are plotted together with the phase φ_{cz} , which is defined to be the angle from the whirl centre in the plane of the disk O_z , to the race centre C_z , see (d). We note that in the formulation of the mathematical model the direction of the couple imbalance is

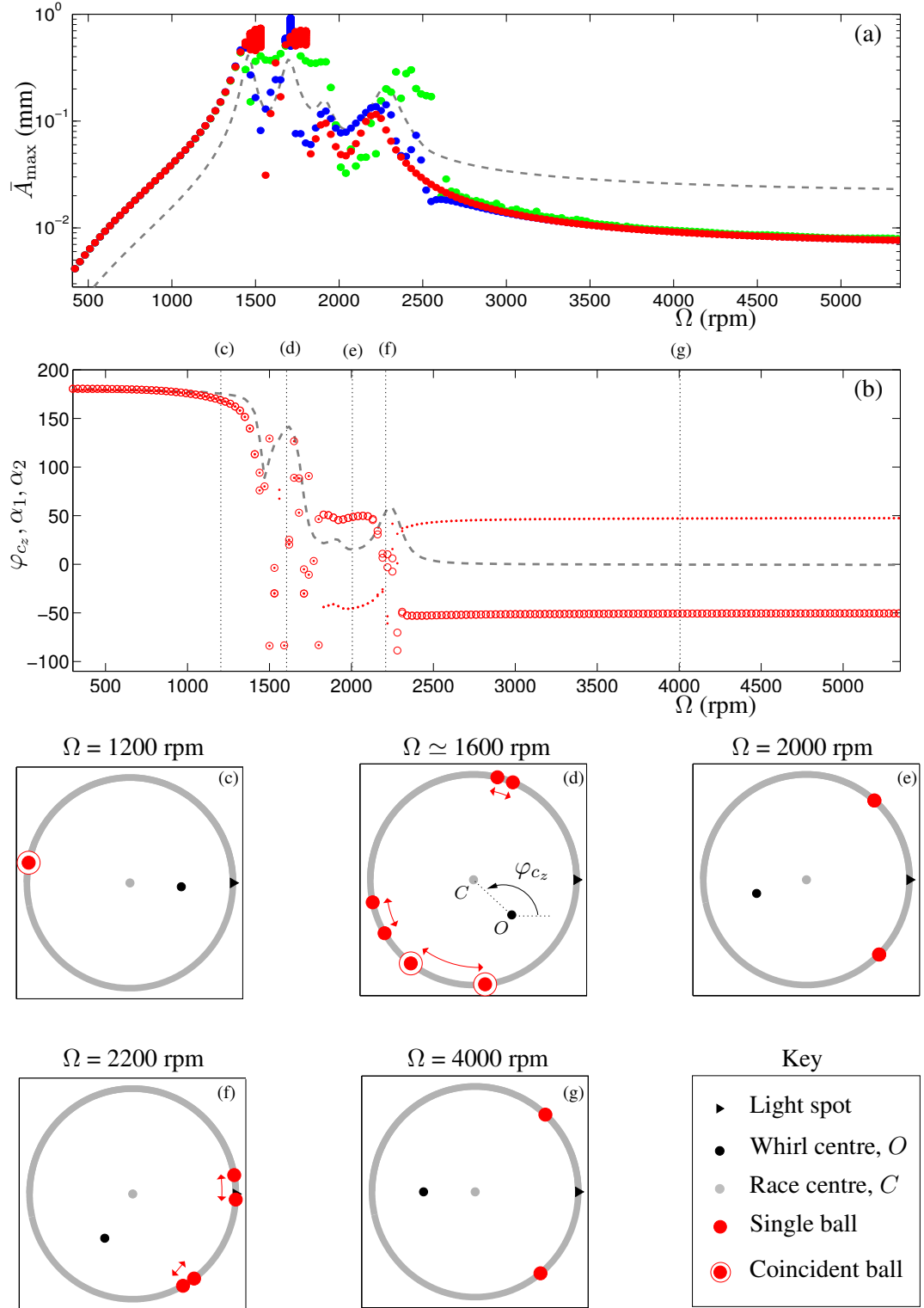


Figure 4.12. Simulated frequency response and ball positions for the automatic balancer with two balls and an applied imbalance of 2 washers. Panel (a) shows the lateral vibration amplitude \bar{A}_{\max} upon variation of the rotor speed Ω for three different values of the non-dimensional race damping parameter c_b , namely $c_b = 0.01$ green, $c_b = 0.1$ red and $c_b = 1$ blue. The control case of the simulated plain rotor is shown by the dashed grey line cf. Figure 4.7. In panel (b) the ball positions α_1 and α_2 have been plotted against Ω for the race damping value of $c_b = 0.1$ and the phase of the disk φ_{c_z} is also shown for reference. Panels (c) to (g) illustrate the dynamics of the balls at the specific speeds indicated. Note in panel (d) two distinct observed behaviours are superimposed. Compare with the experimental results of Figure 4.7.

defined to be at 0° . However, here it is more appropriate to use the light spot as the 0° direction and so we have applied a constant phase shift of $-(\beta - \pi)$ to all angles in order to adjust for this change of reference, see also Figure B.2. The simulated positions of the balls for some specific rotation speeds are shown in (c) to (g) and, if moving, arrows indicate their motion.

Again, for rotation frequencies below the first rigid body resonance the response is the same for the three different c_b values (a). We find that the balls remain on the same side of the race as the heavy spot and that this configuration leads to an increase in the vibration level of the rotor. Likewise, if the rotation speed is greater than 2700 rpm and so is supercritical to the rigid body resonances, then the balls find their balanced positions and reduce the vibration amplitudes, regardless of the value taken for c_b . Thus, the predominant role of the race damping in this speed regime is to effect the transients of the ball motions rather than to alter the stability of the balanced state. (For examples of transient ball responses in races with different damping values we refer the reader to Section 2.3.2). For the parameter value $c_b = 0.1$ we have found both the greatest variety of solutions types, and also, the closest agreement with the experimental data of Figure 4.7, therefore we have focused on this race damping value for the ball plots of the remaining panels.

In panel (b) the relationship between the phase of the plain rotor at the disk φ_{c_z} and the ball positions α_1 and α_2 , is clearly demonstrated. As expected, for frequencies below the first critical speed, the heavy side of the disk is thrown towards the outside of the whirl and we have a solution with the balls coincident and on the heavy side (c). As the rotor passes between the first and second critical speeds $\Omega_{\text{cyl},Y} < \Omega < \Omega_{\text{cyl},X}$, the disk undergoes a backward whirling motion and the phase changes rapidly with rotation speed as the rotor attempts to self-centre with respect to the cylindrical mode. For speeds in this range we have found a variety of solutions, such as oscillating states whereby the balls can either be coincident or touching (d), and also destabilised solutions in which the balls lag the rotor and begin to whirl about the race. This behaviour is in good qualitative agreement with the experimental results that we have discussed in relation to this speed range, compare with Figure 4.7 (d). For frequencies in between 1800 rpm and 2200 rpm, we find that the phase of the rotor approaches near to 0° , and so the light side of the disk is brought to the outside of the whirl and the balls find stable positions that are close to the balanced state (e). We also note that the third resonance at $\Omega_{\text{con},X} \simeq 1950$ rpm has a relatively small associated phase shift, and it is this property of the mode which encourages stable steady state solutions in the nearby speed range. As the rotor passes through the final rigid body resonance at $\Omega_{\text{con},X} \simeq 2310$ rpm there is another change in the phase of the disk as the rotor self-centres with respect to the conical mode. This can lead to oscillations of the balls about the balanced positions (f) and in some cases they can destabilise completely. However, for speeds greater than 2300 rpm that are supercritical to the rigid body resonances we find that the light spot is again brought back to the outside of the whirl and the balls find stable positions that act to balance the disk (g).

4.6 Discussion

The aim of this chapter has been to build on the theoretical analysis that was presented in the first part of this thesis by providing some empirical data for the validation of the mathematical model. To this effect, we have designed and built an experimental rig that possesses both cylindrical and conical modes that are excited by the static and couple imbalances respectively. Once the rig was built experiments were performed on the plain rotor so that the system parameters could be determined. It was found that the supports had stiffnesses that were significantly anisotropic, and also that the rotor possessed an unexpected nonlinear bearing resonance in the supercritical operating range. Nevertheless, a good qualitative and quantitative description of the plain rotor system was made and these sets of results provided a control against which the vibration levels of the ABB could be compared.

The performance of the ABB has been assessed for a variety of different applied imbalances for which both the eccentricity and misalignment of the rotor were taken into account. It was found that for all but the case in which the rotor was already nominally balanced, the ABB reduced the vibration levels in the speed range that was supercritical to the rigid body resonances. Some evidence was presented that suggests that the ABB also performs best when the mass of the balls is matched to the size of the imbalance. We believe that this behaviour occurs because the errors in the position of the balls are reduced when they are touching in the balanced state, however, further tests are needed in order to confirm this hypothesis.

The dynamics of the balancing balls were observed for a specific applied imbalance of 2 washers. As expected, it was shown that for speeds below the first rigid body resonance the balls cause an increase in the vibration levels by finding positions on the heavy side of the rotor. By contrast, for speeds supercritical to the rigid body resonances the balls move to the light side of the rotor and effect a reduction in the vibration levels. In addition, the behaviour of the ABB for supercritical operating speeds was repeatable and it was found that the balls consistently reside in positions that were close to the balanced state. Again, the dynamics of the balls during the rigid body resonances were unpredictable and for this speed range we found a rich variety of system solutions. These included coexisting oscillatory touching ball states, more complex motions where the balls were separated and also destabilised solutions whereby the balls would whirl about the race and lag behind the speed of the rotor.

In order to accurately describe the behaviour of this ABB system we have used a model that is based on a four degree of freedom rotor that not only includes the effect of rotor misalignment and eccentricity, but also includes the effect of support anisotropy. With this model we have established a good agreement between the numerical simulations and the experimental results. For the supercritical frequency range the model produces an approximate quantitative match with the measured data and the causes of the discrepancies have been discussed in relation

to both the presence of rolling friction, and also, race eccentricity. During the rigid body resonances the dynamics of the ABB is highly nonlinear and for this speed range the agreement between theory and experiment is mainly qualitative. However, the model has been able to successfully reproduce many of the solution types that have been found experimentally.

The results from this chapter have provided both a demonstration of the validity of the mathematical model and also a ‘proof of concept’ for the feasibility of using the ABB in applications where the rotor is subject to non-planar tilting vibrations. Unfortunately, it has been beyond the scope of the present work to fully investigate the effect of factors such as rotor run-up, race damping and the number and size of the balancing balls. However, we shall provide a brief discussion of these and other such issues in the future research section of the following concluding chapter.

Chapter 5

Conclusion and outlook

Here we shall discuss the key findings of the thesis and identify possible directions for future research. In addition, we shall provide design guidelines for the implementation of ABBs in ‘real-world’ machines.

5.1 Summary

The main aim of this work has been to improve the understanding of automatic balancers so that in time they can be incorporated into rotating machines of a greater complexity. Specifically, we have extended the ABB model so that it includes the effect of out-of-plane tilting motions and couple type imbalances. Furthermore, the influence of certain device asymmetries have been determined and an experimental proof of concept has been provided. With these points in mind, we summarise the thesis as follows.

In Chapter 2, we presented the first nonlinear bifurcation analysis of a two-plane automatic balancer. The out-of-plane tilting motions are described in terms of Euler angles, and an autonomous system of governing equations is then derived through the use of rotating coordinates. The steady states of this system are determined explicitly and numerical continuation techniques are employed in order to find instabilities of these states in terms of bifurcations.

It was shown that for sufficiently high rotational speeds the considered device is capable of effectively eliminating imbalances arising from both mass eccentricity and principal axis misalignment. However, the bifurcation analysis also demonstrates that there is a complex interdependence between the stability of the ABB and the other characteristics of the rotor set-up. Furthermore, numerical simulations highlighted the coexistence of stable balanced operation with other less desirable dynamics.

In Chapter 3 the ABB model was extended by including effects such as support anisotropy and rotor acceleration. The symmetry of the imbalance was considered, and techniques from

equivariant bifurcation theory were used in order to demonstrate that operation above the highest rigid body critical speed is a necessary condition for the stability of the balanced state.

Next, we investigated mechanical set-ups in which either the supports or the ABB device were asymmetric. Here it was shown that, provided the imbalance is small, the balanced state is robust to the considered asymmetries. In addition, simulations that included the effect of rotor run-up were performed. These results illustrate that a high race damping value prevents destabilised ball motions from occurring in the range of the critical speeds.

In Chapter 4 we presented an experimental study of a specific ABB system. The rig is shown to be capable of passing through multiple resonances and of operating in the highly supercritical frequency regime. The performance of the ABB is assessed for a variety of different imbalances and a reduction in the vibration level is consistently observed for sufficiently high rotation speeds. For lower speeds the coexistence of steady state operation with more complex dynamics is also found, and we show that this behaviour can be replicated by the ABB model.

The analysis of the first part of this thesis illustrates that the dynamics of the ABB is heavily dependent on many parameters of the rotor set-up. In particular, even though supercritical rotation speeds are necessary, they are not sufficient to enable successful operation of the balancer. Therefore, detailed dynamic considerations are crucial for the successful design of practical ABB devices. The experimental validation of Chapter 4 demonstrates that this design analysis can be carried out using the models and techniques that have been described in Chapters 2 and 3.

5.2 Future research

The systems that we have considered in this thesis have been based on an underlying four-degree-of-freedom rigid rotor model. However, many high speed rotating machines possess flexible characteristics and can deform under centrifugal loading. Furthermore, studies by Chung and Jang [13] and Ehyaei and Moghaddam [20] have demonstrated the feasibility of using ABBs in specific flexible rotor set-ups. Therefore, a natural extension to the research would be to incorporate the dynamics of an ABB-like mechanism into existing finite element method (FEM) code. This would enable accurate quantitative predictions to be made for flexible rotors with highly complex geometries. A possible approach would be to derive the equations of motion of the ABB, with the underlying rotor structure taken to be the beam element of the FEM software that is to be adapted. (For example, with packages such as MADYN 2000 [15] and DynRot [23] this is the twelve-degree-of-freedom Timoshenko beam element [24, §5.3]). This could be achieved by combining the models of Chapter 3 with those of [13] and [20].

In Section 2.3 it was shown that a stable balanced state could coexist with destabilised ball whirling motions. Since the latter solutions are highly undesirable, it would be beneficial to

determine the conditions for which balanced operation is *globally* stable. A possible approach would be to use numerical continuation software such as AUTO [16] to follow the ball whirling states and then to subsequently find the regions of parameter space in which these solutions are themselves unstable. Alternatively, one could attempt to construct a Lyapunov function for the balanced state [59]. One may assume that both methods would result in explicit conditions for the required amount of race damping.

Further investigations could also be conducted into the characterisation of the codimension-two pitchfork-Hopf points that act as organising centres for the dynamics of the ABB and give rise to the Hopf instability curves. A detailed analysis would seek to explain why the Hopf bifurcation curves are born at the resonances, and it may also be possible to determine the asymptotic behaviour of these instabilities in terms of the system parameters. This study should first be carried out for an isotropic single-plane ABB, before then proceeding onto more complicated mechanical set-ups. An investigation similar to that presented in Section 3.2 could be conducted in which the starting point for the analysis would be the appropriate normal form for the co-dimension two pitchfork-Hopf bifurcation.

Other avenues for future research arise from the experimental work of Chapter 4. An obvious extension would be to include a second ABB onto the existing rig so that the automatic two-plane balancing procedure could be validated. In fact, this was the original intention of the experiment. However, a manufacturing error in one of the aluminium hubs meant that the fit of the steel race insert was slightly loose. As a consequence, the runway eccentricity of this second device was of a comparable size to the mass eccentricities that arose due to the applied imbalance. Therefore, in order to achieve the most accurate results, we felt it was appropriate to concentrate on the experimental validation of the single-plane balancing process.

More work is also needed in order to reach an optimal design for a particular physical application. For example, the analysis conducted by Green *et al.* [27] suggests that although the two-ball set-up is optimum in terms of local stability, the multi-ball configuration may add to the robustness of successful operation. Preliminary tests have been carried out in order to determine the optimum number of balls for the experimental set-up of Chapter 4, however no firm results have so far been achieved. Nevertheless, we believe that the most suitable ball configuration is highly problem specific, and so an appropriate course of action would be to determine these design details with the aid of a prototype.

Finally, alternative designs of automatic balancers should also be considered. For example, Horvath *et al.* [33, 32] have demonstrated that positioning errors due to friction can be significantly reduced by using pendulums as balancing masses instead of balls, see also Section 1.4.2. Similarly, disks can be used as the balancing masses, and a device of this type is illustrated in Figure 5.1. This automatic balancer has been designed by a team of Rolls-Royce graduate trainees and was tested at the BLADE laboratories at the University of Bristol [3].

The mechanism comprises of two weighted disks that are free to rotate on independent bearings. Centrifugal clamps fix the disks during the rotor run-up and then automatically bend back to release the disks for the sufficiently high rotation speeds at which the auto-balancing effect takes place. Another novel method, recently proposed by Nagato *et al.* [44], uses an ultraviolet (UV)-curing resin to compensate for the imbalance. In this study, a liquid resin is injected into the rotor, and this positions itself opposite the imbalance at speeds above the main resonance. Whilst in the balanced configuration the resin is solidified with UV light and in this manner the imbalance of the rotor is permanently corrected. We note that although there is a wide variety of possible design solutions, they all operate under the same underlying auto-balancing principle. Therefore, the methods and techniques presented in this thesis will also be useful for the analysis of these different types of balancers.

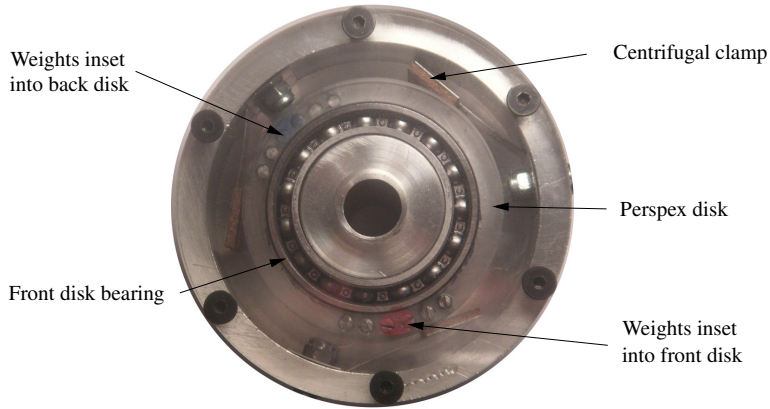


Figure 5.1. Rolls-Royce disk balancer [3].

5.3 Recommendations for automatic balancer design

In conclusion, we suggest the following design guidelines for situations in which an automatic balancer is being considered:

- Develop a model of the rotor that is to be balanced. This can be done either through existing FEM code or with reduced order models such as those that have been presented in this thesis.
- Determine the frequency ranges for which the shaft is self-centered at the axial location of the proposed balancing plane. These speeds will form the candidate operating ranges for the automatic balancer.
- Determine the required mass imbalance tolerances. Consider whether it is possible to manufacture a race with a runway eccentricity less than the required mass eccentricity

tolerance. If this is achievable then a ball-type balancer may be an appropriate solution. However, if the required accuracy of the race geometry is unattainable then other forms of balancing masses such as weighted disks or UV-curing resins may still be suitable [32, 44].

- Check the stability of balanced operation. This can be achieved using the methods developed in Chapters 2 and 3. Specifically numerical continuation software can be used to map out the regions of stability in various parameter planes.
- Conduct numerical simulations to assess the robustness of balanced operation to effects such as rotor run-up and variations of the initial conditions. The models presented in Section 3.1 are suitable for this purpose.
- Consider fixing the masses whilst the rotor is passing through its resonances.
- Ensure that the motion of the balancing masses have sufficient viscous damping in order that destabilised states can be avoided.
- Dry friction opposing the movement of the balancing masses should be minimised.

Appendix A

Physical interpretation of the Hopf bifurcation

In this appendix we present a physical interpretation of the automatic ball balancer (ABB) dynamics near a Hopf bifurcation.

A.1 Supercritical and subcritical Hopf bifurcations

In this thesis we have found that as the rotation speed Ω is varied, the local stability of the balanced state can change through a process called a Hopf bifurcation. This bifurcation occurs as a pair of complex conjugate eigenvalues of the linearized system pass through the imaginary axis. This process is indicative of an oscillatory type of instability and is associated with the birth of a periodic orbit. There are two types of Hopf bifurcation which are called *supercritical* and *subcritical*, respectively. Moreover, depending on which case occurs, the resulting solutions will have qualitatively different dynamics.

In order to simplify the following discussion we shall restrict attention to a planar ABB that is equipped with a single ball. In addition we assume that its mass has been chosen such that the ball exactly balances the rotor when it resides opposite the imbalance at $\alpha = \pi$. For this setup we illustrate some schematic frequency responses in the vicinity of both types of Hopf bifurcation, see Figure A.1. Here the varying parameter is the rotation speed Ω and the solution measure is the ball angle α . The left hand diagram shows the situation for a supercritical Hopf. Here we find that for high enough rotation speeds the balanced state is stable and the ball remains at an equilibrium position opposite the rotor imbalance, ①. As the speed decreases through Ω_b , the balanced state destabilises in a supercritical bifurcation and a stable periodic orbit is born. Physically, this orbit corresponds to a small-amplitude ball oscillation about the now unstable balanced equilibrium position, ②. Because the onset of the ball oscillations is gradual, a supercritical bifurcation is sometimes referred to as a *soft loss of stability*. We also note that as the speed of the rotor is reduced towards the critical speed, Ω_c , the amplitude of

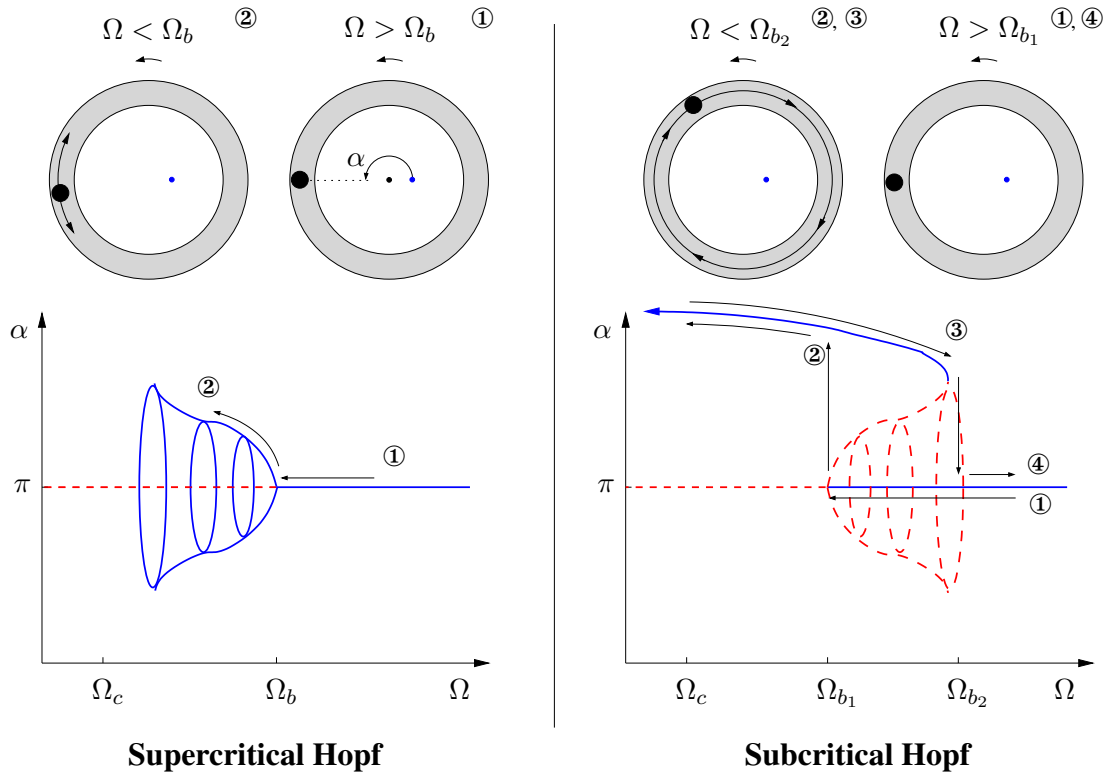


Figure A.1. Bifurcation diagrams in the vicinity of both a supercritical and a subcritical Hopf. Solid blue lines represent stable solutions and red dashed lines unstable ones. The associated ball motions at the numbered positions are illustrated in the schematic diagrams above.

the ball oscillations will grow and the periodic orbit can itself destabilise. This may lead to a desynchronized state in which the ball lags the rotor and whirls backwards along the race.

Next, the right hand diagram illustrates the corresponding situation near a subcritical Hopf. Again, for high enough rotation speeds the balanced state is stable, ①. However, as the speed decreases through Ω_{b_1} , the balanced equilibrium position destabilises and the solution suddenly jumps to the state in which the ball whirls about the race, ②. Because the transition to the desynchronized state is immediate, a subcritical bifurcation is also known as a *hard loss of stability*. Clearly this switch to a desynchronized state without any prior warning can be particularly dangerous in high speed applications. This type of behaviour occurs because at a subcritical Hopf an unstable periodic orbit is born and this solution surrounds the stable equilibrium. As the periodic orbit folds over and gains stability at Ω_{b_2} , a region of bistability is created. Thus as the rotation speed is increased back through Ω_{b_1} the ball feels no change and will remain whirling for speeds below Ω_{b_2} , ③. Finally, as the speed passes through Ω_{b_2} the solution jumps down to the balanced state and the equilibrium position is again globally stable, ④.

A.2 The effect of the initial conditions

The aforementioned difference in the ABB's run-up and run-down characteristics is sometimes called *hysteresis*. Here however, the path dependence is due to the effect of the initial conditions and is not associated with any energy dissipation. To illustrate this concept we shall consider the phase portrait of the device in the bistable region near the subcritical Hopf bifurcation, see Figure A.2.

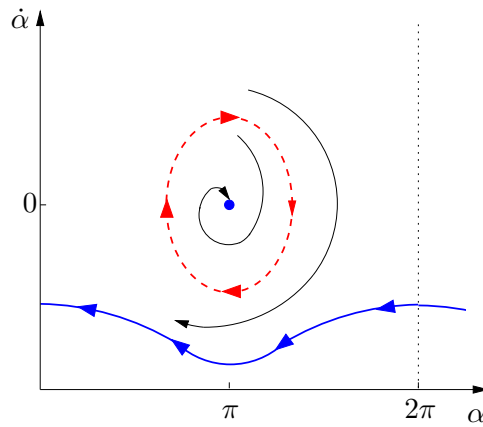


Figure A.2. Phase portrait in the bistable region $\Omega_{b_1} < \Omega < \Omega_{b_2}$ near the subcritical Hopf. The blue dot represents the stable balanced equilibrium and the blue line represents the desynchronized ball whirling state. These attracting solutions are separated by an unstable periodic orbit which is shown by the red dashed ring. Sample trajectories for solutions beginning inside and outside the unstable orbit are illustrated in black.

In the $\Omega_{b_1} < \Omega < \Omega_{b_2}$ speed range a stable balanced equilibrium coexists with a stable ball whirling state. Moreover, these two solutions are separated by the unstable periodic orbit that emanates from the subcritical bifurcation. If the initial value of the ball's position and velocity ($\alpha, \dot{\alpha}$) are such that the solution starts within the unstable orbit then the ball will be drawn towards the balanced equilibrium. However, if the solution starts outside the unstable orbit then the system will be attracted to the desynchronized state and the ball will start to whirl about the race. Thus in certain speed ranges the ball's starting position can greatly influence the final outcome of the system's behaviour. The area enclosed by the unstable orbit is called the *basin of attraction* of the stable equilibrium. For random initial conditions the size of the basin of attraction will provide an estimate for the probability of successful balanced operation. Therefore, even though the unstable orbit cannot be observed experimentally, it can still have a pronounced effect on the dynamics of the overall system.

Appendix B

Measurement of the rotor imbalance

In this appendix we shall describe the process by which the imbalance parameters for the rotor of Chapter 4 were determined. We start with a brief outline of the ‘four-run without phase’ balancing procedure, for further details of this method we refer the interested reader to [63, §9].

B.1 Four-run without phase method

The ‘four-run’ procedure begins with an initial run during which the original vibration amplitude is measured, a further three runs are then conducted at the same speed as the first but now with a single trial mass of a known weight attached to the rotor. For each of these additional runs, the trial mass is placed in the balancing plane at points that are equi-radial and spaced 120° apart. The amplitudes of the four runs can then be used to calculate the magnitude and phase of the rotor imbalance. Hence, the imbalance can be reduced through appropriate adjustments to the rotor’s mass distribution. This process can then be repeated until no further reductions in the imbalance can be achieved.

B.1.1 An example

In order to illustrate this method with an example, we shall take values from the final iteration of the balancing operation that was carried out on the rotor of Chapter 4. As each screw on the balancing disk is at the same radius of 32.5 mm, we arbitrarily choose the yellow screw as the 0° reference point and the red and black screws are then at the 120° and 240° positions respectively, see Figure 4.2.

Initial run: With the rotor running at its operating speed of 4000 rpm we measured the vibration amplitude as $10 \mu\text{m}$. (The units of vibration amplitude do not matter as long as they

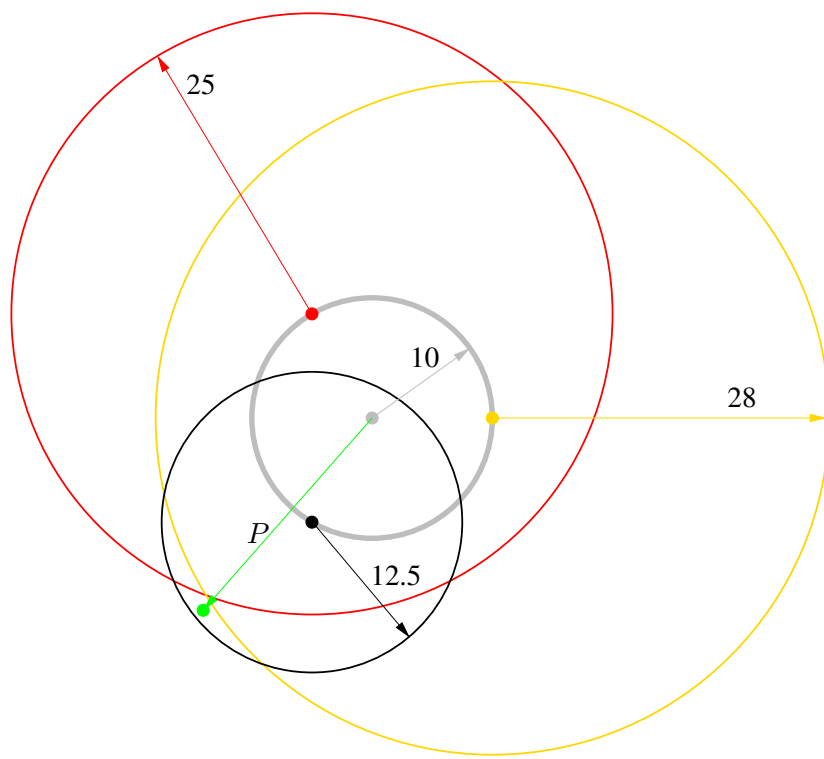


Figure B.1. Graphical construction used to determine the rotor imbalance. The radius of the grey circle corresponds to the vibration amplitude of the initial run and the positions of the three reference points at which the trial mass is to be placed are marked off on this circle. Three further circles are then drawn, each centred on the appropriate reference point and with radii equal to the vibration amplitude of the corresponding trial run. The magnitude and phase of the imbalance can then be estimated from the point P which denotes the position at which the three trial run circles (almost) intersect.

are consistent). Next we construct a grey circle with a 10 unit radius and mark off the three reference points on the circumference which are 120° apart, see Figure B.1.

First trial run: A small washer of 0.38 g mass was used as the trial weight and this was attached to the rotor at the 0° position (yellow screw). The rotor was then brought back to the same operating speed of 4000 rpm and the new vibration amplitude was measured as $28\text{ }\mu\text{m}$. On the balance diagram we then draw a yellow circle of radius 28 units which is centered on the 0° reference point.

Second trial run: The washer was attached at the 120° position (red screw) and the vibration level at 4000 rpm was measured as $25\text{ }\mu\text{m}$. A red circle is now drawn centered at the 120° position with radius 25 units.

Third trial run: For the final trial run the washer was placed at the 240° position (black screw) and the vibration amplitude at 4000 rpm was measured as $12.5\text{ }\mu\text{m}$. The corresponding

black circle is then drawn centered at the 240° position with radius 12.5 units.

If there were no experimental error then the three trial run circles would intersect at a common point, however we may estimate the appropriate point P by taking the geometric centre of the nearby intersections. The position of point P can then be measured and is given in polar co-ordinates as $(21.1, 230^\circ)$. The phase of the imbalance is *opposite*¹ to that of P and its magnitude $(mr)_I$ is given by

$$(mr)_I = \frac{R_0}{|P|} (mr)_T = \frac{10}{21.1} \times (0.38 \text{ g} \times 32.5 \text{ mm}), \\ = 5.9 \text{ g mm}, \quad (\text{B-1})$$

here R_0 is the vibration amplitude of the initial run and $(mr)_T$ is the imbalance of the trial weight, the imbalance can thus be given as 5.9 g mm at 50° . We know from previous balancing operations that the imbalance could not be reduced any further, also the conical whirl shapes that were present allow us to deduce that this remaining imbalance was mainly of the couple type.

B.2 The imbalance in $(\varepsilon, \chi, \beta)$ notation

Next we shall apply a larger known imbalance and determine the $(\varepsilon, \chi, \beta)$ parameters of the resulting imbalance in order that we may use them in the mathematical model. The inherent misalignment parameter χ_I can be estimated by envisaging two static imbalances, each equal to half the measured imbalance magnitude, placed at the bearing locations and phased opposite each other. We then have the relation

$$|\chi_I(J_t - J_p)| = \frac{1}{2}(mr)_I l_1 + \frac{1}{2}(mr)_I l_2. \quad (\text{B-2})$$

This couple has as phase of 230° (i.e. opposite the inherent imbalance) because the axial location of the balancing disk $z_{1,2}$ is negative, see Figure 4.3.

We now apply a known imbalance by *removing* washers of mass 0.38g from the yellow screw at 0° . The eccentricity ε is given by

$$M\varepsilon = n_w(mr)_w, \quad (\text{B-3})$$

here, n_w is the number of washers removed and $(mr)_w$ is the mass imbalance of each washer. The phase of the resulting eccentricity is 180° because mass has been removed from the 0° position. Also, because the balancing plane does not quite lie in the same axial plane as the centre

¹i.e. P gives the phase at which one should apply the correction mass.

of mass, the removal of the washers induces an additional couple imbalance with magnitude

$$|\chi_w(J_t - J_p)| = |n_w(mr)_w z_w|, \quad (\text{B-4})$$

and phase 0° , again this is opposite to the direction of the eccentricity because the washers' axial location z_w is negative. The directions of the imbalances are shown in Figure B.2.

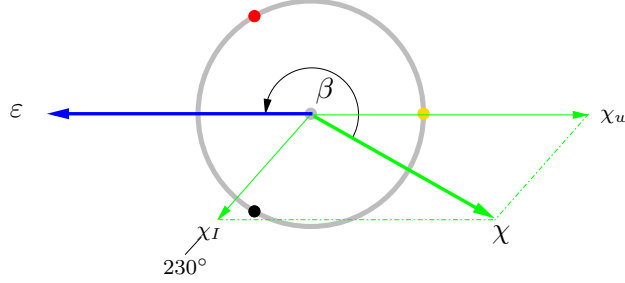


Figure B.2. Schematic diagram showing the directions of, χ_I , χ_w and χ which are the inherent, applied and resultant misalignments together with ε the (applied) eccentricity and β the phase between them. Note, it has been assumed that the single plane balancing process has eliminated the inherent eccentricity.

By resolving the couple imbalance into the x and y directions we can determine the misalignment as

$$\chi = \sqrt{\chi_x^2 + \chi_y^2}, \quad (\text{B-5})$$

where

$$\begin{aligned} \chi_x &= (1/2(mr)_I(l_1 + l_2) \cos(230^\circ) + |n_w(mr)_w z_w|) / (J_t - J_p), \\ \chi_y &= (1/2(mr)_I(l_1 + l_2) \sin(230^\circ)) / (J_t - J_p). \end{aligned} \quad (\text{B-6})$$

Finally the phase β which denotes the angle between the couple and static imbalances is given by

$$\beta = \pi - \arctan(\chi_y / \chi_x). \quad (\text{B-7})$$

The imbalance parameters and the values used to calculate them are displayed in Tables B.1 and B.2.

Table B.1. Parameter values for the calculation of the imbalance.

Rotor mass, M	1.28 kg
Transverse moment of inertia, J_t	1.38×10^{-2} kg m ²
Polar moment of inertia, J_p	1.24×10^{-3} kg m ²
Axial distance from bearing B1 to C , l_1	110 mm
Axial distance from bearing B2 to C , l_2	150 mm
Inherent rotor imbalance, $(mr)_I$	5.9 g mm
Number of washers removed, n_w	Varies between 0-4 see below
Washer imbalance, $(mr)_w$	12.35 g mm = (0.38 g · 32.5 mm)
Axial position of washers, z_w	-30 mm

Table B.2. Estimated imbalance parameters for the different number of washers removed n_w .

n_w	Imbalance [g mm]	ε [mm], (ε/R)	χ [rads]	β [degs]
0	5.9	0 (0)	6.1e-5	n/a
1	12.4	1.0e-2 (2.3e-4)	4.8e-5	282°
2	24.8	1.9e-2 (4.5e-4)	5.1e-5	247°
3	37.2	2.9e-2 (6.8e-4)	6.8e-5	224°
4	49.6	3.9e-2 (9.0e-4)	9.2e-5	211°

Appendix C

Measurement of the support parameters

In this appendix we shall describe the process by which the support parameters for the rotor of Chapter 4 were determined.

C.1 Support stiffness

Initially the stiffnesses of the supports were calculated by measuring the stiffnesses of the individual springs via an application of Hooke's law. This method is suitable for an order of magnitude calculation, however, it does not lead to accurate results because the cable ties, which are used to attach the springs to the bearing housings, also contribute to the stiffness values of the supports. As a next approach, we inferred the support parameters from modal tests that were performed at rest, for example, by looking at the Fourier transforms and decay rates of responses that were generated when the rig was tapped with a rubber mallet. However, this method also produces unsatisfactory results because the support structure of the rig has multiple modes that are interacting at different frequencies. As a consequence, we have found that for our system the frequency response of the rotor as it passes through the resonances provides the most suitable data from which the support parameters can be determined.

As discussed in Chapter 3, the stiffness matrix for the system takes the form

$$\mathbf{K} = \begin{bmatrix} \mathbf{K}_X & \mathbf{0} \\ \mathbf{0} & \mathbf{K}_Y \end{bmatrix},$$

where

$$\mathbf{K}_X = \begin{bmatrix} k_{11} & k_{12} \\ k_{12} & k_{22} \end{bmatrix} = \begin{bmatrix} k_{1_X} + k_{2_X} & k_{1_X}l_1 - k_{2_X}l_2 \\ k_{1_X}l_1 - k_{2_X}l_2 & k_{1_X}l_1^2 + k_{2_X}l_2^2 \end{bmatrix},$$

and

$$\mathbf{K}_Y = \begin{bmatrix} k_{33} & k_{34} \\ k_{34} & k_{44} \end{bmatrix} = \begin{bmatrix} k_{1Y} + k_{2Y} & k_{1Y}l_1 - k_{2Y}l_2 \\ k_{1Y}l_1 - k_{2Y}l_2 & k_{1Y}l_1^2 + k_{2Y}l_2^2 \end{bmatrix}.$$

Here, k_{1X} and k_{2X} are the stiffnesses at bearings B1 and B2 in the X direction, k_{1Y} and k_{2Y} are the corresponding bearing stiffnesses in the Y direction, and l_1 and l_2 are the axial distances from the bearings to the centre of rotation C . The stiffnesses at each bearing will differ slightly due to the variation in the angles at which the individual springs are suspended from the support posts to the bearing housings. In addition, the effective stiffness at the B1 bearing end will be increased by the presence of the rubber bands that support the motor. However, as both these effects are small (less than 10%), we shall make the assumption that the stiffnesses at both bearings are the same. We then have the relations $k_{1X} = k_{2X} = \frac{1}{2}k_{11}$ and $k_{1Y} = k_{2Y} = \frac{1}{2}k_{33}$, and so, the whole stiffness matrix \mathbf{K} can be fully determined from k_{11} and k_{33} which are the total lateral stiffnesses in the X and Y directions respectively. If the lateral degrees of freedom were elastically uncoupled from the tilting ones, that is to say if \mathbf{K} were diagonal, then we would have the expressions

$$\Omega_{\text{cyl},X} = \sqrt{\frac{k_{11}}{M}} \quad \text{and} \quad \Omega_{\text{cyl},Y} = \sqrt{\frac{k_{33}}{M}}, \quad (\text{C-1})$$

which give the critical speeds of the cylindrical modes in the undamped case. By fitting numerically generated curves to the data we have found that using values of $\Omega_{\text{cyl},X} = 1750$ rpm and $\Omega_{\text{cyl},Y} = 1500$ rpm in the above equation yield the stiffness values which best match the experimental results. Thus we have $k_{11} = 21,494 \text{ N m}^{-1}$ and $k_{33} = 15,791 \text{ N m}^{-1}$ which, to the nearest 10 N m^{-1} , gives the individual bearing stiffnesses as

$$\begin{aligned} k_{1X} = k_{2X} &\simeq 10,750 \text{ N m}^{-1}, \\ k_{1Y} = k_{2Y} &\simeq 7,900 \text{ N m}^{-1}. \end{aligned}$$

At this point we should note that for our experimental set-up, equation (C-1) holds only approximately. This is because the rotor's centre of mass is not quite at the midspan of the bearings and so there is a gyroscopic coupling between the cylindrical and conical modes. For a rotor with $J_t > J_p$, this leads to a reduction in the critical speeds of the cylindrical whirls, and so, in order to compensate for this effect we have used higher values for $\Omega_{\text{cyl},X}$ and $\Omega_{\text{cyl},Y}$ in (C-1) than that which were found experimentally. However, when we use the full model which does include the gyroscopic effect, the computed critical speeds closely match the experimental results.

C.2 Support damping

Having estimated the values for the stiffness parameters we now turn to the determination of the support damping parameter values. We shall assume the simplest case whereby the damping matrix is proportional to the stiffness matrix so that

$$\mathbf{C} = \tilde{c}\mathbf{K}. \quad (\text{C-2})$$

The constant of proportionality \tilde{c} can then be determined by fitting the results from the numerical model to the experimental data. This process is illustrated in figure C.1 where the experimental data is compared to the numerical results for three different \tilde{c} values. Here we find that the best overall fit is given by a value of $\tilde{c} = 2.5 \times 10^{-4}$ s (red curve) and it is this value for the damping that we have used in the subsequent numerical calculations of chapter 4. However, it is also clear that the higher damping value of $\tilde{c} = 5 \times 10^{-4}$ s (blue curve) matches more closely with the first peak and a lower value of $\tilde{c} = 1 \times 10^{-4}$ s (green curve) matches more closely with the fourth peak. This result suggests that (C-2) is too simple a relation and that we could improve the match by using a more sophisticated model for the damping parameters, such as that found in [1]. However, we have not performed this procedure here as it is beyond the scope of the present study, and also, an improvement in the quantitative match at the resonance peaks is thought to make little impact on the ABB dynamics, especially for the far supercritical speed regime. Nevertheless, if ABBs are to be incorporated into the complicated rotors that are encountered in real-world machinery, then more work will need to be carried out in order to enable the integration of the ABB dynamics into FEM models which include a more realistic description of the damping physics and rotor geometry. It is thought that such an approach will lead to higher accuracy quantitative predictions of the ABB performance.

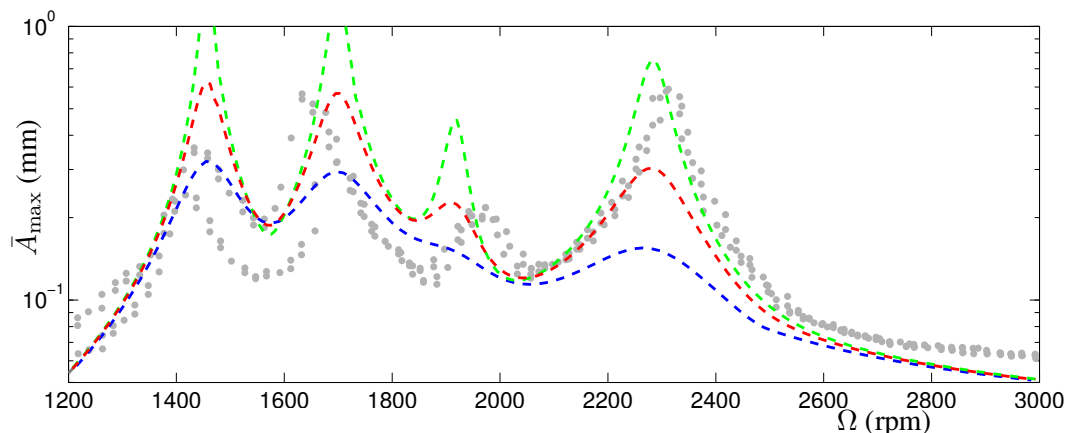


Figure C.1. Fitting of the support damping parameters. Lateral vibration levels \bar{A}_{\max} during the rigid body resonances are plotted for the experimental data (grey) together with three different values for the damping parameter \tilde{c} , namely $\tilde{c} = 1 \times 10^{-4}$ s (green), $\tilde{c} = 2.5 \times 10^{-4}$ s (red) and $\tilde{c} = 5 \times 10^{-4}$ s (blue).

Bibliography

- [1] S. Adhikari. Damping modelling using generalized proportional damping. *Journal of Sound and Vibration*, 293(1-2):156 – 170, 2006.
- [2] J. Adolfsson. *Passive Control of Mechanical Systems: Bipedal Walking and Auto-balancing*. PhD thesis, Royal Institute of Technology, Sweden, 2001.
- [3] M. Allanson, A. Pascovitch, S. Haydn-Smith, and L. Taylor. Automatic balancing: design and make. Technical report, Rolls-Royce, 2008.
- [4] S. Bae, J. M. Lee, Y. J. Kang, J. S. Kang, and J. R. Yun. Dynamic analysis of an automatic washing machine with a hydraulic balancer. *Journal of Sound and Vibration*, 257(1):3–18, 2002.
- [5] I. Blekhman. *Vibrational Mechanics*. World Scientific, 2000.
- [6] J. du Bois, N. Lieven, and S. Adhikari. Error analysis in trifilar inertia measurements. *Experimental Mechanics*, 49(4):533–540, 2008.
- [7] W. Changsen. *Analysis of Rolling Element Bearings*. Wiley, 1991.
- [8] C.-P. Chao, Y.-D. Huang, and C.-K. Sung. Non-planar dynamic modeling for the optical disk drive spindles equipped with an automatic balancer. *Mechanism and Machine Theory*, 38(11):1289–1305, 2003.
- [9] C.-P. Chao, C.-K. Sung, C.-L. Huang, and J.-S. Huang. Precision repositioning of the balancing ball in an auto-balancer system via a fuzzy speed regulator equipped with a sliding-mode observer. *Control Systems Technology, IEEE Transactions on*, 13(6):1107–1118, 2005.
- [10] C.-P. Chao, C.-K. Sung, and H.-C. Leu. Effects of rolling friction of the balancing balls on the automatic ball balancer for optical disk drives. *Journal of Tribology*, 127(4):845–856, 2005.

- [11] C.-P. Chao, C.-K. Sung, S.-T. Wu, and J.-S. Huang. Nonplanar modeling and experimental validation of a spindle-disk system equipped with an automatic balancer system in optical disk drives. *Microsystem Technologies*, 13(8-10):1227–1239, 2007.
- [12] P. Chossat and R. Lauterbach. *Methods in Equivariant Bifurcations and Dynamical Systems*. World Scientific, 2000.
- [13] J. Chung and I. Jang. Dynamic response and stability analysis of an automatic ball balancer for a flexible rotor. *Journal of Sound and Vibration*, 259(1):31–43, 2003.
- [14] J. Chung and D. S. Ro. Dynamic analysis of an automatic dynamic balancer for rotating mechanisms. *Journal of Sound and Vibration*, 228(5):1035–1056, 1999.
- [15] Delta JS AG. MADYN 2000. www.delta-js.ch, 2009.
- [16] E. Doedel, A. Champneys, T. Fairgrieve, Y. Kusnetsov, B. Sanstede, and X. Wang. *AUTO97: Continuation and bifurcation software for ordinary differential equations*, 1997.
- [17] dSPACE. <http://www.dspaceinc.com>, 2009.
- [18] SKF Autobalance Systems, Dynaspin. <http://dynaspin.skf.com>, 2000.
- [19] ebmpapst. <http://www.ebmpapst.com/en/>, 2009.
- [20] J. Ehyaei and Majid M. Moghaddam. Dynamic response and stability analysis of an unbalanced flexible rotating shaft equipped with n automatic ball-balancers. *Journal of Sound and Vibration*, 321(3-5):554–571, 2009.
- [21] A Fesca. Improvement in centrifugal machines for draining sugar. *US Patent No. 125,036*, 1872.
- [22] M.I. Friswell, J.E.T. Penny, S.D. Garvey, and A.W. Lees. *Dynamics of Rotating Machines*. In press, 2009.
- [23] G. Genta. *DYNROT: A finite element code for rotordynamic analysis*, 2000.
- [24] G. Genta. *Dynamics of Rotating Systems*. Springer, 2005.
- [25] G. Genta, C. Delprete, and E. Brusa. Some consideration on the basic assumptions in rotordynamics. *Journal of Sound and Vibration*, 227(3):611 – 645, 1999.
- [26] M. Golubitsky, I. Stewart, and D. G. Schaeffer. *Singularities and Groups In Bifurcation Theory*, Vol. 2. Springer-Verlag New York, LLC, 1988.

- [27] K. Green, A. R. Champneys, M. I. Friswell, and A. M. Muñoz. Investigation of a multi-ball, automatic dynamic balancing mechanism for eccentric rotors. *Philosophical Transactions of the Royal Society A: Mathematical, Physical and Engineering Sciences*, 366(1866):705–728, 2008.
- [28] K. Green, A. R. Champneys, and N. J. Lieven. Bifurcation analysis of an automatic dynamic balancing mechanism for eccentric rotors. *Journal of Sound and Vibration*, 291(3-5):861–881, 2006.
- [29] M. Hedaya. *A Study of Automatic Dynamic Balancers*. PhD thesis, University of Leeds, 1978.
- [30] M. Hedaya and R. Sharp. An analysis of a new type of automatic balancer. *Journal of Mechanical Engineering Science*, 19(5):221–226, 1977.
- [31] G. H M. van der Heijden. Bifurcation sequences in the interaction of resonances in a model deriving from nonlinear rotordynamics: the zipper. *Dynamics and Stability of Systems*, 15:159–183(25), 1 June 2000.
- [32] R. Horvath. *Passive Pendulum Balancer for Rotor Systems*. PhD thesis, Auburn University, 2006.
- [33] R. Horvath, G. T. Flowers, and J. Fausz. Influence of nonidealities on the performance of a self balancing rotor system. *Proceedings of IMECE*, 2005.
- [34] Rebecca Hoyle. *Pattern Formation: An Introduction to Methods*. CUP, 2006.
- [35] W.-Y. Huang, C.-P. Chao, J.-R. Kang, and C.-K. Sung. The application of ball-type balancers for radial vibration reduction of high-speed optic disk drives. *Journal of Sound and Vibration*, 250(3):415–430, 2002.
- [36] H. H. Jeffcott. The lateral vibration of loaded shafts in the neighbourhood of a whirling speed—the effect of want of balance. *Philosophical Magazine Series 6*, 37(219):304–314, 1919.
- [37] W. Kim, D.-J. Lee, and J. Chung. Three-dimensional modelling and dynamic analysis of an automatic ball balancer in an optical disk drive. *Journal of Sound and Vibration*, 285(3):547–569, 2005.
- [38] B. Krauskopf, H. Osinga, and J. Galán-Vioque, editors. *Numerical Continuation Methods for Dynamical Systems*. Springer, 2007.
- [39] M. Leblanc. Automatic balancer for rotating bodies. *US Patent No. 1,159,052*, 1915.
- [40] M. Leblanc. Automatic balancer for rotating bodies. *US Patent No. 1,209,730*, 1916.

- [41] G. W. Ledyard. Automatic balancer for centrifugal machines.
US Patent No. 1,183,745, 1916.
- [42] J. Lee and W. K. Van Moorhem. Analytical and experimental analysis of a self-compensating dynamic balancer in a rotating mechanism. *Journal of Dynamic Systems, Measurement, and Control*, 118(3):468–475, 1996.
- [43] E. W. Louden. Automatic balancing means for high speed rotors.
US Patent No. 1,314,005, 1919.
- [44] K. Nagato, T. Ide, N. Ohno, M. Nakao, and T. Hamaguchi. Automatic unbalance correction of rotors by sympathetic phase inversion of ultraviolet-curing resin. *Precision Engineering*, 33(3):243 – 247, 2009.
- [45] K.-O. Olsson. Limits for the use of auto-balancing. *International Journal of Rotating Machinery*, 10(3):221–226, 2004.
- [46] A. Pikovsky, M. Rosenblum, and J. Kurths. *Synchronization: A Universal Concept in Nonlinear Sciences*. CUP, 2001.
- [47] C. Rajalingham and S. Rakheja. Whirl suppression in hand-held power tool rotors using guided rolling balancers. *Journal of Sound and Vibration*, 217(3):453–466, 1998.
- [48] D.J. Rodrigues, A.R. Champneys, M.I. Friswell, and R.E. Wilson. Automatic balancing of a rigid rotor with misaligned shaft. *Applied Mechanics and Materials*, 5-6:231–236, 2006.
- [49] D.J. Rodrigues, A.R. Champneys, M.I. Friswell, and R.E. Wilson. Automatic two-plane balancing for rigid rotors. *International Journal of Non-Linear Mechanics*, 43(6):527–541, 2008.
- [50] D.J. Rodrigues, A.R. Champneys, M.I. Friswell, and R.E. Wilson. Device asymmetries and the effect of the rotor run-up in a two-plane automatic ball balancing system. *9th International Conference on Vibrations in Rotating Machinery*, pages 899–907, Exeter, 9-11 September 2008.
- [51] D.J. Rodrigues, A.R. Champneys, M.I. Friswell, and R.E. Wilson. A consideration of support asymmetry in an automatic ball balancing system. *Sixth EUROMECH Nonlinear Dynamics Conference, ENOC-2008*, Saint Petersburg, Russia, 30 June - 4 July 2008.
- [52] B. Ryzhik, L. Sperling, and H. Duckstein. Auto-balancing of anisotropically supported rigid rotors,. *Technische Mechanik*, 24:37–50, 2004.
- [53] B. Ryzhik, L. Sperling, and H. Duckstein. Non-synchronous motions near critical speeds in a single-plane auto-balancing device. *Technische Mechanik*, 24:25–36, 2004.

- [54] William Sellers & Co. *Railway Machinery*, page 184, Dec. 1904.
- [55] SKF Explorer bearings. <http://www.skf.com/files/059281.pdf>, 2009.
- [56] L. Sperling, F. Merten, and H. Duckstein. Self-synchronization and automatic balancing in rotor dynamics. *International Journal of Rotating Machinery*, 6:275–285, 2000.
- [57] L. Sperling, B. Ryzhik, and H. Duckstein. Single-plane auto-balancing of rigid rotors. *Technische Mechanik*, 24:1–24, 2004.
- [58] L. Sperling, B. Ryzhik, Ch. Linz, and H. Duckstein. Simulation of two-plane automatic balancing of a rigid rotor. *Math. Comput. Simul.*, 58(4-6):351–365, 2002.
- [59] S. Strogatz. *Nonlinear Dynamics and Chaos: With Applications to Physics, Biology Chemistry and Engineering*. Westview Press, 1994.
- [60] E. Thearle. A new type of dynamic-balancing machine. *Transactions of the ASME*, 54(APM-54-12):131–141, 1932.
- [61] A. J. Winzenz. Steady as you go: active balancing brings equilibrium to equipment while it's running. *Uptime magazine*, pages 30–35, Apr. 2006.
- [62] N. van de Wouw, M. N. van den Heuvel, H. Nijmeijer, and J. A. van Rooij. Performance of an automatic ball balancer with dry friction. *International Journal of Bifurcation and Chaos*, 20(1):65–85, 2005.
- [63] V. Wowk. *Machinery Vibration: Balancing*. McGraw-Hill, 1998.
- [64] T. Yamamoto and Y. Ishida. *Linear and Nonlinear Rotordynamics: A Modern Treatment with Applications*. Wiley, 2001.
- [65] Q. Yang, E.-H. Ong, J. Sun, G. Guo, and S.-P. Lim. Study on the influence of friction in an automatic ball balancing system. *Journal of Sound and Vibration*, 285(1-2):73–99, 2005.
- [66] S. Zhou and J. Shi. Active balancing and vibration control of rotating machinery: A survey. *The Shock and Vibration Digest*, 33(5):361–371, 2001.